REPORT DOCUMENTATION PAGE

AFRL-SR-AR-TR-04-

O245

1. AGENCY USE ONLY *(Leave blank)*	2. REPORT DATE	3. REPORT TYPE AND DATES COVERED
	March 2004	Final Technical Report (01 Dec 00 - 30 Nov 03)

4. TITLE AND SUBTITLE	5. FUNDING NUMBERS
FLUIDIC VIRTUAL AEROSURFACES FOR FLOW CONTROL APPLICATIONS	F49620-01-1-0015 2307/BX/BV 61102F

6. AUTHOR(S)

Ari Glezer

7. PERFORMING ORGANIZATION NAME(S) AND ADDRESS(ES)	8. PERFORMING ORGANIZATION REPORT NUMBER
Woodruff School of Mechanical Engineering Georgia Institute of Technology Atlanta, GA 30332-0405	

9. SPONSORING/MONITORING AGENCY NAME(S) AND ADDRESS(ES)	10. SPONSORING/MONITORING AGENCY REPORT NUMBER
AFOSR/NA 4015 Wilson Blvd., Room 713 Arlington, VA 22230-1954 Program Manager: Dr. Thomas Beutner	

11. SUPPLEMENTARY NOTES

12a. DISTRIBUTION AVAILABILITY STATEMENT	12b. DISTRIBUTION CODE
APPROVED FOR PULBIC RELEASE, DISTRIBUTION IS UNLIMITED	

13. ABSTRACT *(Maximum 200 words)*

This research program has focused on a novel approach to the control of the aerodynamic performance of lifting surfaces by fluidic modification of their apparent aerodynamic shape, or virtual aerosurface shaping. This flow control approach emphasizes fluidic modification of the "apparent" aerodynamic shape of the surface with the objective of altering or prescribing the streamwise pressure gradient. Control is typically effected by the interactions of arrays of synthetic jet actuators with the cross flow that displace the local streamlines near the surface and thereby induces an "apparent" modification of the flow boundary. The operating frequency of the control jets is high enough so that the actuation period is at least an order of magnitude lower than the relevant characteristic time scale of the flow. Therefore, the interaction domains between the control jets and the cross flow are quasi-steady and hence the induced aerodynamics forces are virtually time-invariant.

20040520 038

14. SUBJECT TERMS			15. NUMBER OF PAGES
			72
			16. PRICE CODE

17. SECURITY CLASSIFICATION OF REPORT	18. SECURITY CLASSIFICATION OF THIS PAGE	19. SECURITY CLASSIFICATION OF ABSTRACT	20. LIMITATION OF ABSTRACT
U	U	U	

FLUIDIC VIRTUAL AEROSURFACES FOR FLOW CONTROL APPLICATIONS

AFOSR Grant F49620-01-1-0015

Final Technical Report

Dec. 2000 –Nov. 2003

Ari Glezer
Woodruff School of Mechanical Engineering
Georgia Institute of Technology
Atlanta, GA 30332-0405

FLUIDIC VIRTUAL AEROSURFACES FOR FLOW CONTROL APPLICATIONS

Ari Glezer
Woodruff School of Mechanical Engineering
Georgia Institute of Technology
Atlanta, GA 30332-0405

I. OVERVIEW

This research program has focused on a novel approach to the control of the aerodynamic performance of lifting surfaces by *fluidic modification of their apparent aerodynamic shape, or virtual aerosurface shaping*. This flow control approach emphasizes fluidic modification of the "apparent" aerodynamic shape of the surface with the objective of altering or prescribing the streamwise pressure gradient. Control is typically effected by the interactions of arrays of synthetic jet actuators with the cross flow that displace the local streamlines near the surface and thereby induces an 'apparent' modification of the flow boundary. The operating frequency of the control jets is high enough so that the actuation period is at least an order of magnitude *lower* than the relevant characteristic time scale of the flow. Therefore, the interaction domains between the control jets and the cross flow are quasi-steady and hence the induced aerodynamic forces are virtually time-invariant. Earlier work at Georgia Tech demonstrated the utility of this approach to flow control for the suppression of flow separation at post stall angles of attack. In contrast to other approaches for control of flow separation that rely on the receptivity of the separating shear layer to time-periodic actuation and on Coanda-like unsteady reattachment (e.g., Hsiao et al. 1990), the aerodynamic forces achieved by the present approach are virtually time-invariant. More recently, the utility of this approach was demonstrated in the absence of stall at low angles of attack. For example, significant reduction in form drag with minimal lift penalty can be achieved by controlled formation of trapped vortices through the interaction of a synthetic jet and a miniature [$O(0.01c)$] passive obstruction near the leading and trailing edges of lifting surfaces.

The present report is comprised of four sections. Section I describes the interaction between a jet actuator and the cross flow over the surface of a 2-D cylinder with the objective of demonstrating the alteration of the streamwise pressure gradient. This section also compares the effects of fluidic interaction with that of a surface-mounted miniature passive obstruction. Even though the details of the interaction domains with the cross flow are not the same, a properly-scaled obstruction can induce the same global aerodynamic forces as an active fluidic element within a limited parameter range and therefore these elements can be used to complement each other. The second and third parts are concerned with the modification ofd the aerodynamic performance of lifting surfaces at small angles of attack. These effects are explored near the leading edge (Section II) and the trailing edge (Section III). While near the leading edge the effects is mainly the formation of a trapped vortex of controllable circulation, near the trailing edge, the actuation manipulates the Kutta condition by a miniature Gurney-like flap integrated with a jet actuator. Finally, Section IV focuses on an investigation of the fundamental flow mechanisms of the interaction of surface-mounted synthetic jets with a turbulent boundary layer.

1

I.2. THE INTERACTION OF SYNTHETIC JET ACTUATORS WITH A CROSS FLOW

Although the interest in control of separation for aerodynamic applications has been primarily focused on 2-D and 3-D airfoils, some control strategies have been investigated in the nominally two-dimensional flow around circular cylinders (e.g., Williams et al., 1991 and Pal & Sinha, 1997). This simple geometry is particularly attractive since it minimizes higher-order effects of a *specific* global (e.g., airfoil) geometry and has the distinct advantage that the baseline flow is extensively documented including the evolution with Reynolds number of flow separation (e.g., Roshko and Fiszdon, 1969). Amitay et al. (1997 and 1998) investigated the effect of a surface mounted synthetic jet at Re_D up to 130,000 over a range of jet angles and showed that the jets can effect an increase in lift of up to $C_L = 1$ and a corresponding reduction in pressure drag of up to 30%. The structure of the interaction domain between a jet and the nominally two-dimensional cross flow around the cylinder were investigated in detail under earlier support from AFOSR. High-resolution (0.133 mm) digital particle image velocimetry (PIV) was used to investigate the nominally two-dimensional (time- and phase-averaged) flow field in the absence and presence of actuation within a domain that includes the synthetic jet actuator and the separating shear layer on the top surface of the cylinder. These measurements were conducted in a two-dimensional (0.91 x 0.051 m cross section), closed return wind tunnel using a 63 mm cylinder model equipped with a 2-D jet actuator having an orifice width of 0.5 mm. The cylinder can be rotated about its centerline so that the angle between the jets and the direction of the free stream can be continuously varied.

The interaction domain between the jet and the cross flow at high actuation frequency is inferred from distributions of the spanwise vorticity (Figures I.1a-c) that are measured along the surface of the cylinder at $Re_D = 21,500$ (to provide a thicker boundary layer). The time-averaged vorticity map in Figure I.1a shows that the baseline flow separates at $\theta \approx 90°$. Phase-averaged vorticity concentrations in the presence of actuation (Figure I.1b) show that the (counter rotating) vortex pairs that engender the jet interact with the wall boundary layer and form a train of clockwise (CW) vortices that are advected downstream, become weaker and ultimately disappear within three to four wavelengths of the actuation ($\lambda = 0.5U_\infty/f_{act}$). These data also show that the (upstream) counterclockwise (CCW) jet vortex is accelerated above and around the CW vortex and rapidly weakens (within one

Figure I.1. Normalized vorticity $St_{Dact} = 4.0$ baseline (a), and actuated: phase-locked (b), and time-averaged (c). ($\gamma = 63°$, $C_\mu = 5.1x10^{-2}$).

wavelength). The time-averaged vorticity in the presence of actuation (Figure I.1c) shows a *finite* interaction domain that protrudes into the cross flow above the edge of the local boundary layer in the absence of actuation and ends approximately 2-3λ downstream from the jet orifice and is followed by a *thinner boundary layer compared to the baseline flow*.
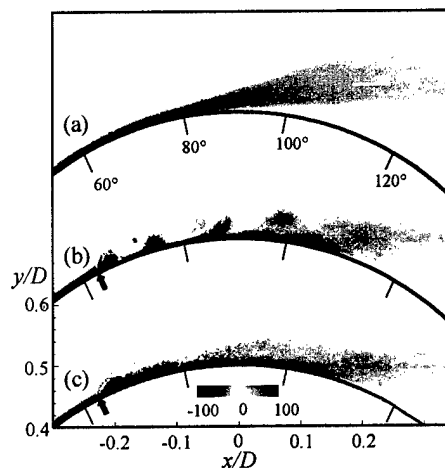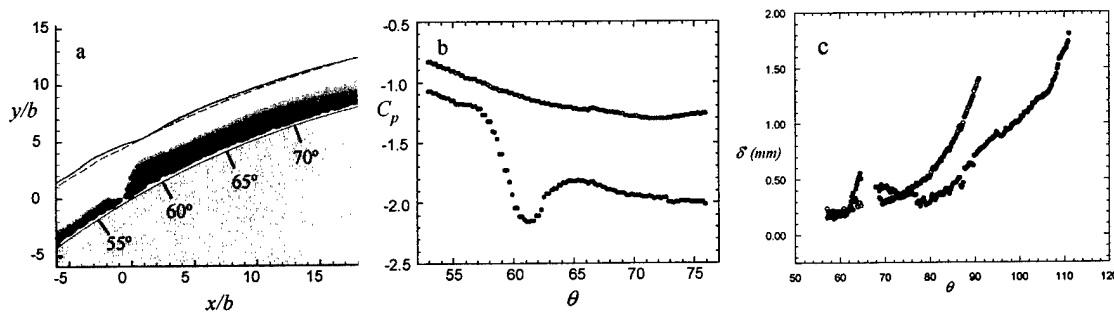
The interaction domain in Figure I.1c displaces the outer flow and thereby results in local variations in the time-averaged pressure field, which is computed from the Reynolds-averaged Navier-Stokes equations using the PIV data. Figure I.2a shows two streamlines having the same value of the stream function in the absence and presence of actuation that are superposed on the vorticity distribution of the actuated flow (note the displacement of the streamline in the presence of the actuation). Here, b is the jet's orifice width. The corresponding pressure distributions along these streamlines are shown in Figure I.2b. Compared to the baseline flow, the pressure along the streamline in the presence of actuation is lower over the entire measurement domain, indicating an increase in the velocity along the streamline due to global changes in the flow (e.g., the movement of the separation point). More significantly, within the azimuthal sector that includes the interaction domain there is a local minimum in the pressure distribution that indicates a significant favorable pressure gradient in the cross flow above the interaction domain. The favorable gradient is followed by a small region of weaker adverse pressure gradient, and finally, there is a slight favorable pressure gradient through the rest of the domain. As can be inferred from Figure I.2c, the alteration of the streamwise pressure gradient results in a thinner, more stable, boundary layer downstream of the interaction domain and a substantial delay in separation. The evolution of the (time-averaged) boundary layer displacement thickness δ^* for the baseline and actuated flows are shown in Figure I.2c. Within the interaction domain, $(60° < \theta < 80°)$, δ^* in the presence of actuation increases, reaches a local maximum immediately downstream of the jet, and then diminishes substantially suggesting the presence of a favorable streamwise pressure gradient. For $\theta > 80°$, δ^* begins to increase again although at a lower streamwise rate than in the absence of actuation, until separation occurs at $\theta = 110°$.

Figure I.2. *(a) Vorticity in interaction domain superimposed with streamlines having the same stream function value: baseline (-----) and actuated (———); The pressure coefficient along the streamlines (b) and the boundary layer displacement thickness (c): baseline (○), actuated (●).*

I.3 COMPARISON WITH A PASSIVE OBSTRUCTION

Similar to the effects of fluidic actuation, the flow can also be significantly modified by placing a small physical obstruction upstream of boundary layer separation (e.g., Prandtl et al., 1914). The obstruction (commonly referred to as a "trip") is thought to induce premature transition to turbulence within the boundary layer, and consequently delay separation presumably owing to enhanced momentum transfer with the (outer) cross flow (e.g., Fage & Warsap, 1929, Igarashi, 1986 and Hover, Tvedt & Triantafyllou, 2001). In fact, similar to the effects of a synthetic jet actuator, the asymmetric placement of a trip wire on the surface of a circular cylinder can lead to reduction in drag and even generate lift (James & Troung, 1972).

The present report describes the modifications of the aerodynamic characteristics of a circular cylinder at sub-critical Reynolds numbers using integrated synthetic jet actuators and miniature,

surface-mounted passive obstructions. Even though the details of the interaction domains of the jet and the obstruction with the cross flow are not the same, it is shown that within a narrow range of operating conditions, a properly scaled obstruction can induce the same global aerodynamic forces as an active fluidic element. It appears that the effect of these interaction domains is similar to that of circulation bubbles that have been observed upstream of separation during the (natural) drag crisis at the critical Reynolds number (e.g., Achenbach, 1968). It is remarkable that when these bubbles are formed on both sides of the cylinder (near $\theta = \pm 100°$), boundary layer separation occurs farther downstream at ($\theta_{sp} \approx 147°$) and the drag coefficient is reduced to $C_D = 0.2$ (Schewe, 1983). These changes are also accompanied by a substantially thinner wake, and the absence of vortex shedding. When these bubbles ultimately vanish at supercritical Reynolds numbers (when the boundary layer becomes fully turbulent), the drag coefficient begins to increase again and the separation point moves upstream.

The present experiments are conducted in two wind tunnels at the same Reynolds numbers (for the experiments reported here, $Re_D = 75,500$). Aerodynamic measurements are conducted in an open-return wind tunnel having a square (0.91 m) test section, while high-resolution PIV measurements (8.88 μm/pixel, and spatial resolution of 0.133 mm) along the surface of the cylinder are obtained in a close-return 2-D wind tunnel having a test section which is essentially a 5 cm wide slice of the test section in the open return tunnel. The cylinder model ($D = 63.2$ mm) can be rotated about its spanwise axis, has a pair of adjacent spanwise jet actuators (2.5 mm apart, each 0.5 mm wide) and an azimuthal array of pressure ports. For simplicity, the passive obstruction is a surface-mounted circular cylinder (diameter d).

I.3.1. Global Flow Changes

The effects induced by the interaction domain between the jet and the cross flow are compared to the displacement of the outer flow by a miniature obstruction having a circular cross section that is mounted on the surface of the cylinder at the same azimuthal positions of the jet. The variations of C_L and C_D for various obstruction azimuthal positions and diameters are shown in Figures I.3a and b, respectively. The variation of the forces with the azimuthal position of an obstruction ($d/D = 0.017$) is shown in Figure I.3a. Static pressure distributions (not shown) reveal a local pressure minimum immediately downstream of the obstruction (for $19° \leq \gamma \leq 60°$) that is associated with the acceleration of cross flow fluid over the separation bubble (cf. Figure I.2b). The drag is reduced by a significant increase in the base pressure (C_L/C_D reaches a maximum of 0.6 at $\gamma = 50°$) and then abruptly decreases when the flow separates. As shown in Figure I.3b, the characteristic height of the obstruction (at $\gamma = 60°$) has a profound effect on the aerodynamic performance due to the changes in the size of the separation bubble. There is clearly an optimal characteristic scale for the obstruction for which the lift and reduction in pressure drag are maximized. As the size of the obstruction is increased beyond $d/D > 0.02$, the separated flow does not reattach. For comparison, Figure I.3c shows the variation of C_L and $\hat{C}_D = \Delta C_D/C_{D0}$ with the momentum coefficient of a synthetic jet that is placed at $\gamma = 60°$ (the actuation frequency is $St_D = 4.0$). While both the passive obstruction and the jet result in similar
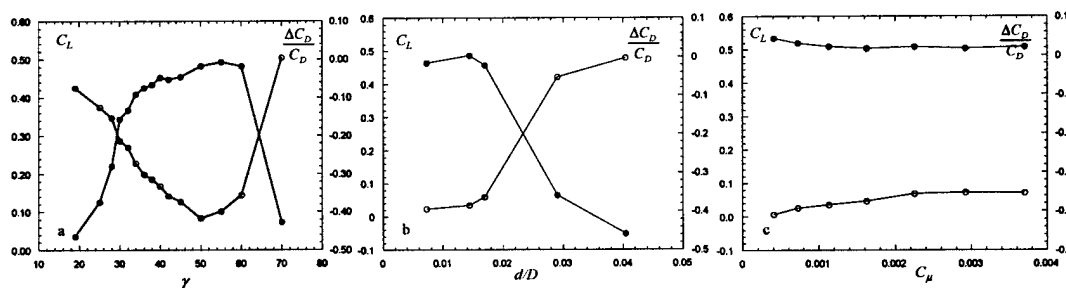

Figure I.3 *Variation of C_L and $\hat{C}_D$ with: a) azimuthal position for $d/D = 0.017$, b) obstruction diameter at $\gamma = 60°$, and c) jet momentum coefficient at $\gamma = 60°$.*

4

modifications of the surface pressure distributions, the aerodynamic forces are much less sensitive to variations in momentum coefficient compared to changes in obstruction size.

I.3.2. "Matched" Aerodynamic Performance of Jet and Passive Obstruction

The details of the interaction domains of the passive obstruction and the jet are compared when the global aerodynamic forces are approximately equal (within 2%). This "matching" is achieved using a d/D = 0.014 obstruction and a synthetic jet at St_D = 4.0, C_μ = 10^{-3} (C_L = 0.49, C_D = 0.86 for the obstruction and C_L = 0.50, C_D = 0.87 for jet actuation). Azimuthal pressure distributions for the "matched" flows (not shown) reveal that aside from details of the pressure peaks (the obstruction yields a narrower, stronger suction peak compared to the jet), the pressure distributions are otherwise very similar, including the changes in base pressure and the movement of the separation points.
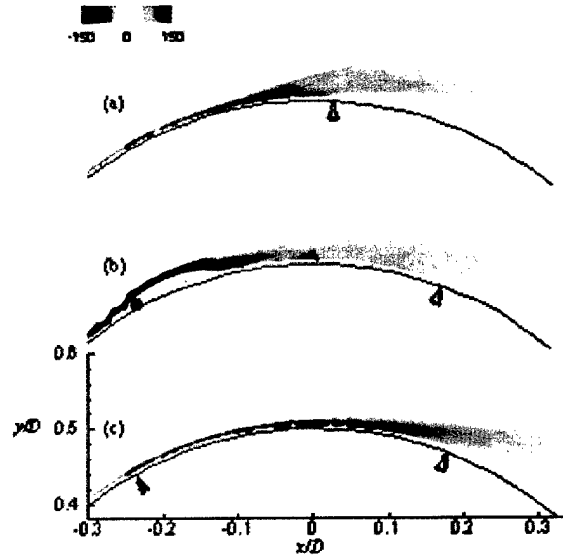

Figure I.4 Time-averaged, normalized spanwise vorticity: a) baseline, b) obstruction, and c) synthetic jet actuation. Triangles: closed-actuator location, open-separation location.
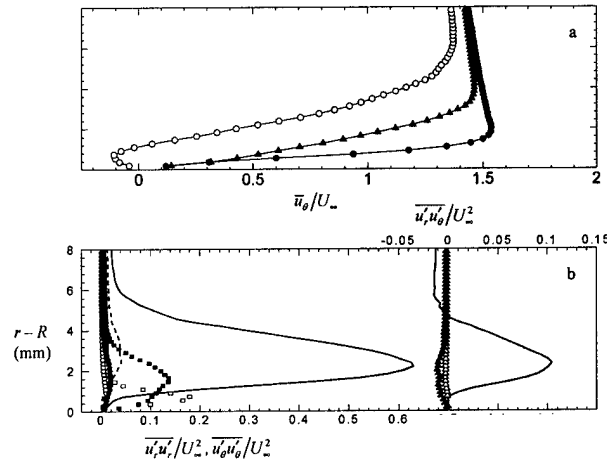
The interaction between the actuation (jet and obstruction) and the cross flow on the top surface of the cylinder is compared with the baseline flow using maps of spanwise vorticity concentrations that are obtained from PIV measurements (Figures I.4a-c). The baseline flow (Figure I.4a) separates at $\theta \approx 95°$ and the separated flow domain is marked by the presence of negative (i.e., CCW) vorticity near the surface. When the obstruction is placed on the surface (γ= 60°, Figure I.4b), the flow separates locally and reattaches at $\theta \approx 75°$ (i.e., $-0.25 \le x/D \le -0.12$) although the boundary layer downstream of the attachment region is considerably thicker than for the baseline flow at the same azimuthal domain. Separation occurs at θ_{sp} = 110° and the streamwise spreading rate of the separated shear layer appears to be smaller than for the unforced flow presumably owing to increased speed and turning of the outer flow. The vorticity maps even capture the blockage effects and thickening of the boundary layer upstream of the obstruction. Finally, the effects of jet actuation are shown in Figure I.4c. It is remarkable that even though both the jet and the obstruction yield similar aerodynamic forces and lead to flow attachment over similar azimuthal extent (θ_{sp} = 111° for the jet), the most

Figure I.5 Cross stream velocity (a) and Reynolds stresses (b). a) b-l (O), obst (▲), jet (●); b) $\overline{u'_r u'_r}/U^2_\infty$: b-l (---), obst (●), jet (O); $\overline{u'_\theta u'_\theta}/U^2_\infty$: b-l (—) , obst (■), jet (□); $\overline{u'_r u'_\theta}/U^2_\infty$: b-l (—), obst (▲), jet (△).

5

prominent difference between the vorticity maps is that the flow displacement by the obstruction is substantially larger than the displacement by the interaction domain of the jet (and therefore the suction peak induced by the obstruction is larger). Furthermore, the boundary layer downstream of the jet interaction domain is substantially thinner than the corresponding boundary layer downstream of the obstruction. Cross stream distributions of the time-averaged azimuthal velocity and Reynolds stresses downstream from the obstruction and the jet ($\theta = 100°$) are shown in Figures 3a and b, respectively. As shown in Figure I.5a, at this azimuthal position the base flow is already separated and the boundary layer downstream of the obstruction is significantly thicker and the velocity outside of the layer is somewhat lower than in the boundary layer induced by the jet. It is remarkable that the distributions of Reynolds stresses downstream of the interaction domains (Figure I.5b) are significantly *lower* than in the baseline flow even when the flows are completely attached (not shown). That this reduction is also prevalent (radially) outside of the boundary layer, indicates that the two interaction domains lead to significant reductions in velocity fluctuations that are associated with vortex shedding into the wake. In a similar manner, the appearance of a natural separation bubble on one or both sides of the cylinder at the critical Reynolds number that corresponds to the drag crisis (Achenbach, 1968, Bearman, 1969) results in substantial changes in the shedding of organized vorticity into the wake. These findings are consistent with the earlier observations of Amitay, Smith & Glezer (1998) who showed that the Reynolds stresses in the wake are reduced by actuation and that the spectral peak at the vortex shedding frequency is significantly suppressed.

I.4. THE INTERACTION OF A SYNTHETIC JET WITH A "TRIPPED" BOUNDARY LAYER

The effects of synthetic jet actuation in a cylinder boundary layer that is presumably "tripped" by a conventional trip wire is investigated to assess whether the tripped boundary layer impedes the efficacy of the jet actuation. The "tripped" boundary layer is turbulent-like flow that is formed by symmetrically placing a pair of cylindrical obstructions ($d/D = 0.02$) on the cylinder surface well at $\gamma = \pm 34°$ that yield a turbulent-like (supercritical) pressure distribution (as may be characterized by increased suction peaks and base pressure). The changes in the pressure distribution result in a substantial reduction (41%) in pressure drag ($C_D = 0.82$ compared to 1.4 for base flow). In the presence of the trip, the jet is more effective farther downstream (near $\gamma = 100°$, $St_D = 4$ and $C_\mu = 3.8 \times 10^{-3}$). The asymmetry induces additional increase and decrease in the magnitude of the suction peak on the actuated and unactuated surfaces of the cylinder owing to the change in circulation which yields $C_L = 0.36$. The increase in the base pressure contributes to a further reduction in drag ($C_D = 0.59$) relative to the "tripped" flow. Maps of normalized, time-averaged spanwise vorticity concentrations with superimposed cross stream velocity distributions of the flow fields (i.e., the baseline, and in the absence and presence of jet actuation) are shown in Figures
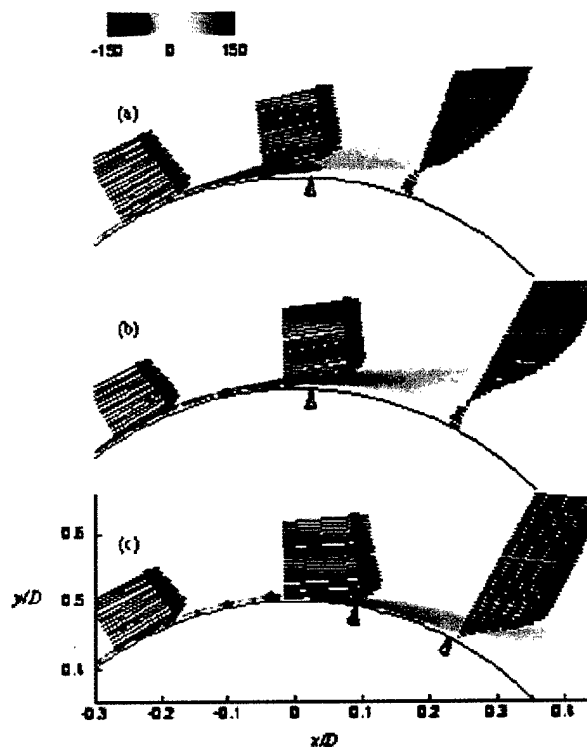

Figure I.6 Normalized spanwise vorticity, ReD = 75,000: a) baseline, b) tripped, and c) actuated. Boundary layer separation marked with open triangles, synthetic jet actuator location marked bv closed triangle.

6

I.6a-c. Although the "tripped" flow appears to be attached farther downstream than the base flow and the separating shear layer appears to be deflected towards the surface of the cylinder, it is remarkable that boundary layer separation (as determined from zero wall shear stress, not shown) still occurs at nominally $\theta_{sp} = 93°$ for both the baseline and tripped flows. Corresponding cross stream velocity distributions at $\theta = 100°$ (Figure I.7) show that the tripped flow is indeed
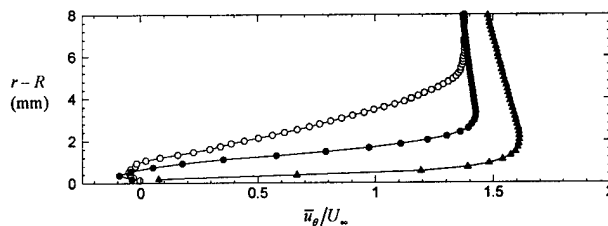

Figure I.7 *Cross stream velocity distributions, $\theta = 100°$: baseline (O), tripped (●), actuated (▲).*

deflected towards the wall and that the separated flow domain occurs within a narrow cross stream domain that is less than one millimeter above the surface. The presence of separation bubbles downstream of the obstructions at $\gamma = \pm 34°$ apparently modifies the local streamwise pressure gradient and results in a thinner boundary layer at separation. The fact that the location of boundary layer separation is virtually identical to that of the baseline flow further suggests that transition to turbulence is incidental in the alteration of the global aerodynamic characteristics of the tripped flow. Nevertheless, these seemingly minor changes in the flow are responsible for the substantial changes in the aerodynamic forces (incidentally, a similar effect is observed when the synthetic jet is positioned at $\gamma = 30°$). It seems plausible that a similar mechanism is associated with the onset of the drag crisis at the critical Reynolds number owing to the appearance of recirculating flow bubbles near $\theta = \pm 100°$ (Achenbach, 1968). Jet actuation of the "tripped" flow causes more dramatic changes in the velocity and vorticity distributions which include displacement of the time-averaged separation point to $\theta_{sp} = 116°$ and a downward deflection of the separated shear layer. These changes lead to a thinner wake that is displaced downward, as noted by Glezer, et al. (2003).

Cross stream distributions of the Reynolds stresses for the three flows are shown in Figures I.8a-i. In the baseline flow (Figure I.8a-c), the three stress components increase in magnitude with downstream distance, and do not completely vanish outside of the boundary layer even upstream of separation, ostensibly as a result of potential fluctuations that are associated with the global vortex shedding. As noted above, the addition of the upstream "trips" results in a reduction in all three components of Reynolds stress across the boundary layer. This reduction, which extends outside the layer suggests that the bulk
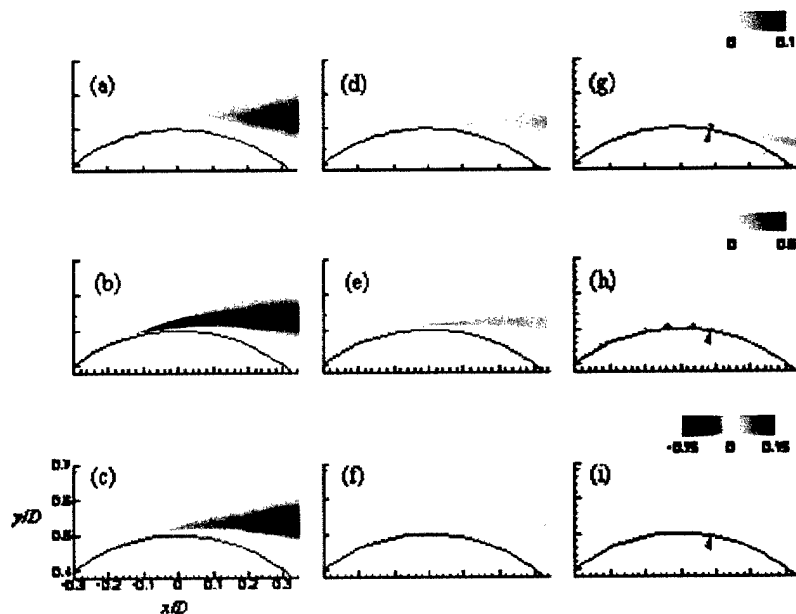

Figure I.8 *Normalized Reynolds Stresses: $\overline{u_r' u_r'}/U_\infty^2$ (a, d, g), $\overline{u_\theta' u_\theta'}/U_\infty^2$ (b, e, h), $\overline{u_r' u_\theta'}/U_\infty^2$ (c, f, i); baseline (a, b, c), tripped (d, e, f), actuated (g, h, i).*

7

motion due to global vortex shedding is diminished. In fact, as shown in Figures I.8d-e (tripped flow), the decrease in the Reynolds stress persists in the separated shear layer (presumably the result of reduction in both global potential velocity fluctuations that are associated with vortex shedding and turbulence production within the separating shear layer owing to stretching in the stain field of the large scale shed vortices. Jet actuation (Figures I.8g-i) brings about additional reduction in the Reynolds stresses relative to the "tripped" flow, both within the boundary layer and the separated shear layer both upstream and downstream of the jet actuator (at the actuator orifice, $\gamma = 100°$, the peak in $u'_\theta u'_\theta$ has approximately the same magnitude as in the tripped flow and the radial velocity fluctuations are larger due to the velocity perturbations introduced by the jet itself. However, farther downstream the turbulent fluctuations added by the jet are rapidly dissipated and the overall levels of the Reynolds stresses are lower than in the "tripped" flow suggesting that the high frequency (small-scale) actuation that are introduced by the jet, lead to enhanced dissipation in the base flow that is augmented by suppression owing to the presence of global, favorable pressure gradient.

Even though it is difficult to assess the relative importance of these (potentially competing) mechanisms in the reduction in turbulence, the present data suggests that the delay in separation and the concomitant changes in the global aerodynamic forces are not merely the result of turbulent transition within the surface boundary layer. Rather, these changes are effected by the formation of the interaction domains between the actuation and the cross flow that modify the apparent aerodynamic shape of the cylinder (and other aerodynamic surfaces).

REFERENCES

Achenbach E., "Distribution of local pressure and skin friction around a circular cylinder in cross flow up to Re=5 x 10^5," *J. Fluid Mech.*, **34**, pp. 625-639, 1968.

Amitay M., Smith B.L., and Glezer A. "Aerodynamic flow control using synthetic jet technology" AIAA Paper 98-0208, 36th Aerospace Sciences Meeting, Reno, NV, 1998.

Amitay, M. Honohan, A. M. Trautman, and Glezer, A., "Modification of the Aerodynamic Characteristics of Bluff Bodies Using Fluidic Actuators," AIAA Paper 97-2004, June 1997

Amitay, M., Horvath, M., Michaux, M. and Glezer, A. "Virtual Aerodynamic Shape Modification at Low Angles of Attack using Synthetic Jet Actuators," AIAA Paper 2975, 2001.

Bearman P.W., *J. Fl. Mech.*, **37**, pp. 577-585, 1969.

Fage A. and Warsap J.H., "The effects of turbulence and surface roughness on the drag of a circular cylinder," *Aeronautical Research Council R & M* No. 1283, 1929.

Glezer A., Amitay M., and Honohan A.M., "Aspects of Low- and High-Frequency Aerodynamic Flow Control," AIAA Paper 2003-0533, 41st Aerospace Sciences Meeting and Exhibit, Reno, NV, 2003.

Honohan, A., Amitay, M., and Glezer, A. "Aerodynamic Control using Synthetic Jets," AIAA Paper 2000-2401, June 2000

Hover F.S., Tvedt H., and Triantafyllou M.S., *J. Fl. Mech.*, **448**, pp. 175-195, 2001.

Hsiao, F. B., Liu,. C. F., and Shyu, J-Y. "Control of wall-separated flow by internal acoustic excitation," *AIAA J.* **28**, 1440-1446. 1990.

Igarashi T., Bull. JSME, **29**, n. 255, pp. 2917-2924, 1986.

James D.F. and Truong Q-S, "Wind load on cylinder with spanwise protrusion," Proceedings of the ASCE, Journal of the Engineering Mechanics Division, **98**, pp. 1573-1589, 1972.

Roshko A. and Fiszdon W., "On the persistence of transition in the near wake," *Problems of Hydrodynamics and Continuum Mechanics*. Soc. Industrial and Appl. Math., Philadelphia, pp. 606-616, 1969.

Schewe G., "On the force fluctuations acting on a circular cylinder in a cross flow from sub-critical to trans-critical Reynolds numbers," *J. Fluid Mech.*, **133**, pp. 265-285, 1983.

Smith, D. R., Amitay, M., Kibens, V., Parekh, D., and Glezer, A. "Modification of lifting body aerodynamics using synthetic jet actuators," AIAA Paper 1998-0209, January 1998.

II. VIRTUAL AERO-SHAPING AT LOW ANGLES OF ATTACK

II.1. OVERVIEW

The pressure drag of lifting surfaces at low angles of attack is reduced with minimal lift penalty by fluidic modification of the apparent aerodynamic shape of the surface. The pressure distribution on the surface is modified when the baseline flow is fully attached by the formation of a small stationary recirculating flow domain next to the surface, which displaces the local streamlines sufficiently to modify the local pressure distribution. In the present work, the recirculating flow domain is formed on the surface of a clark-y airfoil by combining the activation of a high-frequency synthetic jet actuator placed downstream from a miniature surface-mounted passive obstruction. The alteration of the pressure distribution around the airfoil results in a significant reduction in pressure drag that is comparable to the magnitude of the pressure drag of the baseline configuration with minimal loss of lift. The flow structure in the vicinity of the bubble and its scaling is investigated using particle image velocimetry (PIV).

II.2 INTRODUCTION

Much of the recent work on flow control techniques with the objective of extending the post stall flight envelope of various airfoil configurations has focused on the manipulation of flow separation at moderate and large angles of attack either at the leading edge or over flaps (e.g., Seifert et al.[1]). This has been typically accomplished by exploiting the instability of the separating shear layer and its receptivity to time-periodic actuation (e.g., pulsed blowing) on the time scale of the flow about the airfoil, which results in a Coanda-like unsteady reattachment. Active control techniques that have achieved varying degrees of separation control by manipulation of the unstable separated free shear layer have included external and internal acoustic excitation (e.g., Ahuja and Burrin[2], and Hsiao et al.[3]), vibrating ribbons or flaps (e.g., Neuburger and Wygnanski[4]), and steady and unsteady blowing or bleed (e.g., Williams et al.[5], and Chang et al.[6]). In these experiments, the time-periodic actuation was typically applied at a dimensionless (reduced) frequency, $F^+ \sim O(1)$ such that the actuation period scaled with the time of flight over the length of the reattached flow.

More recently, Smith et al.[7] and Amitay et al.[8, 9] demonstrated the suppression of separation over an unconventional airfoil at moderate Reynolds numbers (up to 10^6) that resulted in a dramatic increase in lift and a corresponding decrease in pressure drag. Actuation was effected using synthetic (zero mass flux) jet actuators, which were deliberately operated at frequencies that were typically *an order of magnitude higher* than the characteristic (shedding) frequency of the airfoil [i.e., $F^+ \sim O(10)$ rather than $F^+ \sim O(1)$]. These authors argued that the interaction of high-frequency zero net mass flux jets with the cross flow leads to local modification of the apparent aerodynamic shape of the flow surface, and, as a result, to full or partial suppression of flow separation. Moreover, the recent experiments of Erk[10] demonstrated the suppression of separation on an FX61-184 airfoil at Reynolds numbers up to 3×10^6 using synthetic jet actuation at frequencies up to $F^+ \sim O(100)$.

The interaction between a cross flow over a 2-D circular cylinder and surface-mounted synthetic jet actuators was recently investigated in detail by Honohan et al.[11]. These authors showed that when the jets are operated on a time scale that is well below the characteristic time scale of the base flow, their interaction with the cross flow leads to the formation of distinct quasi-steady flow regions near the surface and displacement of the local streamlines induces an apparent or virtual change in the shape of the surface and in the local pressure gradient. The acceleration of the cross flow around the interaction domain is accompanied by substantial alterations of the streamwise pressure gradient both locally and globally. As a result the surface boundary layer downstream of the interaction domain becomes thinner allowing the flow to overcome stronger adverse pressure gradients and therefore delaying (or altogether suppressing) flow separation.

10

The concept of modifying the apparent aerodynamic shape of aero-surfaces in order to prescribe the streamwise pressure distribution and therefore to influence its aerodynamic performance is not new and was addressed in a substantial body of work in the 40s and 50s. One example of this approach is the use of a stationary, trapped vortex to alter the apparent local surface curvature and therefore the direction of the external flow. Perkins and Hazen[12] used a suction slot near the trailing edge of an airfoil and an upstream cavity to trap a vortex near the trailing edge and reported substantial lift ($C_L = 1.2$) at zero angle of attack at relatively low (3%) suction coefficient. Mandl[13] used a split flap located on the pressure side of an airfoil combined with suction (at the flap) to trap a vortex and to enforce tangential flow near the trailing edges of the airfoil and the flap and alter the Kutta condition of the airfoil.

The present work focuses on the modification of the apparent aerodynamic shape of an airfoil at low angles of attack when the baseline flow is fully attached with the objective of reducing the pressure drag with minimal or no penalty in lift Chatlynne et al.[12] and Amitay et al.[13]). This is achieved by the formation of a stationary recirculating flow domain next to the surface that alters the flow above the airfoil by inducing a displacement of the local streamlines. While such a recirculating domain can be formed in principle by an array of jet actuators, in the present work this domain is formed by combining the activation of a high-frequency synthetic jet actuator that is placed downstream from a miniature surface-mounted passive obstruction.

II.3 EXPERIMENTAL APPARATUS AND PROCEDURE

Fluidic modification of the aerodynamic performance of lifting surfaces is investigated using a 2-D Clark-Y airfoil having a chord measuring 229 mm and thickness to chord ratio t/c of 0.24. Control is effected using an array of four collinear spanwise rectangular synthetic jet actuators that are integrated into the center section of the airfoil as shown schematically in Figure II.4. Each actuator jet has a flush-mounted 140 mm long and 0.5 mm wide (in the streamwise direction) orifice. The jets issue normal to the surface of the airfoil and are located at x/c = 0.22, 0.28, 0.36, and 0.44 (measured from the leading edge). Streamwise fences are placed near the (spanwise) edges of the actuator orifices to maintain a nominally two-dimensional flow in the controlled section of the airfoil. The actuator jets are driven by piezoelectric membranes built into a cavity underneath the skin of the airfoil. The airfoil is also instrumented with a circumferential array of 41 pressure ports (located at mid-span) that are each connected to an external high-speed pressure measurement system. The airfoil is mounted in a low-speed open-return wind tunnel having a square test section measuring 91 cm on a side and maximum air speed of 32 m/s (the free-stream turbulence level is lower than 0.25%). The upper and lower walls of the wind tunnel test section are adjusted to compensate for blockage created by the airfoil.

In the present work, the performance of the synthetic jet actuators is measured using their momentum coefficient

$$ C_\mu = \frac{\bar{I}_j}{\frac{1}{2}\rho_o U_o^2 c} $$

where $\bar{I}_j$ is the time-averaged momentum flux per unit length during the outstroke and is given by

$$ \bar{I}_j = \frac{1}{\tau}\rho_j b \int_0^\tau <u_j^2(\phi)> d\phi , $$

$\tau = T/2$ (T is the period of the diaphragm motion), ρ_j and ρ_o are the jet and free-stream fluid densities, respectively, b is the jet orifice width, c is the chord, U_o is the free-stream velocity,

and $<u_j(\phi)>$ is the phase-averaged velocity at the jet exit plane. During calibration, the orifice velocity of the jets is measured using a miniature hot-wire sensor following the procedure of Smith and Glezer[14].

The velocity and vorticity fields in the cross-stream (x-y) plane, z = 0, above the airfoil (i.e., on the suction side) are measured using particle image velocimetry (PIV). The flow is seeded with sub micron smoke particles and it is illuminated using a double-pulse ND-YAG laser. Image pairs are captured using a 1008x1016 pixel CCD camera with a magnification of 21 and 86μm/pixel for global and detailed views, respectively. In each image, the velocity vectors are computed using a standard cross-correlation technique. A given PIV map is averaged over 300 realizations (image pairs).

II.4. AERODYNAMIC MODIFICATION OF THE AIRFOIL PERFORMANCE

Although the primary objective of the present work is to demonstrate the effect of fluidic actuation on the aerodynamic performance of the airfoil at low angles of attack (i.e., in the absence of stall), it is instructive to gauge the effectiveness of the present actuators on the baseline configuration over a broad range of angles of attack. To this end, the pressure distribution about the airfoil was measured for α between -1 and 24° in the presence and absence of actuation. Figure II.1a-c show the distributions of the pressure coefficient for $\alpha = 1.5°$, 9° and 19°, respectively. The chord Reynolds number is $Re_c = 250,000$, the active actuator jet is located at x/c = 0.22 and the jet momentum coefficient is $C_\mu = 1.9 \cdot 10^{-3}$. As evident from the data, at $\alpha = 1.5°$ (Figure II.1a), the baseline flow in the absence of the control jet is fully attached over the entire surface of the airfoil. It is noteworthy that when the jet is activated, the suction peak decreases somewhat (by 2%) and moves slightly downstream and the (suction) magnitude of the pressure coefficient remains lower than in the absence of actuation through the trailing edge of the airfoil. These changes in C_p lead to a small decrease in lift (8%, as shown in Figure II.2a above) while the pressure drag coefficient remains unchanged. This translates to a reduction in the lift to (pressure) drag ratio. The present measurements show that in the absence of control, the baseline airfoil stalls at $\alpha \approx 7°$ (cf. Figure II.2b). In Figure II.1b, ($\alpha = 9°$) the baseline flow is stalled and when the jet (which is located in the *separated* flow domain) is activated, the flow becomes fully attached along most of the surface of the airfoil (except possibly the streamwise domain x/c > 0.75) and the resulting pressure distribution exhibits a large suction peak ($C_p = -2.8$) near x/c = 0.2, which is near the point of maximum thickness (x/c = 0.25). The apparent increase in circulation about the attached airfoil affects the pressure distribution around the *entire* airfoil and in particular it appears that the front stagnation point moves towards the pressure side and that the pressure increases along the bottom surface of the airfoil. The effectiveness of the actuation diminishes
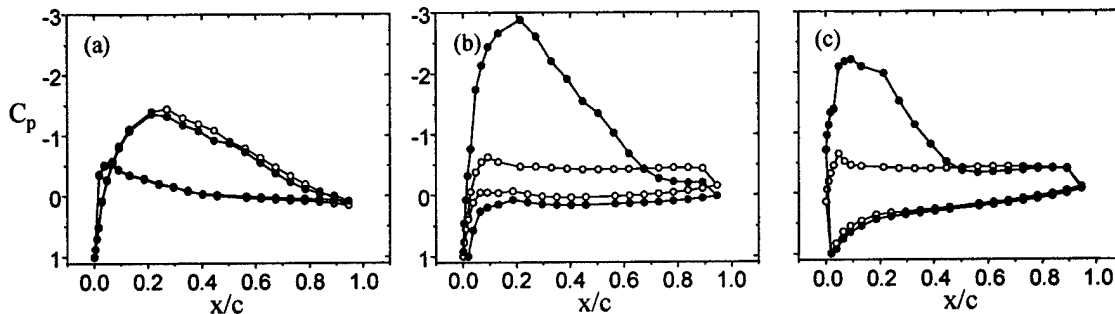
Figure II.1. *Pressure distribution around the airfoil at $\alpha = 1.5°$ (a), $9°$ (b) and $19°$ (c). $Re_c = 250,000$ and $C_\mu = 1.9x10^{-3}$. (o) baseline and (•) actuation.*

12

at high angles of attack. At $\alpha = 19°$ (Figure II.1c), the pressure peak is lower ($C_p = -2.1$) and moves farther upstream ($x/c = 0.1$) and it appears that the flow is attached only through $x/c = 0.5$ and is separated farther downstream. Note that even though the flow is partially separated, the pressure distribution along the pressure side is almost identical to the distribution in the absence of actuation.
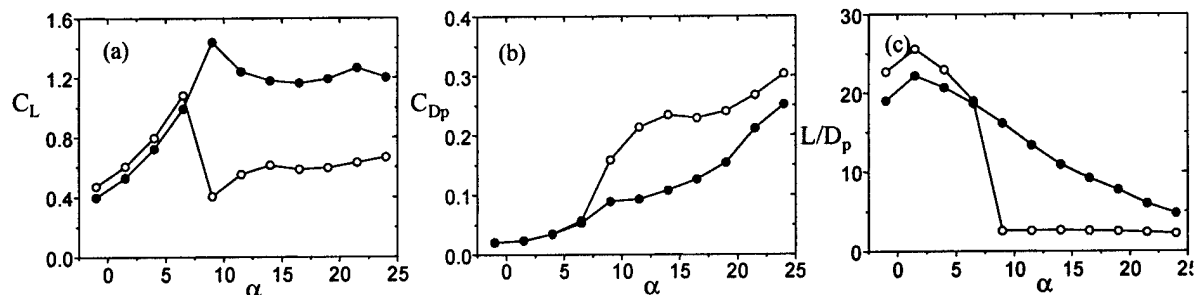

Figure II.2. *Lift coefficient (a), pressure drag coefficient (b) and lift to pressure drag ratio (c) as a function of α (o) baseline and (•) actuation.*

The pressure distributions on the airfoil in the presence and absence of actuation are integrated to yield the lift coefficient, the pressure drag coefficient and the lift-to-pressure drag ratio (Figure II.2a-c, respectively). As noted above, these data show that in the absence of actuation the airfoil stalls at $\alpha \approx 7°$ and there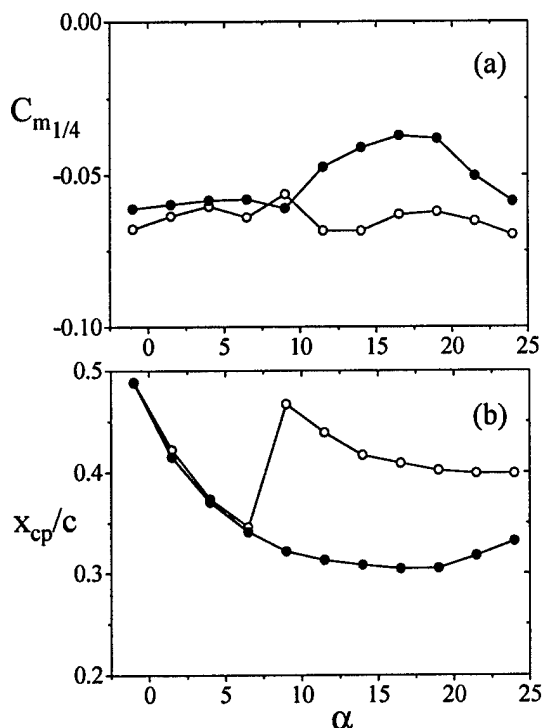after the lift remains almost invariant with angle of attack although the pressure drag continues to increase. The stall results in a sharp decrease (an order of magnitude) in the lift to (pressure) drag ratio. As noted in connection with Figure II.1a above, actuation at low angles of attack (i.e., pre-stall, $\alpha < 5°$), results in a nominal 8% reduction in lift while the drag coefficient remains the same and therefore the net reduction in the peak level of L/D_p (at $\alpha = 1.5°$) is approximately 10%. At post stall angles of attack, the actuation leads to a substantial augmentation in lift that is accompanied by a reduction in the (pressure) drag coefficient and consequently to a higher lift-to-pressure drag ratio. In the presence of actuation, the length of the separated flow domain upstream of the trailing edge increases with angle of attack and there is a relatively small decrease in the peak suction pressure (e.g., Figure II.1b and c). The net effect is that in the post-stall domain for the baseline airfoil in the absence of control, the actuation-augmented lift remains almost invariant with angle of attack and therefore the gradual increase in pressure drag results in a similar decrease in L/D_p.

Figure II.3. *Pitching moment coefficient (a) and the center of pressure (b) as a function of α (o) baseline and (•) actuation.*

The effects of the actuation on the location of the airfoil's center of pressure and the pitching moment (computed relative to c/4) are shown in Figure II.3a and b. Stall results in a

13

substantial change in the center of pressure of the baseline airfoil (nominally 35% at $\alpha = 9°$), which is accompanied by a (mild) decrease in the magnitude of the pitching moment. The actuation eliminates the abrupt change in the center of pressure and within the post stall domain shown here, x_{cp} varies by no more than 10% while the pitching moment decreases compared to the baseline configuration.

The data shown above, suggests that relatively low-level actuation [i.e., C_μ of $O(10^{-3})$] is most effective at post stall angles of attack of the baseline airfoil but that the induced aerodynamic changes at low angles of attack are, in effect, marginal. Other work at Georgia Tech (not shown) has demonstrated that control effectiveness can be realized at low angles of attack with increased actuation levels (or higher C_μ). However, as indicated by the present results, a new approach to the modification of the aerodynamic performance of airfoils at low angles of attack may be necessary if it is also desirable to maintain low actuation levels.
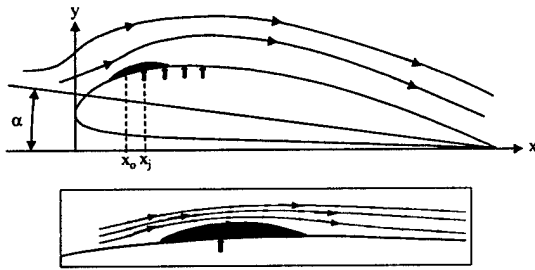

Figure II.4. Airfoil model.

In what follows, a new flow control technique is presented with the objective of reducing the pressure drag at low angles of attack with minimal or no penalty in lift. The approach is to modify the pressure distribution on the surface of the airfoil by exploiting virtual aero-shaping of the surface that is achieved by the formation of a stationary recirculating flow domain next to the surface. The formation of this domain alters the flow above the airfoil by inducing a displacement of the local streamlines that is sufficient 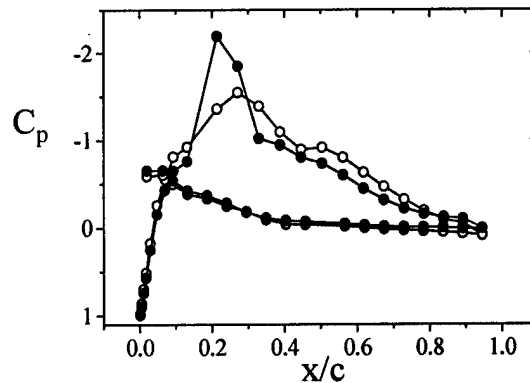to modify the pressure distribution on the surface of the airfoil even at small angles of attack. While such a recirculating domain can be formed in principle by an array of jet actuators, in the present work this domain is formed by combining the activation of a high-frequency synthetic jet actuator that is placed downstream from a miniature surface-mounted passive obstruction (as shown schematically in Figure II.4).

In a proof of concept experiment, the characteristic height of the obstruction (above the surface of the airfoil) is $h = 9.3 \cdot 10^{-3}c$ (i.e., less than 1% of the chord) and it is placed at $x_o/c = 0.19$. The synthetic jet is located at $x_j/c = 0.22$ (i.e., *downstream* of the obstruction) and is operated at $C_\mu = 1.9 \, 10^{-3}$. In these experiments, the angle of attack is $1°$ and $Re_c = 381,000$. The distribution of the pressure coefficient around the circumference of the airfoil for the baseline configuration and in the presence of actuation are shown in Figure II.5. At this angle of attack the baseline flow is attached to the surface of the airfoil. The activation of the synthetic jet actuator downstream of the obstruction results in an increase (42%) in the magnitude of the suction peak and its displacement in the

Figure II.5. Pressure distribution around the airfoil at $\alpha = 1$. $Re_c = 381,000$ and $C_\mu = 1.9x10^{-3}$. ($\circ$) baseline and ($\bullet$) actuation.

upstream direction (to $x/c = 0.21$). The pressure recovery is such that magnitude of the static pressure for $x/c > 0.33$ is smaller than for the baseline configuration (i.e., within this domain, the pressure difference between the suction and pressure sides is smaller when the control is applied) indicating that there may be a net reduction in pressure drag. Note that upstream of

14

the obstruction the pressure is slightly lower than for the baseline configuration (i.e., less negative) due to blockage caused by the obstruction.

These effects are evident from distributions of the lift, pressure drag, and the pressure drag polar (Figures 6a-c) that are computed from a series of pressure measurements over a range of
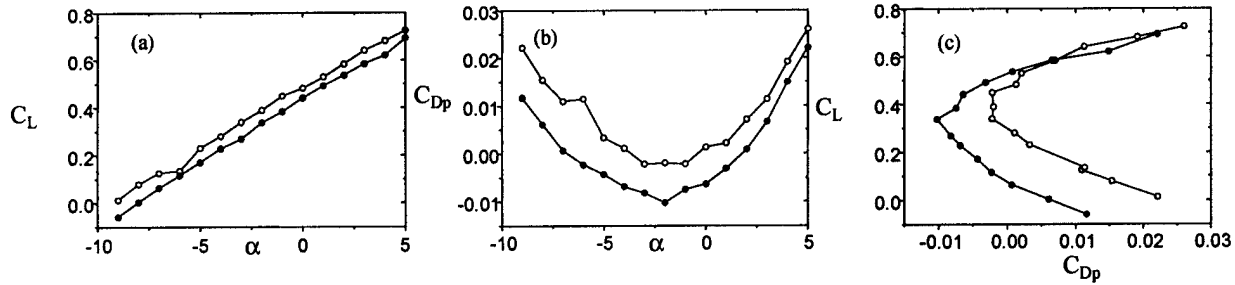

Figure II.6. *Lift coefficient (a) and pressure drag coefficient (b) as a function of α, and the pressure drag polar (c). (o) baseline and (●) actuation.*
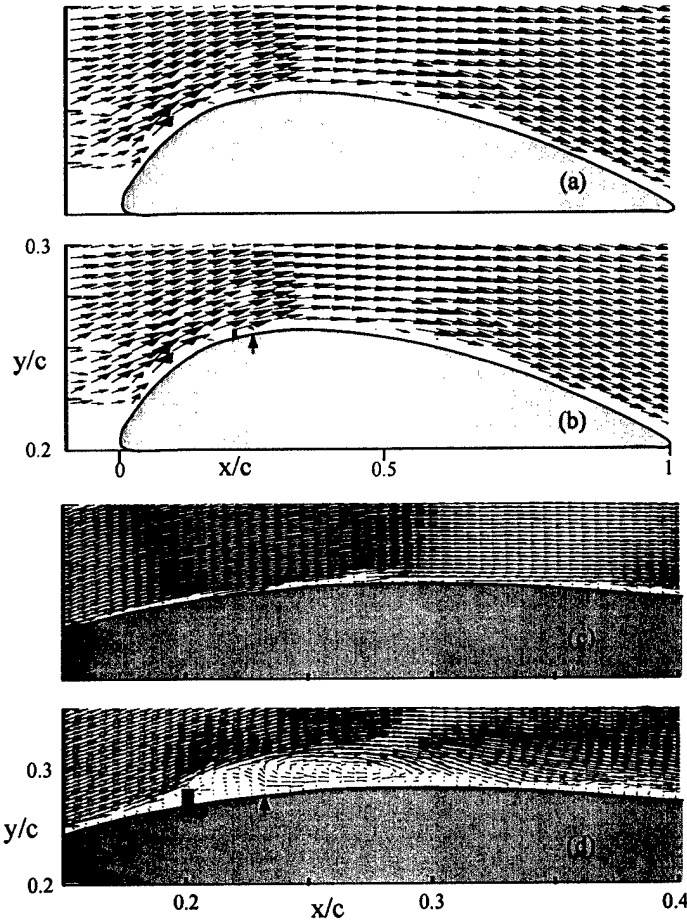
Figure II.7. *Time-averaged velocity vector maps above the airfoil. Global views: baseline (a) and actuation (b), zoom in: baseline (c) and actuation (d).*

15

angles of attack $(-9° < \alpha < 5°)$. For this range of angles of attack, activation of the control results in reductions in both of (pressure) drag and the lift coefficients (the reduction in lift is almost uniform throughout the range of measurements). However, while the reduction in the lift is about 10% with respect to the baseline configuration, the corresponding reduction in the (pressure) drag is greater than 30% resulting in an increase of the lift-to-pressure drag ratio for a given angle of attack. Moreover, the pressure drag polar (Figure 6c) shows that for $C_L < 0.25$, the pressure drag of the modified airfoil decreases significantly. The reduction in (pressure) drag without a substantial loss in lift may be important in cruise conditions and lead to significant savings in fuel over long distances.

The effect of the actuation on the flow field above the surface of the airfoil is investigated using particle image velocimetry (PIV) in the x-y plane $(z = 0)$. Each image is comprised of three partially overlapping frames measuring 10cm x 10cm and consists of 300 realization pairs. Figures II.7a-d show cross-stream maps of the time-averaged velocity vector of the baseline configuration (Figures II.7a and c) and of the controlled flow (Figures II.7b and d). Magnified views of the domain of interaction between the control actuation and the cross flow are shown in Figures II.7c and d (the magnification in Figures II.7c and d is 21μm/pixel compared to 86μm/pixel in Figures II.7a and b). In the absence of control, the time-averaged velocity field is clearly attached to the surface of the airfoil (Figures II.7a and c). When actuation is applied (Figure II.7b), the velocity vector field above the surface of the airfoil appears to be qualitatively similar to the corresponding velocity field in the absence of the control (Figure II.7a). Although the surface boundary layer is thicker near the trailing edge of the airfoil in the controlled flow, ostensibly as a result of a sub optimal pressure recovery. The high-magnification (zoomed in) images of the flow in the vicinity of the actuation jet show the formation of a closed recirculation bubble downstream of the obstruction (the location of the active jet is marked with an arrow). It is remarkable that despite its relatively small characteristic scales (cross-stream and streamwise dimensions of 0.03c and 0.1c, respectively), the presence of this bubble is sufficient to effect the aerodynamic modifications depicted in Figure II.6.The internal structure of the recirculation bubble is investigated using phase-averaged velocity vector maps. The vector maps in Figures II.8a-f are acquired at six time increments during the jet actuation cycle where Figures II.8a and d correspond to the beginning of the blowing and suction cycles. At the beginning of the blowing cycle (Figure II.8a), the recirculation domain includes a clockwise (CW) vortex centered approximately at x' = 6.1h downstream from the obstruction. The image also shows the blockage upstream of the obstruction and the separated flow downstream from its cross-stream edge. A smaller CW vortex is visible farther (12.2h) downstream. As the blowing proceeds (Figures II.8b and c), the upstream (larger) CW vortex seems to intensify as is evidenced by the relatively strong downwash that is induced near the downstream edge of the primary bubble and is advected farther downstream (the maximum streamwise length of the primary bubble is ~3.8h). These data also suggest that a weak CCW vortex is formed on the left side of the jet orifice (the nominally 2-D jet forms a counter rotating vortex pair during the blowing cycle). At the same time it appears that the strength of the secondary (downstream) vortex is somewhat reduced. The effect of the suction stroke is apparently to ingest the weak CCW vortex (immediately downstream of the obstruction) and to induce the formation of a second CW vortex within the primary bubble (Figure II.8e), which intensifies as the downstream (earlier) CW vortex becomes weaker. By the time the cycle repeats itself, the latter vortex is advected outside of the downstream edge of the primary bubble. This sequence of images clearly indicates that the streamwise extent of the bubble is of the order of one to two wavelengths of the actuation frequency (e.g., based on half the local free stream velocity). More importantly, similar to the earlier observations of Honohan et al.[11] farther downstream, the actuation frequency has negligible temporal effect on the vorticity distribution within the wall boundary layer.

The characteristic streamwise scale of the recirculation bubble (and consequently the aerodynamic performance of the airfoil) can be extended by moving the actuation jet farther

16
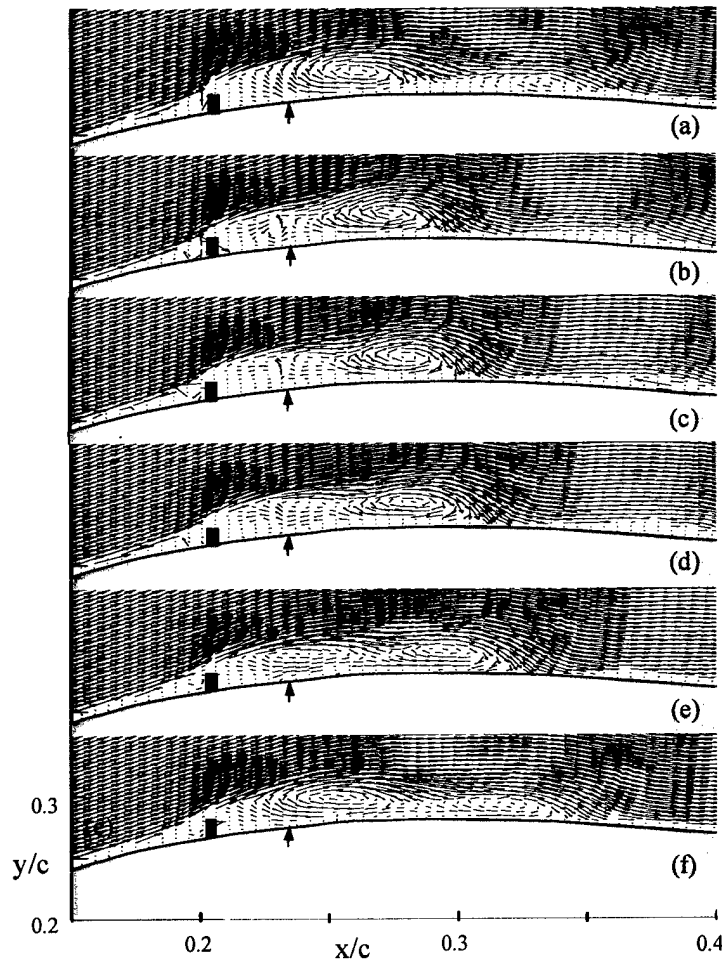
Figure II.8. *Phase-averaged velocity vector maps above the airfoil, actuation on.* $t/T = 0$ *(a),* 0.29 *(b),* 0.42 *(c),* 0.5 *(d),* 0.71 *(e) and* 0.93 *(f).*

downstream relative to the obstruction. For an obstruction having a characteristic height ($h/c = 0.01$) that is placed at $x/c = 0.22$, the jet streamwise position (relative to the obstruction) is increased from $x'/h = 0$ to 6 (x' is the streamwise distance measured from the obstruction). The resulting distributions of the pressure coefficient are shown in Figure II.9 (the distribution for the baseline configuration in the absence of actuation is also shown for reference). The most prominent feature of these distributions is the increase in the magnitude of the low (suction) pressure within the interaction domain of the actuation with the cross flow. The upstream jet ($x'/h = 0$) results in a large suction peak at $x/c = 0.25$ (-2.43 compared to -1.55 for the baseline configuration) followed by a rapid pressure recovery for $0.25 < x/c < 0.32$, and thereafter the pressure recovery towards the trailing edge is more gradual. Compared to the upstream jet, activation of the jet that is located at ($x'/h = 6$) yields a lower suction peak (around $x/c = 0.25$) and a wider pressure distribution around it. However, the pressure recovery for $x/c > 0.4$ is similar for both cases (note that the pressure in the presence of actuation is lower than for the baseline configuration indicating a reduction in pressure drag).

The corresponding distributions of lift, pressure drag, and the pressure drag polar are shown in Figures II.10a-c, respectively. When the control jet is just downstream of the obstruction

17

(x'/h = 0) the pressure drag coefficient is reduced throughout the entire measurement range while the lift is almost unchanged
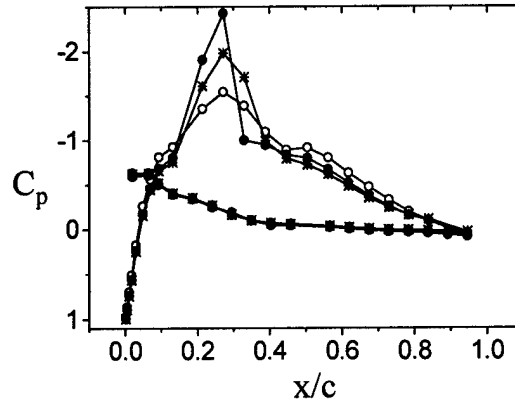
Figure II.9. Pressure distribution around the airfoil at $\alpha = 1.$). (o) baseline, (●) upstream jet is on and (✶) downstream jet is on.

compared to the baseline configuration. In fact, the pressure drag polar shows that for a given magnitude of the lift the (pressure) drag is reduced (the major effect is for $\alpha < 1^\circ$). The performance of the actuation (in terms of reduction in pressure drag with a minimum penalty in lift) is somewhat degraded when the jet is placed farther downstream (x'/h = 6) and seems to be related to the characteristic dimensions of the interaction bubble. It is noted that the downstream jet can not maintain an attached flow (in the presence of the obstruction) at angles of attack above 3°.

As noted above, based on the data in Figure II.9 it appears that placement of the actuation jet farther downstream extends the streamwise length of the recirculating bubble and hence diminishes the magnitude of the suction peak as the external flow turns around the bubble. This effect is visible in time-averaged vector maps obtained from PIV images in the streamwise domain 0.15 < x/c < 0.4 (Figures II.11a and b). These data show that the maximum height of the bubble increases from 1.07h to 1.71h and its length increases from 6.5h (0.066c) for x'/h = 0 to 12.9h (0.16h). These data confirm that the pressure distribution in the vicinity of the bubble can be adjusted (and controlled) by extending its streamwise length and the rate of turn of the outer flow.
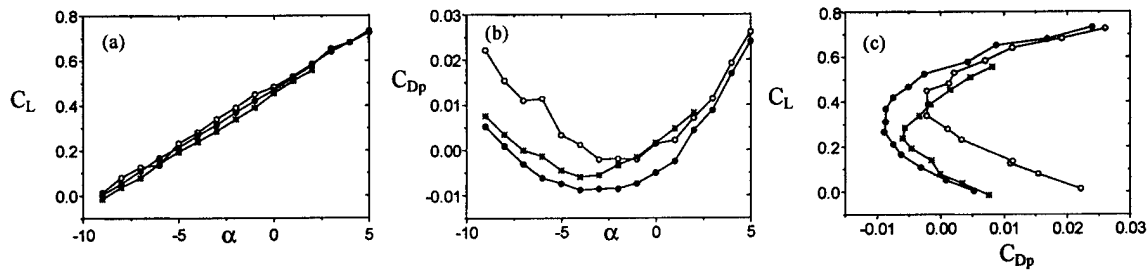
Figure II.10. Lift coefficient (a) and pressure drag coefficient (b) as a function of α, and the pressure drag polar (c). (o) baseline, (●) upstream jet is on and (✶) downstream jet is on.

In the experiments discussed above, the momentum coefficient of the jet was invariant ($C_\mu = 1.9 \times 10^{-3}$). The sensitivity of the actuation effectiveness (as measured by the aerodynamic

18

forces) to C_μ is measured over the range $1.8 \cdot 10^{-5} \le C_\mu \le 1.9 \cdot 10^{-3}$ for at $\alpha = 1°$, $x_j/c = 0.22$. The resulting pressure distributions around the airfoil (Figure II.12) are very similar and the differences in the vicinity of the actuation domain are rather small. For example, an increase in C_μ from $3.1 \cdot 10^{-5}$ to $1.9 \cdot 10^{-3}$ results in an increase of the suction peak by 10%. Therefore, it appears that for this range of momentum coefficients the size of the bubble is almost invariant. These data indicate that at least for the present actuation the effect of C_μ on the lift and (pressure) drag (not shown) and thus on the aerodynamic performance is minimal.
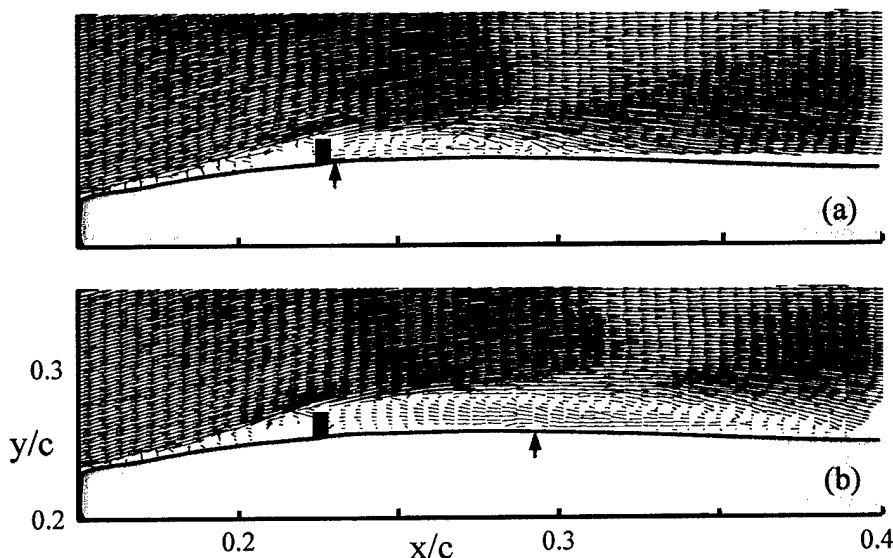

Figure II.11. Time-averaged velocity vector maps above the airfoil. Upstream jet on (a) and downstream jet on (b).

Finally, given the above results, it might be argued that similar effects may be obtained by simply replacing the recirculating flow domain that results from the actuation with a solid extension of the surface having the same shape. This notion is tested by comparing the effects of the actuation and of a passive surface modification on the pressure distribution around the
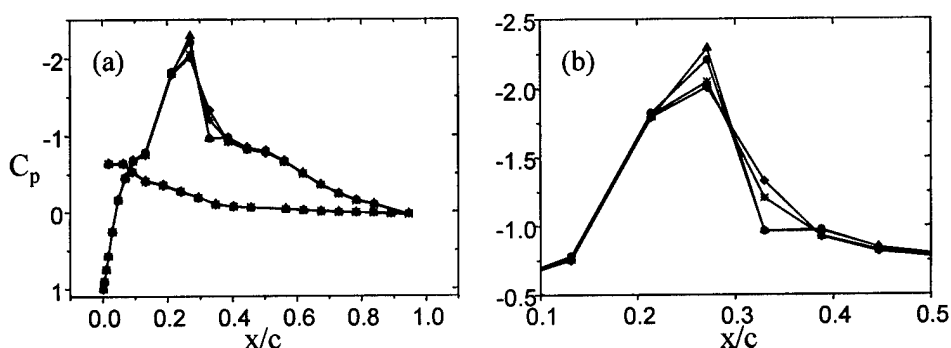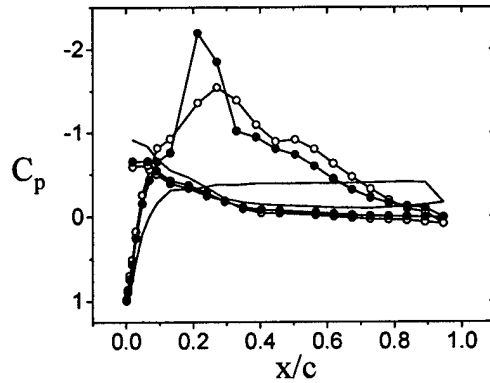

Figure II.12. Pressure distribution around the airfoil at $\alpha = 1°$. Global distribution (a) and detailed distribution (b). (●) $C_\mu = 1.9x10^{-3}$, (▲) $5.4x10^{-4}$, (✴) $3.1x10^{-5}$ and (◆) $1.8.1x10^{-5}$.

Figure II.13. *Pressure distribution around the airfoil at* $\alpha = 1^\circ$. *(* o *) baseline, (* • *) actuation and (———) solid surface extension.*

airfoil (Figure 13). The passive extension to the surface was fabricated (using stereo-lithography) based on the streamline maps that were computed from the PIV data. This extension extends approximately 0.01c above the surface and 0.12c in the streamwise direction. As shown in Figure 13, the surface extension leads to a complete flow separation ostensibly because the flow above the airfoil cannot overcome the local adverse pressure gradient that is imposed by the solid extension. Furthermore, it is clear that the solid extension does not duplicate the boundary conditions on the surface of the recirculating bubble in terms of slip and penetration.

II.5 SCALING OF THE INTERACTION DOMAIN

As shown above, the pressure drag at low angles of attack can be reduced with minimal penalty in lift by forming a stationary, recirculating flow domain next to the surface and thereby modifying its apparent aerodynamic shape and altering the surface pressure distribution even at small angles of attack. The recirculating domain is formed by combining the activation of a high-frequency synthetic jet actuator that is placed downstream from a miniature surface-mounted passive obstruction (as shown schematically in Figure II.4).

In this section, attention is restricted to the characteristic streamwise scale of the recirculation domain at a fixed angle of attack ($\alpha = 3^\circ$). This domain is altered by varying the actuation frequency and/or the jet momentum coefficient. The resulting distributions of the pressure coefficient are shown in Figures II.14a-d (the distribution for the baseline configuration in the absence of actuation is also shown for reference) for $f_{act} = 139$, 187, 362, and 850 Hz, respectively. The most striking feature of these pressure distribution is the appearance of a local minimum in the suction pressure just upstream of the obstruction (e.g., Figure II.14a at $x/c = 0.2$). This minimum vanishes as the actuation frequency is increases and is virtually undetectable at 850 Hz. The presence of this minimum suggests a blockage effect just upstream of the obstruction that can be attributed to the cross-stream height of the recirculating domain. This blockage leads to a local reduction in suction pressure compared to the baseline flow and therefore to loss of lift and potentially an increase in pressure drag.
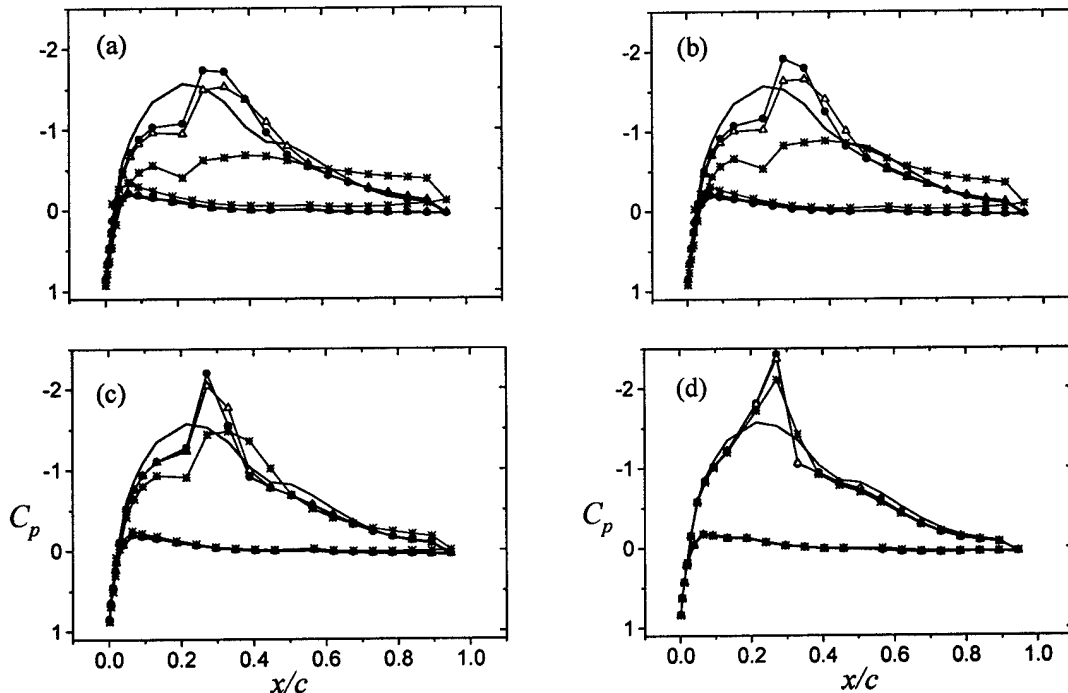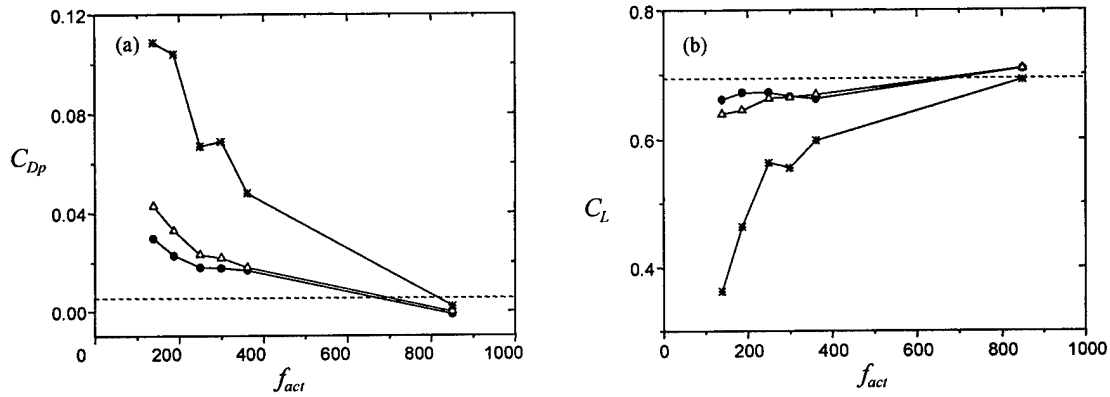

Figure II.14. Pressure distributions around the airfoil at $\alpha = 3^0$ and $Re_c = 381,000$ for (a) $f_{act} = 139Hz$, (b) 187 Hz, (c) 362 Hz and (d) 850 Hz. (—) baseline and actuated: (●) $C_\mu = 1.2x10^{-3}$, (△) $5.7x10^{-4}$, and (*) $1.7x10^{-4}$.

The effect of the blockage on the flow field can be assessed from cross-stream velocity profiles that are measured above the obstruction (using particle image velocimetry). Figure II.15 shows two such profiles measured at $x/c = 0.16$ and 0.21 (above the obstruction) for $f_{act} = 139$ HZ and 850 Hz (the jet location is marked with an arrow). The velocity vectors that correspond to the high frequency actuation not only exhibit higher speed near the surface, but their stronger turn towards the surface suggests that the smaller interaction domain results in stronger turning of the outer flow.
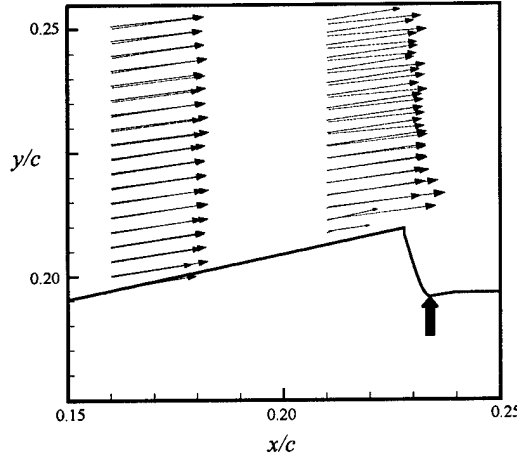
Figure II.15. *Cross-stream distributions of the velocity vector at x/c = 0.16 and 0.21. $\alpha = 3^0$ and $Re_c = 381,000$. $f_{act} = 139Hz$ (—) and 850 Hz (—).*

While the streamwise position of the suction peak appears to be unaffected by the actuation frequency, its magnitude increases with the frequency and decreases with the jet momentum coefficient. The flow appears to be most sensitive to C_μ at $f_{act} = 139$ Hz (Figure II.14a) where a decrease of an order of magnitude in the momentum coefficient (to $1.7\,10^{-4}$) results in flow separation over the upper side of the airfoil and loss of the actuation effectiveness. When the actuation frequency is increased to 187 Hz (Figure II.14b), the increase in the suction peak ($C_p = -1.95$) is accompanied by a decrease in the streamwise extent of the recirculating domain. When C_μ is decrease by an order of magnitude (to $1.7\,10^{-4}$), the flow separates near the trailing edge at $x/c \sim 0.8$. At the high actuation frequency (850 Hz, Figure II.14d), the sensitivity to the level of C_μ is greatly decreased and the suction peak reaches $C_p = -2.4$.


Figure II.16. *Pressure drag coefficient (a) and lift coefficient (b) as a function of the actuation frequency. (●) $C_\mu = 1.2x10^{-3}$, (△) $5.7x10^{-4}$, and (*) $1.7x10^{-4}$, $Re_c = 381,000$. The baseline is represented by the dashed line.*

22

The pressure distributions on the airfoil at the various actuation frequencies and momentum coefficients are integrated to yield the lift and the pressure drag coefficients (Figures II.16a and b, respectively, where the baseline levels are presented by the dashed lines). It is interesting to note that for $C_\mu = 1.2 \cdot 10^{-3}$ the pressure drag at $f_{act} = 139$ Hz actually increases by a factor of 5.4 relative to the baseline flow as a result of the streamwise length of the recirculating (interaction) domain. This increase becomes significantly larger when C_μ is decreased. However, as the actuation frequency is increased, for a given momentum coefficient the pressure drag decreases significantly and the lift increases. These data also show that for $f_{act} = 850$ Hz the actuation leads to a reduction in a pressure drag and some lift augmentation (except for $C_\mu = 1.7 \cdot 10^{-4}$, where the lift coefficient is unchanged) and the trend suggests that further increase in the actuation frequency can lead to additional improvement in performance. As noted in connection with Figure II.14 above, the dependence on C_μ decreases with increasing actuation frequency.

The effect of the actuation frequency on the size of the recirculating (interaction) domain in the vicinity of the obstruction is investigated using particle image velocimetry (PIV) in the x-y plane ($z = 0$). Each measurement field is comprised of four partially overlapping frames measuring 10cm x 10cm (only three frames are used for $f_{act} = 850$ Hz) where each frame is computed from an ensemble of 500 realization pairs. Figures II.17a-d show magnified views of the time-averaged maps of cross stream vorticity (that also include regularly-spaced cross stream velocity vectors profiles) within the domain of interaction between the control actuation and the cross flow for $f_{act} = 139$ Hz, 187 Hz, 362 Hz, and 850 Hz, respectively ($\alpha = 3^0$, $Re_c = 381,000$ and $C_\mu = 1.2 \cdot 10^{-3}$). The surface of the airfoil and the outline of the obstruction are included in each frame and the location of the jet which is placed immediately downstream of the obstruction is marked with an arrow [note that the vertical (y) scale is magnified 1.6:1 relative to the horizontal (x) scale to show more detail]. In the presence of actuation, the boundary layer upstream of the obstruction (having a characteristic height $h = 0.01c$ into the
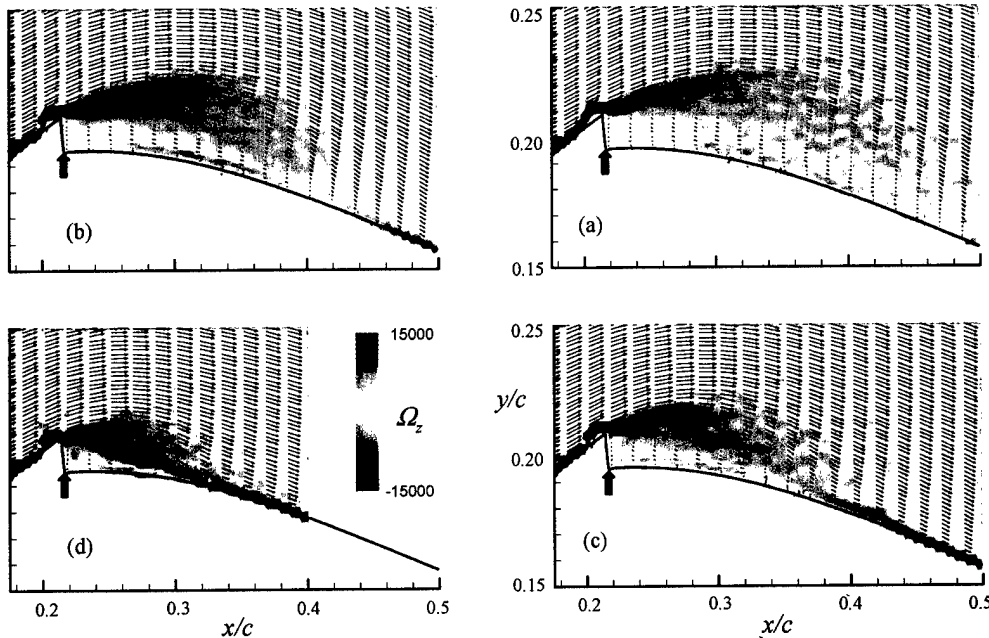
Figure II.17 *Time-averaged velocity vector and spanwise vorticity maps above the airfoil at $\alpha = 3^0$, $C_\mu = 1.2x10^{-3}$ and $Re_c = 381,000$ for (a) $f_{act} = 139$ Hz, (b) 187, (c) 362 Hz, and (d) 850 Hz.*

23

cross flow) separates locally and a closed recirculation domain is formed as a result of the jet actuation. The images show the clockwise (CW) spanwise vorticity concentration within the boundary layer and the ensuing separating shear layer, as well as the counter clockwise (CCW) vorticity near the surface within the recirculation domain downstream of the obstruction. As noted above, the streamwise and cross stream extent of this domain are influenced by the frequency and strength of the jet. Actuation at 139 Hz (Figure II.17a) results in a recirculating domain that extends almost to the downstream edge of the frame or $26 \cdot h$ downstream of the obstruction and $2.2 \cdot h$ into the cross-stream direction. Increasing the actuation frequency to 187 Hz (Figure II.17b) results in a somewhat smaller interaction domain having typical streamwise length and cross-stream height of $20 \cdot h$ and $1.7 \cdot h$, respectively. When the actuation frequency is increased to 362 Hz (Figure II.17c) and 850 Hz (Figure II.17d) it decreases the respective characteristic streamwise and cross-stream lengths of the recirculating domain to $14 \cdot h$ and $7 \cdot h$ and $1.3 \cdot h$ and $1 \cdot h$. As shown by the vector maps, the smaller interaction domain (Figure II.17c) leads to a stronger turning of the outer flow and therefore results in a stronger and sharper low-pressure (suction) peak on the surface of the airfoil.

The nominal streamwise length of the recirculating domain L_i is estimated based on the reattachment location of the recirculating domain downstream of the obstruction and is normalized by the chord of the airfoil. As shown in Figure II.18, L_i/c decay exponentially with F^+. It is noteworthy that when the jet momentum coefficient is reduced by (roughly) an order of magnitude (to $1.7 \cdot 10^{-4}$), its effectiveness at low actuation frequencies diminishes dramatically. This is demonstrated in a sequence of images in Figures II.19a-c. While for $f_{act} = 139$ Hz the flow above the airfoil is separated (not shown), at 187 Hz the recirculation domain extends through $0.8c$ (based on the pressure measurements in Figure II.14b) which is nominally $2 \cdot \lambda_{act}$ wavelengths of this actuation frequency (for which $F^+ = 1.7$). However, when
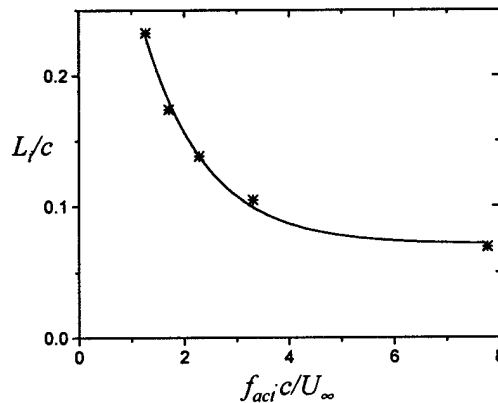
Figure II.18. Normalized streamwise length of the recirculating domain as a function of the non-dimensional frequency. $\alpha = 3^0$ and $Re_c = 381,000$.

$C_\mu = 1.2 \cdot 10^{-3}$ (Figure II.17b), the length of the circulation domain for the *same* actuation frequency is only $0.58 \cdot \lambda_{act}$ (cf. Figure II.18) indicating that the scaling of the interaction domain is not merely a function of the actuation frequency and depends also on the jet momentum coefficient. Similarly, for $f_{act} = 362$ Hz, the streamwise length of the circulation domain increases from $0.82 \cdot \lambda_{act}$ to $1.8 \cdot \lambda_{act}$ and for $f_{act} = 850$ Hz it increases from $1.1 \cdot \lambda_{act}$ to $2 \cdot \lambda_{act}$ when C_μ is decreased (i.e., compare Figures II.17c and 19b and 17d and 19c).

24

The structure of the interaction domain for f_{act} = 850 Hz is investigated using phase averaged PIV measurements (phase-locked to the actuation waveform). The images in Figures II.20a-f are acquired at six equal time increments during the actuation cycle where Figures II.20a and d correspond to the beginning of the blowing and suction strokes, respectively. At the beginning of the blowing stroke (Figure II.20a), the recirculation domain includes a CW vortex centered approximately at $x' = 10 \cdot h$ downstream from the obstruction. A smaller CW vortex is also visible farther downstream ($x' = 28 \cdot h$). As the blowing proceeds (Figures II.20b and c), the
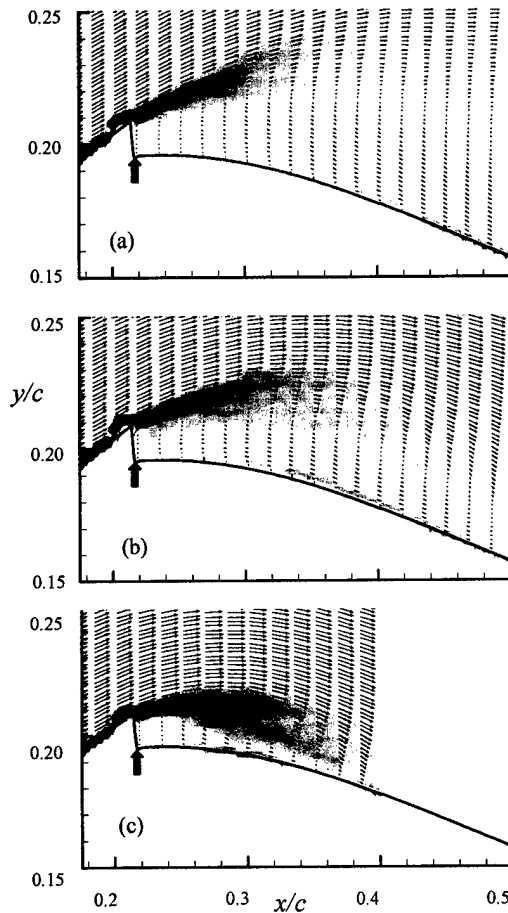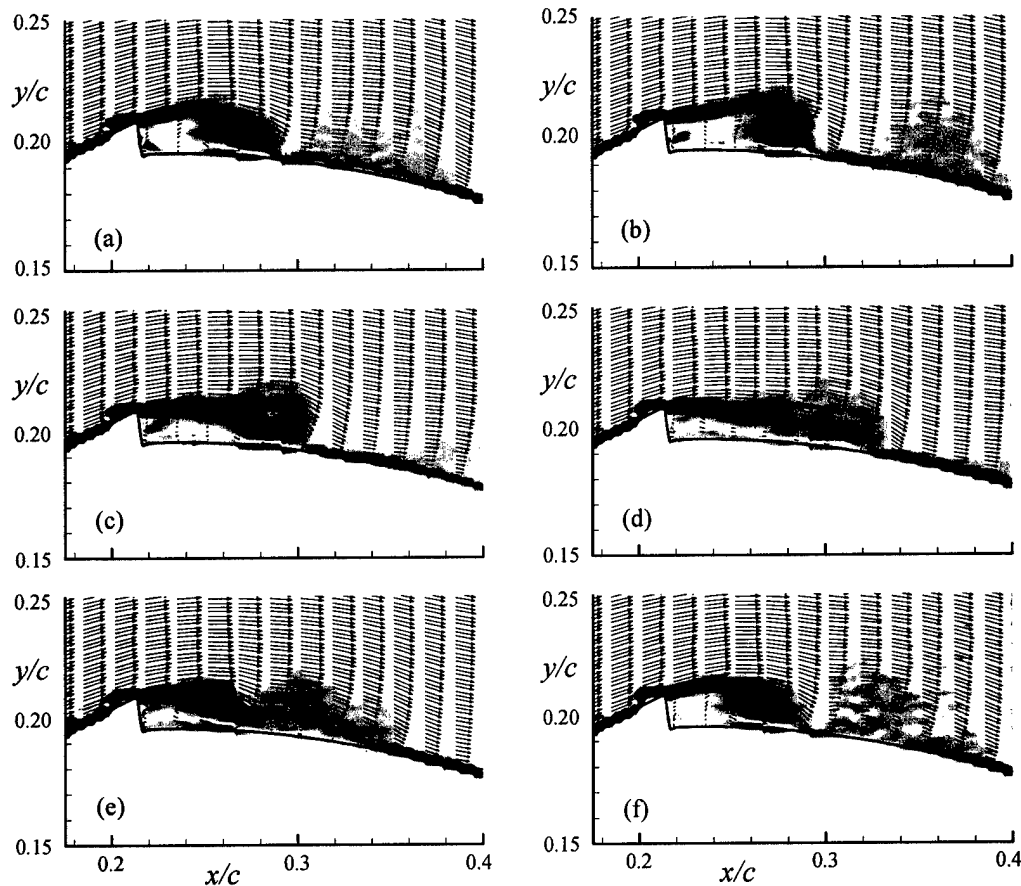

Figure II.19. Time-averaged velocity vectors and spanwise vorticity maps above the airfoil at $\alpha = 3^0$, $C_\mu = 1.7x10^{-4}$ and $Re_c = 381,000$ for (a) $f_{act} = 187$ Hz, (b) 362, and (c) 850 Hz.

upstream (larger) CW vortex seems to intensify as is evidenced by the relatively strong downwash that is induced near its downstream edge and it is advected farther downstream (the maximum streamwise length of the primary recirculating region is ~7·h). Note the formation a counter rotating vortex pair during the blowing cycle just downstream of the obstruction, Figure II.20b). At the same time, it appears that the strength of the secondary (downstream) vortex is somewhat reduced. The effect of the suction stroke is apparently to ingest the weak CCW vortex (immediately downstream of the obstruction) and to induce the formation of a second CW vortex within the primary recirculating domain (Figure II.20e), which intensifies as the downstream (earlier) CW vortex becomes weaker. By the time the cycle repeats itself, the latter vortex is advected outside of the downstream edge of the primary recirculating domain. This sequence of images clearly indicates that for this level of C_μ the streamwise length of the

25

interaction domain is of the order of one to two wavelengths of the actuation frequency. More importantly, similar to the earlier observations of Honohan et al.[12] farther downstream, the actuation frequency has negligible temporal effect on the vorticity distribution within the wall boundary layer.

In order to further explore the effect of the actuation frequency on the formation of the interaction domain, phase-averaged images similar to the data presented in Figure II.20 are shown in Figures II.21a-d for f_{act} = 139 Hz, 187 Hz, 362 Hz, and 850 Hz, respectively. These phase-averaged images are acquired at the beginning of the blowing stroke for each actuation frequency. For f_{act} = 139 Hz (Figure II.21a) the recirculation domain includes a large CW vortex centered approximately at $x' \sim 33\,h$ downstream from the obstruction (a second weaker vortex CW vortex is present downstream of the measurement domain). At f_{act} = 187 Hz (Figure II.21b), the time-averaged recirculation domain in Figure II.17b includes two CW vortices centered approximately at $x' = 10\,h$ and $24\,h$ downstream from the obstruction, where the downstream vortex appears to be considerably more diffused into the free stream (ostensibly owing to loss of phase coherence) and is closer to the downstream edge of the domain outlined by the time-averaged data in Figure II.17b. Further increase of the actuation frequency to 362 Hz and 850 HZ (Figures II.21 c and d, respectively) results in smaller vortices that are located at $x' = 10\,h$ and $20\,h$, and $x' = 5\,h$, and $12\,h$, respectively. A comparison of the

Figure II.20. Phase-averaged velocity vectors and spanwise maps above the airfoil at $\alpha = 3^0$, $C_\mu = 1.2x10^{-3}$, $f_{act} = 850$ Hz and $Re_c = 381,000$. (a) $\phi = 0^0$, (b) 60^0, (c) 120^0, (d) 180^0, (e) 240^0, and (f) 300^0.

26

images in Figure II.21 with the corresponding time-averaged images in Figure II.17 indicates that the bulk of the interaction domain scales approximately with one to two vortical structures of the actuation wavelength where the earlier (downstream) vortex becomes considerably weaker and loses its identity as it is advected downstream. It is also noteworthy that at low actuation frequencies the cross-stream extent of the interaction domain is larger than the obstruction height, which might explain the blockage (velocity reduction) that is evident from the pressure data in Figure II.14.
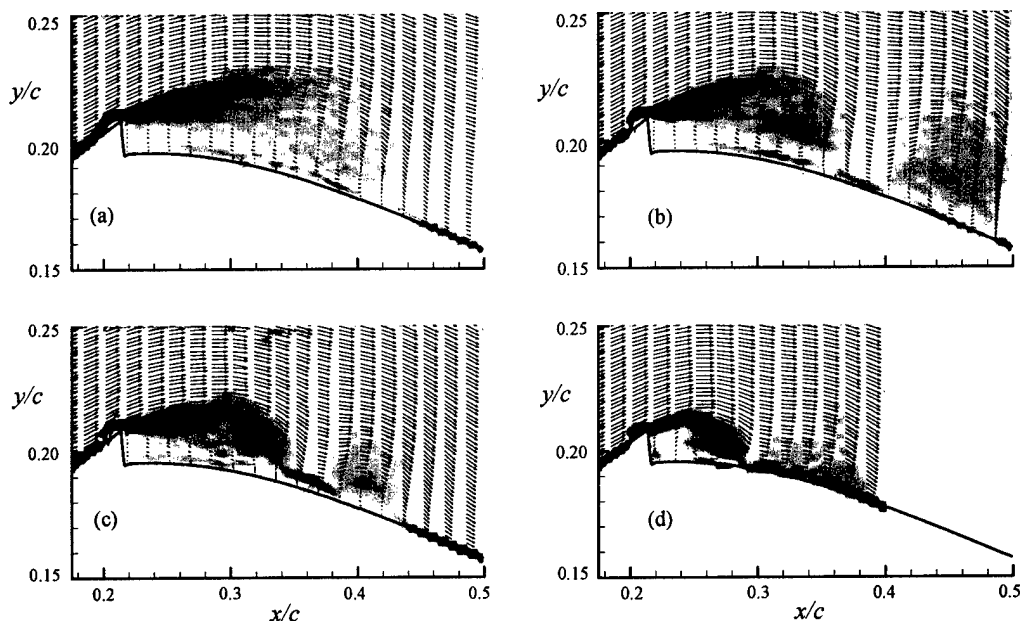
Figure II.21 *Phase-averaged velocity vectors and spanwise vorticity maps above the airfoil at $\alpha = 3^0$, $C_\mu = 1.2x10^{-3}$ and $Re_c = 381,000$ for (a) $f_{act} = 139$ Hz, (b) 187 Hz, (c) 362 Hz and (d) 850 Hz.*

II.6. CONCLUSIONS

The objective of the control approach described here is to reduce the pressure drag at low angles of attack with minimal or no penalty in lift. The pressure distribution on the surface of the airfoil is modified using virtual aero-shaping that is achieved by the formation of a stationary recirculating flow domain next to the surface as a result of the interaction between the cross flow and a high-frequency synthetic jet actuator placed downstream from a miniature surface-mounted passive obstruction. The formation of this interaction domain alters the flow above the airfoil by inducing a displacement of the local streamlines that is sufficient to modify the surface pressure distribution even at small angles of attack.

The present (and earlier) measurements show that while relatively low-level actuation [i.e., C_μ of $O(10^{-3})$] can effectively induce fully attached flow at post stall angles of attack of the baseline airfoil, the induced aerodynamic changes at low angles of attack are, in effect, marginal. As shown in earlier work, control effectiveness can be improved by increasing the actuation levels (i.e., higher C_μ) as may be achieved by arrays of jet actuators. However, the present approach is to place a low-C_μ synthetic jet actuator downstream from a miniature surface-mounted passive obstruction that typically extends 0.01c above the surface of the airfoil. Measurements of the pressure distribution about the surface of the airfoil show that compared to the baseline configuration actuation within the domain $0.19 < x/c < 0.28$ results in increased suction in the vicinity of the actuator and a reduction in the magnitude of the pressure within the recovery domain towards the trailing edge. These changes result in reductions in the

27

pressure drag that are comparable to the magnitude of the pressure drag of the baseline configuration, and concomitantly in relatively small reductions (between nil and 8%) in lift.

In the present work, the height of the obstruction (above the surface of the airfoil) is $h = 9.3 \cdot 10^{-3} c$ (i.e., less than 1% of the chord) and it is placed at $x_o/c = 0.22$ where the synthetic jet actuator is located immediately downstream of the obstruction. The experiments are conducted at $Re_c = 381,000$ for which the baseline flow is fully attached to the surface of the airfoil for $\alpha < 8^\circ$.

The interaction domain between the actuator and the cross flow is investigated using high-magnification particle image velocimetry in the x-y plane ($z = 0$). The characteristic streamwise scale of the induced recirculating flow domain is varied by changing the actuation frequency (F^+ is varied between 1.25 and 7.8) and/or the jet strength (C_μ varies between $1.7 \cdot 10^{-4}$ and $1.2 \cdot 10^{-3}$). The present work shows that the streamwise length of the interaction domain and its cross stream penetration increase with decreasing actuation frequency and jet momentum coefficient. Phase-averaged PIV images show that for $C_\mu = 1.2 \cdot 10^{-3}$, at given actuation frequency the streamwise length of the interaction domain is typically comparable to one to two wavelengths of the actuation frequency. The interaction domain contains one strong clockwise vortex and a second weaker vortex (from the earlier actuation cycle) is advected downstream and rapidly loses its identity. However, a reduction in C_μ by an order of magnitude (to $1.7 \cdot 10^{-4}$) significantly lengthens the interaction domain indicating that it does not merely scale with the actuation frequency. For example, at $F^+ = 7.8$ (850 Hz) the length of the interaction domain increases from $1.1 \cdot \lambda_{act}$ to $2 \cdot \lambda_{act}$ and at lower actuation frequency for which F^+ is 1.25 the decrease in C_μ results in a mismatch between the interaction domain and flow separation.

As a result of the changes in the curvature of the interaction domain, the induced low-pressure (suction) peak on the airfoil diminishes and widens with the actuation frequency and jet momentum coefficient leading to a substantial increase in pressure drag and a reduction in lift. It is remarkable that a significant decrease in the baseline pressure drag (compared to its magnitude) with minimal penalty in lift is only achieved at *higher* actuation frequencies ($f_{act} = 850$ Hz). The present results also show that at high actuation frequencies the aerodynamic forces (and the shape of the interaction domain) are substantially less sensitive to changes in the jet momentum coefficient.

REFERENCES

[1] Seifert, A., Bachar, T., Koss, D., Shepshelovich, M. and I. Wygnanski, I. (1993). Oscillatory blowing: A tool to delay boundary-layer separation. *AIAA J. 31*(11), 2052-2060.

[2] Hsiao, F-B, Liu, C-F, and Shyu, J-Y (1990). Control of wall-separated flow by internal acoustic excitation. *AIAA J. 28*(8), 1440-1446.

[3] Williams, D., Acharya, M., Bernhardt, J., and Yang, P. The Mechanism of Flow Control on a Cylinder with the Unsteady Bleed Technique. AIAA Paper 91-0039, January 1991.

[4] Chang, R.-C., Hsiao, F.-B., and Shyu, R.-N. Forcing Level Effects of Internal Acoustic Excitation on the Improvement of Airfoil Performance. *Journal of Aircraft 29*(5), 1992, pp. 823-829.

[5] Smith, D. R., Amitay, M., Kibens, V., Parekh, D. E. and Glezer, A., "Modification of Lifting Body Aerodynamics using Synthetic Jet Actuators", AIAA Paper 98-0209, January 1998.

[6] Amitay, M., Kibens, V., Parekh, D. E. and Glezer, A., "Flow Reattachment Dynamics over a Thick Airfoil Controlled by Synthetic Jet Actuators", AIAA Paper 99-1001, January 1999.

[7] Amitay, M., Smith, D. R, Kibens, V., Parekh, D. E. and Glezer, A. Modification of the Aerodynamics Characteristics of an Unconventional Airfoil Using Synthetic Jet Actuators. Accepted for publication in the AIAA Journal, Vol. 39, No. 6, June 2001.

28

[8]Honohan, A.M, Amitay, M. and Glezer, A., "Aerodynamic Control using Synthetic Jets", AIAA Paper 2000-2401, June 2000.

[9]Erk, P. P. Separation Control on a Post-Stall Airfoil Using Acoustically Generated Perturbations. Ph.D. Dissertation, Technische Universitat Berlin, Germany, 1997.

[10]Perkins, C.D. and Hazen, D. Some recent advances in Boundary Layer and Circulation Control. Forth Anglo-American Aeronautical Conference, 1953.

[11]Mandl, P. Effect of Standing Vortex on Flow about suction aerofoils with Split Flaps. *Nat. Res. Council of Canada, Aero. Rep. No.* 234, 1959.

[12]Chatlynne, E., Rumigny, N., Amitay, M., and Glezer, A., "Virtual Aero-Shaping of a Clark-Y Airfoil using Synthetic Jet Actuators", AIAA Paper 2001-0732, 2001.

[13]Amitay, M., Horvath, M., Michaux, M., and Glezer, A. "Virtual Aerodynamic Shape Modification at Low Angles of Attack using Synthetic Jet Actuators", AIAA Paper 01-2975, 2001.

III. AERODYNAMIC MODIFICATION AT LOW ANGLES OF ATTACK USING TRAILING EDGE TRAPPED VORTICES

III.1. OVERVIEW

The aerodynamic performance of a conventional non-symmetric airfoil is manipulated at low angles of attack (when the baseline flow is fully attached) by leveraging the presence of a small flap integrated with a synthetic jet actuator. The flap is similar in some respects to a conventional Gurney flap having a characteristic scale of $0.016c$ and is mounted on the pressure side of the airfoil just upstream of its trailing edge. The objective is to leverage the presence of the trapped vortices that are induced by the flap near the trailing edge to further manipulate the Kutta condition of the airfoil and thereby achieve global flow modifications and potentially improve it's overall aerodynamic performance. When the control jet is activated, the aerodynamic performance of the airfoil can be continuously varied from a configuration that is essentially an airfoil with a conventional Gurney flap through an airfoil that has similar performance as that of the smooth (baseline) airfoil to an airfoil that has a higher lift to pressure drag ratio.

III.2 INTRODUCTION

Utilization of flow control techniques in aerodynamic applications has traditionally concentrated on separated flows over stalled wing sections or flaps with the objective of improving the aerodynamic performance by inducing some degree of flow attachment. Control approaches have relied either on exploiting the instability of the separating shear layer at relatively low $[F^+ \sim O(1)]$ actuation frequencies (e.g., Hsiao et al.[1], Seifert et al.[2], Chang et al.[3]), or the suppression of separation by an "apparent" modification of the flow boundary at high $[F^+ \sim O(10)]$ actuation frequencies (e.g., Smith et al.[4] Amitay et al.[5,6] and Erk[7]).

The recent works of Chatlynne et al.[8] and Amitay et al.[9] has demonstrated that the modification of aerosurface by means of high-frequency fluidic actuation can be utilized for aerodynamic flow control even in the absence of stall. This is particularly important for cruise conditions at low angles of attack where the baseline flow is mostly attached. These authors achieved drag reduction with minimal lift penalty on a Clark-Y airfoil at low angles of attack. The flow above the airfoil (i.e., on the suction side) was altered by the formation of a stationary recirculating flow domain near the surface using a high-frequency synthetic jet actuation downstream from a miniature (nominally $0.01c$) surface-mounted passive obstruction. The formation of a trapped vortex within the interaction domain between the synthetic jet and the obstruction results in reduction in the pressure drag that is comparable to the magnitude of the pressure drag of the baseline configuration and is accompanied by a relatively small reduction (between nil and 8%) in lift.

This work is a continuation of the earlier work on aerodynamic flow control at low angles of attack (§II). While the work of Chatlynne et al.[8] and Amitay et al.[9] focused on flow modification on the pressure side of the airfoil near the leading edge, the current work exploits the presence of a miniature Jet Integrated Flap (*JIF*) similar to a Gurney flap that is placed on the pressure side of the airfoil just upstream of the trailing edge.

30

III.3 THE TRAILING EDGE CONTROL CONCEPT

The Gurney flap is a flat plate that is typically mounted along the trailing edge of a conventional airfoil and normal to its lower (pressure) surface such that its height is nominally 1 to 2 percent of the chord. As noted by Liebeck[10] (and confirmed by wind tunnel testing of a flap of height 0.0125c on the symmetric Newman airfoil), when the flap height is less than 0.02c, it can lead to simultaneous increase in lift and reduction in drag. Although Liebeck[10] noted that the mechanism for drag reduction was (and apparently still is) not well understood, he nevertheless suggested a possible mechanism as outlined schematically in Figures III.1a and b. Liebeck[10] conjectured that the drag reduction results from the displacement of small adjacent separation bubbles (essentially a counter-rotating vortex pair) that form along the upper and lower surfaces of the airfoil just upstream of its trailing edge (Figure III.1a). These bubbles extend into the near wake and a stagnation point is formed along the dividing streamline that extends to the trailing edge. The downwash associated with the increased lift in the presence of the Gurney flap apparently results in displacement and stretching of the separation bubbles (Figure III.1b) and therefore in a smaller velocity deficit within the airfoil's wake. The formation of the counter rotating vortex pair downstream of a Gurney flap was later demonstrated computationally on a cambered NACA 4412 airfoil profile by Jang[11] and confirmed by LDV measurements of Jeffrey et al.[12], who also show how a Gurney flap increases circulation over the airfoil by functioning as the equivalent of a stationary vortex located at the trailing edge, and give further insight into the vortex shedding mechanism. Giguère et al[13] conjectured that drag reduction can be attained if the height of the Gurney flap is smaller than the local boundary layer thickness. There is also some evidence in the literature (e.g., Myose et al.[14]) that suggests that drag reduction by Gurney flaps is more readily achieved on symmetric airfoils.
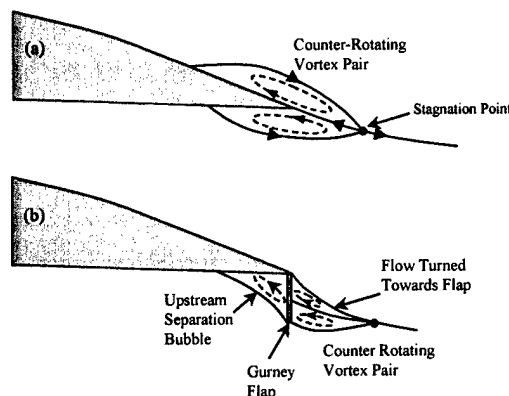
Figure III.1. Hypothesized trailing-edge flow conditions of an airfoil with a Gurney flap. (From Liebeck[10]).

The objective of the present work is to manipulate the aerodynamic performance of a conventional airfoil by leveraging the presence of a Gurney flap near its trailing edge. Specifically, the idea is to manipulate the trapped vortices that are induced by the flap to alter the Kutta condition and achieve global flow modifications. As noted in Section III.2, the concept of using trapped vortices to alter the aerodynamic performance of aero-surfaces is not new and was already addressed in the 1940s and 50s. One example of this approach is the use of a stationary,

31

trapped vortex to alter the apparent local surface curvature and therefore the direction of the external flow. Perkins and Hazen[15] used a suction slot near the trailing edge of an airfoil and an upstream cavity to trap a vortex near the trailing edge and reported substantial lift ($C_L = 1.2$) at zero angle of attack at relatively low (3%) suction coefficient. Mandl[16] used a split flap located on the pressure side of an airfoil combined with suction (at the flap) to trap a vortex and to enforce tangential flow near the trailing edges of the airfoil and the flap and alter the Kutta condition of the airfoil.

III.4 EXPERIMENTAL APPARATUS AND PROCEDURE

The present experiments use a modular NACA 4415 airfoil model. The 2-D airfoil (shown schematically in Figure III.2) has a chord measuring 461 mm and maximum thickness to chord ratio $t/c = 0.15$ and spans the entire wind tunnel test section (which measures approximately 1 m on the side). The center section of airfoil model is equipped with two configurations of modular spanwise synthetic jet actuators each having a rectangular orifice measuring 140 x 0.5 mm. One configuration of actuators can be installed within the streamwise domain $0.09 < x/c < 0.315$ where the jets are flush mounted and issue normal to the surface of the airfoil. In a second configuration, a separate jet actuator is integrated with a miniature flap having a characteristic height of 0.016c. The Jet Integrated Flap (*JIF*) is movable along the surface of the airfoil on the pressure side (Figure III.2). In both configurations, the actuator jets are driven by several piezoelectric membranes that are built into a central cavity and are operated at or near resonance. For both actuator configurations, streamwise fences are placed near the (spanwise) edges of the actuator orifices to maintain a nominally two-dimensional flow in the controlled section of the airfoil.
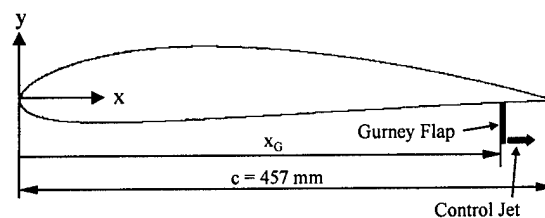

Figure III.2. Airfoil model

The airfoil is also instrumented with a circumferential array of 71 pressure ports (located at mid-span) that are each connected to an external high-speed pressure measurement system.

The velocity and vorticity fields in the cross-stream (x-y) plane, $z = 0$, above the airfoil (i.e., on the suction side) and in its wake are measured using particle image velocimetry (PIV). The flow is seeded with micron smoke particles and it is illuminated using a double-pulse ND-YAG laser. Image pairs are captured using a 1008 x 1016 pixel CCD camera with a magnification of 55.2 µm/pixel. In each image, the velocity vectors are computed using a standard cross-correlation technique. A given PIV map is averaged over 500 realizations (image pairs).

III.5 AERODYNAMIC PERFORMANCE WITH ACTIVE GURNEY FLAP

As discussed in Section III.3, the addition of a Gurney flap that scales on the order of a few percent of the chord length of a conventional airfoil can lead to an increase in lift that can be

accompanied by an increase or decrease in pressure drag. In the present work, the *JIF* is similar in some respects to a conventional Gurney flap and is mounted on a conventional (smooth) airfoil. The objective is to leverage the presence of the obstruction (and the altered baseline flow of the smooth airfoil) to further manipulate the Kutta condition of the airfoil to achieve global flow modifications and potentially improve the airfoil's overall aerodynamic performance. An important element of this approach is that it is implemented at low angles of attack and requires relatively low actuation input by leveraging the presence of the flap as a baseline.

The aerodynamic characteristics of the present *JIF* was compared with a "conventional" $0.014c$ surface-normal Gurney flap when both are mounted flush with the trailing edge of the baseline (smooth) airfoil. The bulk of the experiments reported here are conducted at $Re_c = 460,000$ (based on the free stream velocity and the chord of the airfoil). Figures III.3a-c show the variations with angle of attack ($-4° < \alpha < 8°$) of the lift and (pressure) drag coefficients (C_L and C_{Dp}) and of the lift to pressure drag ratio (L/D_p), respectively, while Figure III.3d is the corresponding pressure drag polar. Data for the baseline (smooth) airfoil, the airfoil combined with the conventional Gurney flap, and the *JIF* are shown. The addition of a conventional Gurney flap leads to an increase in the lift coefficient (nominally 0.12) that is almost invariant over the entire range of angles of attack tested here (Figure III.3a). As shown in Figure3b, the addition of a Gurney flap to the present (cambered) airfoil results in an increase in pressure drag
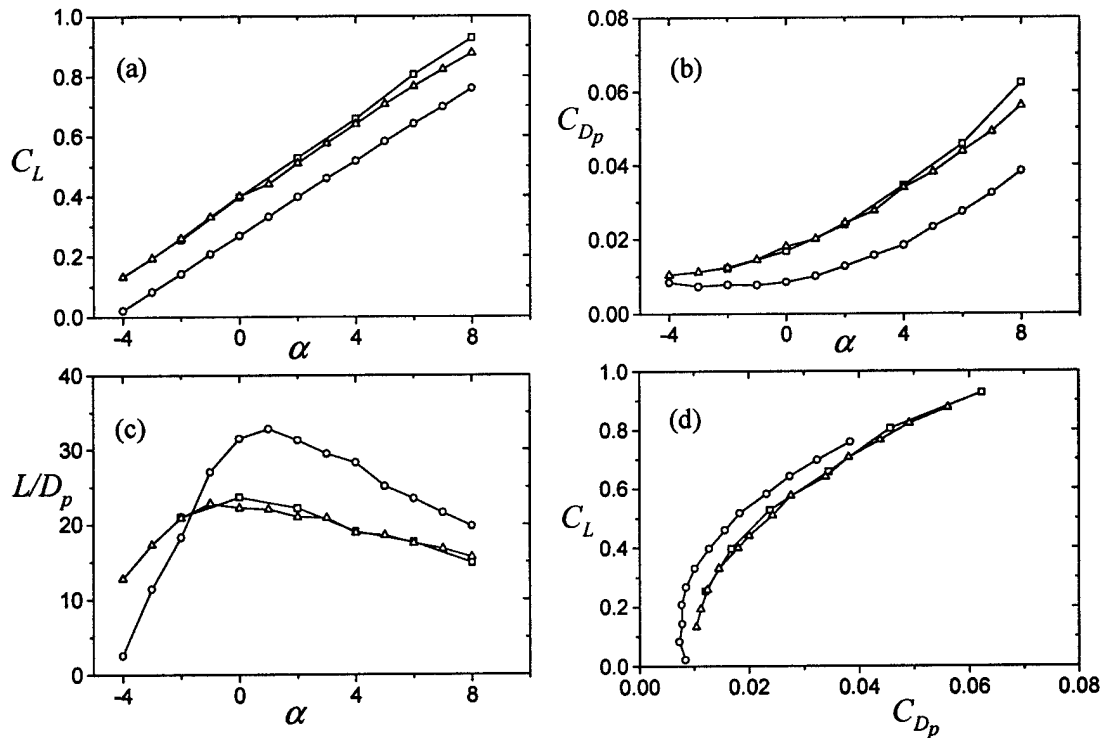

Figure III.3. The variations with angle of attack of the C_L (a), C_{Dp} (b), and L/D_p (c) and the corresponding pressure drag polar (d). (O) Smooth, (Δ) Gurney flap and (□) JIF.

from 112% at $\alpha = 0°$ to 46% at $\alpha = 8°$. Similar trends were also observed in the studies on cambered airfoils by Jeffrey et al.[12] and Giguère et al.[13] as well as in the CFD results of J Jang[11]. In these cases, C_L and C_D increase at a given angle of attack with addition of the Gurney flap.

Despite the increase in lift, the addition of the Gurney flap at the trailing edge results in a decrease in the lift to drag ratio (L/D_p) for $\alpha > -2°$. For smaller angles of attack, L/D_p with the Gurney flap is higher than for the smooth airfoil. The data in Figure III.3 show that the aerodynamic characteristics of the baseline airfoil combined with the present jet integrated flap are reasonably similar to what is measured with the conventional Gurney flap. While the *JIF* yields a slightly higher lift coefficient for $\alpha > 2°$ (Figure III.3a), there is also a small increase in the drag coefficient (Figure III.3b) such that L/D_p is almost the same within the range $2° < \alpha < 8°$.
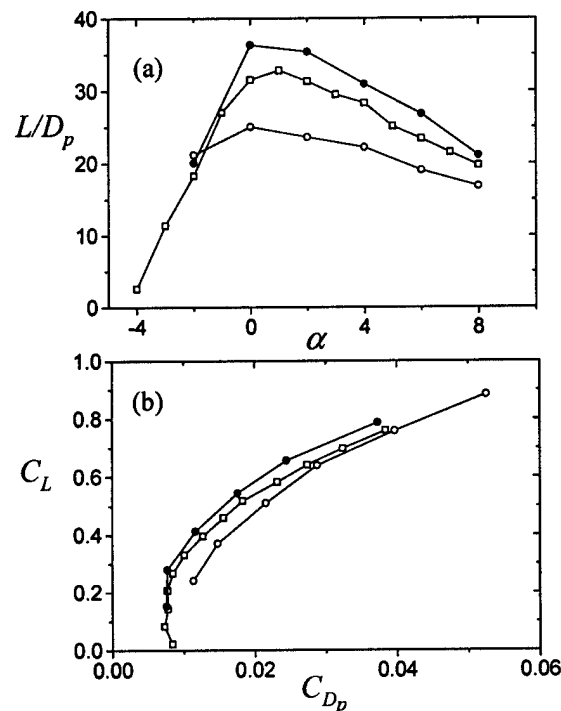
The effect of jet actuation on the pressure distribution around the airfoil when the *JIF* is placed at $x_G/c = 0.94$ is shown in Figures III.4a and b for $\alpha = 0°$ and $8°$, respectively, (the location of the downstream edge of the *JIF* is marked with a dashed line). The pressure distribution in the absence of actuation (open symbols) shows that for $x/c < 0.8$ and similar to a conventional Gurney flap as indicated by Giguère et al.[13], the unactuated *JIF* leads to respective decrease and increase in the pressure coefficient (which corresponds to an increase in the lift) on the suction and pressure surfaces of the airfoil. It is remarkable that these changes are measurable as far upstream as $x/c = 0.1$. Compared to the smooth airfoil, the increase in lift that results from the decrease in pressure downstream from the suction peak on the top surface is ostensibly accompanied by increased (downward) turning of the flow above the airfoil and a concomitant
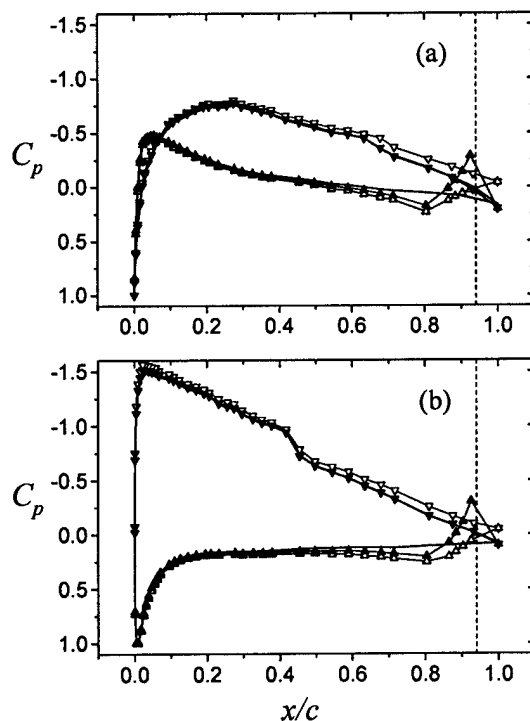
Figure III.4. *The pressure distribution around the airfoil for $\alpha = 0°$ (a) and $8°$ (b). The downstream edge of the JIF is marked with a dashed line ($x_G/c = 0.94$). (———) Smooth, ($\triangle$) unactuated JIF and ( ) actuated JIF.*

reduction in the pressure coefficient at the trailing edge. However, as noted in connection with Figure III.3b, the increase in lift is also accompanied by an increase in pressure drag. The presence of the *JIF* on the pressure surface of the airfoil results in slight blockage that peaks near $x/c = 0.80$ followed by an almost linear decrease of the pressure towards the trailing edge.

The actuation of the jet ($C_\mu = 8 \times 10^{-3}$) results in a localized low pressure domain between the downstream edge of the actuator and the trailing edge of the airfoil as is evidenced by the presence of a suction peak at $x/c = 0.93$ where the pressure coefficient is lower than in the absence of actuation while the pressure at the trailing edge of the airfoil is higher when the jet is active. In fact, it is remarkable that when the jet is active, the pressure distribution along the entire upper (suction) surface of the airfoil is lower than in the absence of actuation and is virtually identical to the pressure distribution of the smooth airfoil. At the same time, while the pressure distribution along the pressure side of the airfoil is generally lower than when the jet is inactive, it is still higher than for the smooth airfoil. Up to $x/c = 0.80$ (where there is a local maximum) the pressure distributions in the presence and absence of the actuation are rather similar. However, the low-pressure domain that is present near the airfoil's trailing edge appears to migrate upstream towards the *JIF* when the jet is activated. As will be shown in Figure III.9 below, the actuation results in upward turning of both flows along the lower (pressure) and upper (suction) surfaces towards the trailing edge, which accounts for the increase in the trailing edge pressure. The upward tilt is clearly commensurate with the reduction in lift that is caused by the appearance of the suction peak on the lower surface ($x/c = 0.93$). The upward turning of the flow near the trailing edge is similar to the turning (vectoring) of a primary jet towards a low-pressure interaction domain that is induced by an adjacent synthetic jet actuator which was investigated in detail by Smith and Glezer[17].

Figure III.5. (a) The variation of L/D_p with angles of attack, and (b) the pressure drag polar. (□) Smooth, (O) unactuated JIF and (●) actuated JIF.

The effect of the actuation on the aerodynamic characteristics of the airfoil for angles of attack within the range $-2° < \alpha < 8°$ is shown in Figure III.5. As shown in Figure III.3c, although the addition of the *JIF* at $x_G/c = 0.94$ results (in the absence of actuation) in an increase in lift, however, an increase in pressure drag leads to an overall decrease in L/D_p compared to the baseline (smooth) airfoil. When actuation is applied ($C_\mu = 8\times10^{-3}$), there is a substantial increase in L/D_p (Figure III.5a) compared to both the baseline and the unactuated *JIF* airfoils over the entire range of angles of attack. At this streamwise position of the *JIF*, the maximum lift to pressure drag ratio is obtained at $\alpha = 0°$ ($L/D_p = 36.3$), which is an increase of 45% over the unactuated *JIF* airfoil, but more significantly an increase of 15.3% over the smooth airfoil. The corresponding pressure drag polar (Figure III.5b) shows that for a given lift coefficient, there is a decrease in the pressure drag compared to both the unactuated *JIF* and smooth airfoils. As C_L increases, the decrement in pressure drag increases relative to the smooth airfoil and decreases relative to the unactuated *JIF* airfoil.
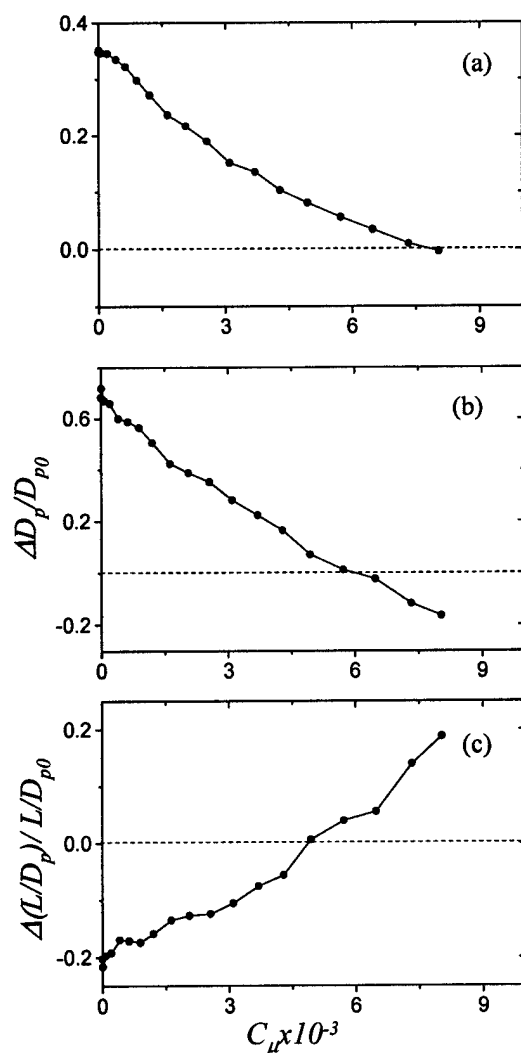

Figure III.6. Variation with C_μ of the normalized increments in the (a) lift, (b) pressure drag, and (c) L/D.

36

The effectiveness of the actuation can be continuously varied with the magnitude of the control jet momentum coefficient C_μ (e.g., Amitay et al.[6]). Figures III.6a-c show the variation with C_μ of the normalized increments (relative to the smooth airfoil) in the lift, pressure drag, and lift to drag ratio, respectively at $\alpha = 0°$. For the unactuated *JIF* case (i.e., $C_\mu = 0$), the respective increases in lift and drag are 35% and 68%, and the corresponding decrease in L/D_p is 20%. As C_μ is increased, there is a monotonic decrease in both the normalized lift and pressure drag and an increase in L/D_p. Apparently, the rate of decrease with C_μ of the normalized pressure drag is larger than that of the normalized lift, and the lift to pressure drag ratio of the smooth airfoil is attained at $C_\mu = 4.9 \times 10^{-3}$ when the lift and drag coefficients are each 8% larger than for the smooth airfoil. The increase in pressure drag for the actuated *JIF* case vanishes at $C_\mu \approx 6 \times 10^{-3}$ while C_L is still 4.5% higher than for the smooth airfoil. Compared to the smooth airfoil, at the highest actuation level that was achieved with the present actuators ($C_\mu = 8 \times 10^{-3}$), L/D_p increases by 19%, the pressure drag decreases by 16% while the lift is nominally unchanged.

These data show that the aerodynamic performance of a conventional airfoil can be continuously varied by adding a small (Gurney flap like) obstruction integrated with a fluidic actuator. In fact, the aerodynamic performance of the airfoil can be varied from a configuration that is essentially an airfoil with a conventional Gurney flap through an airfoil that has similar performance as that of the smooth (baseline) airfoil to an airfoil that has higher lift to pressure drag ratio.

The effects of the actuation on the airfoil's moment coefficient and on the center of pressure (about $c/4$) are shown in Figures III.7a and b, respectively for $-2° < \alpha < 8°$. The center of
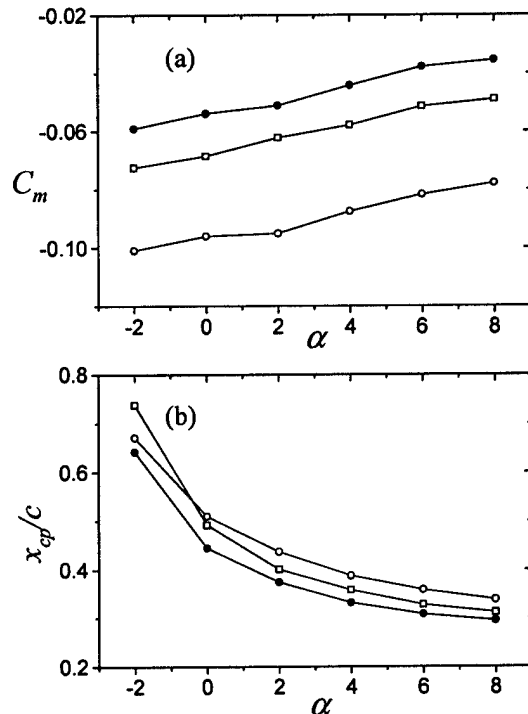

Figure III.7. The variation with α of the (a) moment coefficient and (b) the center of pressure

37

pressure moves forward as the angle of attack is increased (from $0.74c$ to $0.31c$ for the smooth airfoil). As shown in Figure III.7a, the addition of the unactuated *JIF* (which increases lift) moves the center of pressure aft ($0.50c$ at $C_L = 0.4$) and the full range of actuation moves it somewhat aft ($0.38c$ at $C_L = 0.4$) relative to the smooth airfoil. Because of the increase in lift that is associated with the placement of the *JIF* on the smooth airfoil, the moment coefficient is more negative (compared to the smooth airfoil) indicating increased stability (Figure III.7a). Apparently, the suction that is induced by the actuation jet near the trailing edge of the airfoil contributes to a pitch up moment and therefore to a reduction in C_m although it is still negative over the entire range of angles of attack.

In general, use of the actuation at the maximum attainable C_μ results in a decrease in lift and a larger decrease in pressure drag, resulting in an increased L/D_p ratio. The effects of actuation are also evident in the pressure distribution, which shows a low-pressure region upstream of the jet. In addition, the increased suction and pressure that appear on the suction and pressure sides of the airfoil, respectively, when the anactuated *JIF* is used, are diminished when actuation is applied.

The effect of the streamwise placement of the *JIF* on the lower (pressure) surface of the airfoil was investigated over a range of angles of attack (for $C_\mu = 8 \times 10^{-3}$). Figures III.8a and b show the variation of the lift and pressure drag with (normalized) x_G/c for $\alpha = 0°$ and $8°$. These data show that for $x_G/c < 0.7$ the effect of the *JIF* (in the presence or absence of actuation) is small at both angles of attack. Compared to the smooth airfoil, the presence of the *JIF* within this streamwise domain results in small reduction in C_L and C_{Dp}. Near the trailing edge of the airfoil, in the absence of actuation the *JIF* leads to an increase in both lift and pressure drag. The addition of
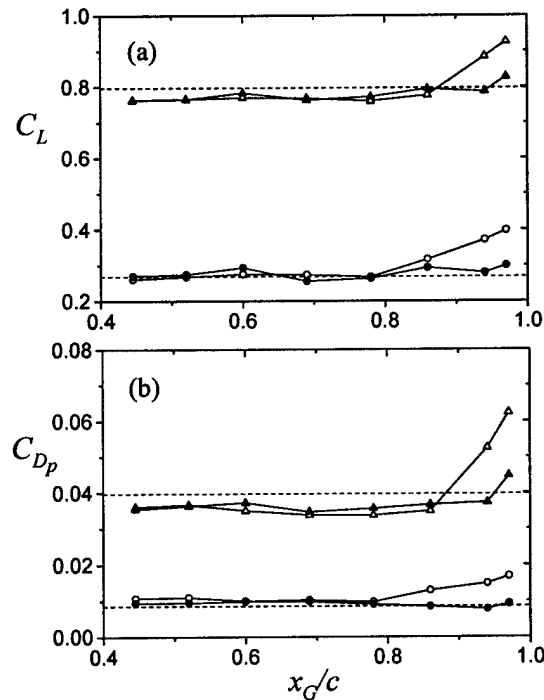

Figure III.8. *The variation of the (a) lift and (b) pressure drag with x_G/c for $\alpha = 0°$ (O) and $8°$ ($\triangle$). Solid and open symbols correspond to the actuated and the unactuated cases, respectively.*

actuation results in a decrease in lift (which is almost invariant with angle of attack) and a reduction in pressure drag. However, the reduction in pressure drag as a result of the actuation increases with angle of attack (46% and 29% at $\alpha = 0°$ and 8°, respectively). It is noteworthy that for $x_G/c < 0.75$, the actuation results in a slight increase in pressure drag ostensibly as a result of the suction that is induced by the presence of the actuation jet.

The flow field in the vicinity of the airfoil's trailing edge is investigated using particle image velocimetry (PIV) in the x-y plane ($z = 0$). Each measurement field is comprised of 7 partially
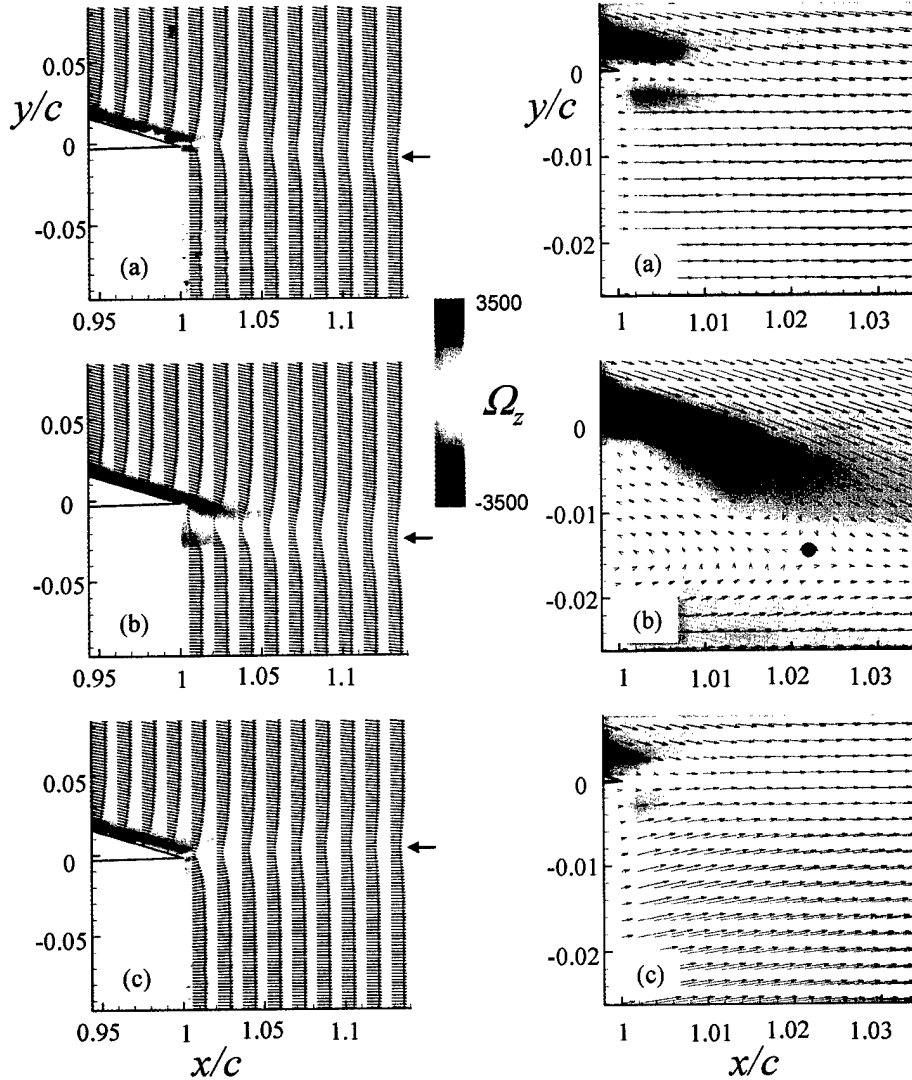

Figure III.9. *Global views of superimposed time-averaged maps of spanwise vorticity and cross-stream velocity vectors for the smooth airfoil (a), and with the JIF in the absence (b) and presence (c) of actuation.*

Figure III.10. *As in Figure III.9, magnified views of superimposed time-averaged maps of spanwise vorticity and cross-stream velocity vectors.*

39

overlapping frames measuring 5.56cm x 5.61cm where each frame is computed from an ensemble of 500 realization pairs. Figures III.9a-c show composite views of time-averaged maps of cross stream vorticity (that also include regularly-spaced cross stream velocity vectors profiles) in the streamwise domain $0.95 < x/c < 1.14$ for the smooth (baseline) airfoil and for the airfoil with the mounted *JIF* in the absence and presence of actuation. In the present experiments, the laser illumination is provided from above, and therefore the flow below the airfoil (which also includes the *JIF*) is shadowed by the airfoil and is not visible here. The outline of the airfoil surface near the trailing edge is included in each frame.

The evolution of the near wake of the smooth airfoil is shown for reference in (Figure III.9a). The boundary layers on the top and bottom surfaces (marked by clockwise (CW) and counter clockwise (CCW) vorticity concentrations, respectively) merge downstream of the trailing edge and commensurate with the (small) lift at $\alpha = 0°$, the center of the wake (as marked by local velocity minima) is turned downward. The presence of the *JIF* ($x_G/c = 0.94$) results in cross-stream spreading of the wake and stronger downward tilt (Figure III.9b). Compared to the smooth airfoil's wake, the (CCW) vorticity layer near the lower (pressure) surface of the airfoil is thicker and appears to be more intense. As shown in Figure III.11 (below) the presence of the unactuated *JIF* leads to organized (time-periodic) shedding of vortices that scale with the thickness of the (CCW) vorticity layer (nominally $0.02c$) near the trailing edge) and apparently merge into the airfoil's wake. One of the prominent features of the near wake in Figure III.9b is the local increase in its cross-stream width immediately downstream of the trailing edge compared to the smooth airfoil. A magnified view of the domain $1 < x/c < 1.03$ is shown in
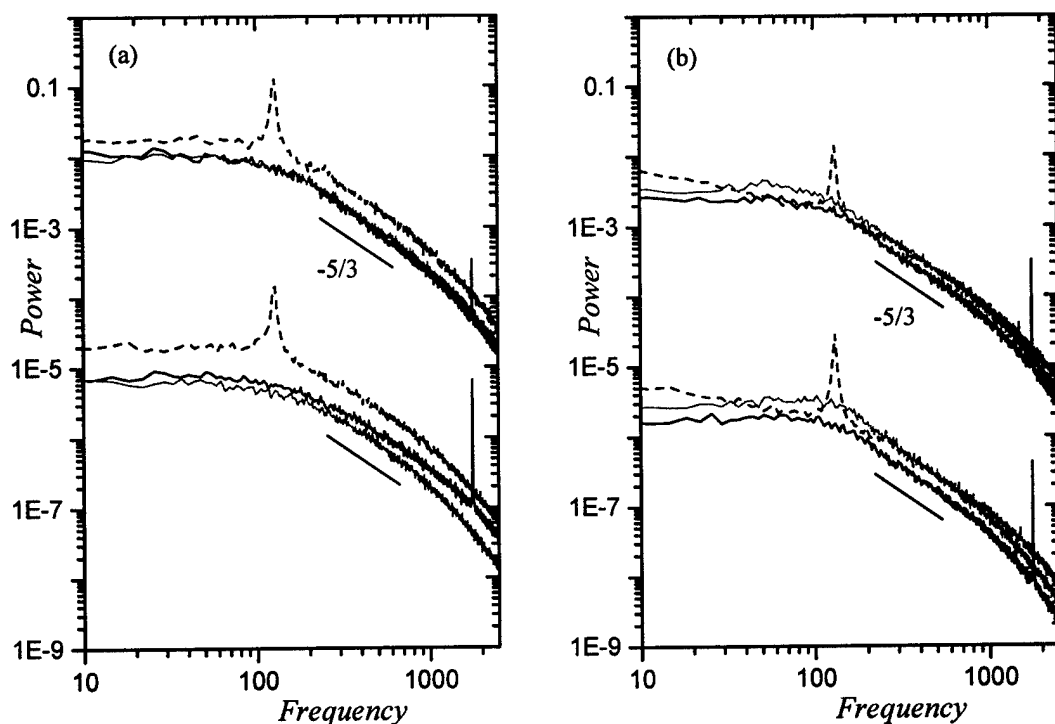
Figure III.11. Power spectra of the velocity magnitude within the wake at x/c = 1.03 (a) and 1.55 (b) for the smooth airfoil ( ), and for the unactuated (- - -) and actuated JIF (___) configurations.

40

Figure III.10b (the magnified view for the smooth airfoil is shown for reference in Figure III.10a). This image shows that the flux of vorticity from the top and bottom eliminated and the flow is turned strongly upward.

Power spectra of the velocity magnitude measured (using a single hot wire sensor) within the wake at $x/c = 1.03$ and 1.55 are shown in Figures III.11a and b, respectively for the smooth airfoil, and for the unactuated and actuated *JIF* configurations. The spectra were measured on both sides of the wake at cross-stream elevations where the velocity deficit is half the maximum deficit. For clarity, the spectra measured at the lower part of the wake are shifted vertically downwards by three decades. The power spectra of the smooth airfoil are virtually featureless and are shown for reference (gray curve) in each of the plots. The spectra of the unactuated *JIF* flow (dashed line) at $x/c = 1.03$ (Figure III.11a) exhibit a strong spectral peak at 128 Hz on both sides of the wake. This peak is apparently associated with the shedding frequency of an organized vortex train that is induced by the *JIF* (on the pressure side) just upstream of the trailing edge. (The spectrum at the upper part of the wake also includes a weak spectral peak at the first harmonic) Similar vortex shedding in the presence of a conventional Gurney flap at the trailing edge of an Eppler e423 airfoil was observed by Jeffrey el al.[12]. It is noteworthy that while there is an overall reduction in the magnitude of all spectral components at $x/c = 1.55$ (Figure III.11b), the magnitude of the spectral peak at the shedding frequency remains relatively unchanged relative to the other (background) components.

The changes in the power spectra in the presence of actuation are remarkable in that the spectral component at the vortex shedding frequency vanishes completely and a spectral component at the actuation frequency (1770 Hz) appears within the dissipation range of the flow. At $x/c = 1.03$, this peak is somewhat weaker on the upper side of the wake, but by $x/c = 1.55$ (Figure III.11b) the magnitude of this peak is almost equal on both sides of the wake (although smaller than at the low side of the wake at $x/c = 1.03$). Another feature of the spectra of the actuated flow at $x/c = 1.03$ is that the magnitude of all spectral components (and ostensibly of the total kinetic energy) is considerably smaller than the corresponding components in the absence of actuation (i.e., with the *JIF* alone). In fact, with the exception of the spectral peak at the actuation frequency, the spectra of the smooth airfoil and of the actuated flow are virtually identical on the top side of the wake. However, on the bottom side of the wake the spectral components of the actuated flow are larger than the corresponding components of the smooth flow (although still smaller than for the unactuated flow). As expected, note that the kinetic energy that is imparted to the flow by the actuation is primarily concentrated within a frequency band around the actuation frequency. The increase in the magnitude of spectral components above the actuation frequency suggests enhanced energy transfer at these scales and therefore enhanced dissipation. Figure III.11b shows probably the most profound effect of the actuation on the wake flow. At this location, all the spectral components in the actuated flow (except at the actuation frequency) are lower (on both sides of the wake) than in the wakes of the smooth airfoil and the airfoil with the unactuated *JIF*. It is remarkable that the effect of the actuation reduces the power (and turbulent kinetic energy) at both low and high frequencies suggesting that the actuation affect the entire energy cascade within the flow and effects enhanced dissipation.

41

III.6 CONCLUSIONS

The objective of the control approach described here is to reduce the pressure drag at low angles of attack with minimal or no penalty in lift. The pressure distribution on the surface of the airfoil is modified using virtual aero-shaping that is achieved by the formation of a stationary recirculating flow domain next to the surface as a result of the interaction between the cross flow and a high-frequency synthetic jet actuator placed downstream from a miniature surface-mounted passive obstruction. The formation of this interaction domain alters the flow above the airfoil by inducing a displacement of the local streamlines that is sufficient to modify the surface pressure distribution even at small angles of attack.

In the present work, the height of the obstruction (above the surface of the airfoil) is $h = 9.3 \cdot 10^{-3} c$ (i.e., less than 1% of the chord) and it is placed at $x_o/c = 0.22$ where the synthetic jet actuator is located immediately downstream of the obstruction. The experiments are conducted at $Re_c = 381,000$ for which the baseline flow is fully attached to the surface of the airfoil for $\alpha < 8°$.

The interaction domain between the actuator and the cross flow is investigated using high-magnification particle image velocimetry in the x-y plane ($z = 0$). The characteristic streamwise scale of the induced recirculating flow domain is varied by changing the actuation frequency (F^+ is varied between 1.25 and 7.8) and/or the jet strength (C_μ varies between $1.7 \cdot 10^{-4}$ and $1.2 \cdot 10^{-3}$). The present work shows that the streamwise length of the interaction domain and its cross stream penetration increase with decreasing actuation frequency and jet momentum coefficient. Phase-averaged PIV images show that for $C_\mu = 1.2 \cdot 10^{-3}$, at given actuation frequency the streamwise length of the interaction domain is typically comparable to one to two wavelengths of the actuation frequency. The interaction domain contains one strong clockwise vortex and a second weaker vortex (from the earlier actuation cycle) is advected downstream and rapidly loses its identity. However, a reduction in C_μ by an order of magnitude (to $1.7 \cdot 10^{-4}$) significantly lengthens the interaction domain indicating that it does not merely scale with the actuation frequency. For example, at $F^+ = 7.8$ (850 Hz) the length of the interaction domain increases from $1.1 \cdot \lambda_{act}$ to $2 \cdot \lambda_{act}$ and at lower actuation frequency for which F^+ is 1.25 the decrease in C_μ results in a mismatch between the interaction domain and flow separation.

As a result of the changes in the curvature of the interaction domain, the induced low-pressure (suction) peak on the airfoil diminishes and widens with the actuation frequency and jet momentum coefficient leading to a substantial increase in pressure drag and a reduction in lift. It is remarkable that a significant decrease in the baseline pressure drag (compared to its magnitude) with minimal penalty in lift is only achieved at *higher* actuation frequencies ($f_{act} = 850$ Hz). The present results also show that at high actuation frequencies the aerodynamic forces (and the shape of the interaction domain) are substantially less sensitive to changes in the jet momentum coefficient.

REFERENCES

[1]Hsiao, F-B, Liu, C-F, and Shyu, J-Y (1990). "Control of wall-separated flow by internal acoustic excitation". *AIAA J. 28*(8), 1440-1446.

[2]Seifert, A., Bachar, T., Koss, D., Shepshelovich, M. and I. Wygnanski, I. (1993). "Oscillatory blowing: A tool to delay boundary-layer separation". *AIAA J. 31*(11), 2052-2060.

[3]Chang, R.-C., Hsiao, F.-B., and Shyu, R.-N (1992). "Forcing Level Effects of Internal Acoustic Excitation on the Improvement of Airfoil Performance". *Journal of Aircraft 29*(5), pp. 823-829.

[4]Smith, D. R., Amitay, M., Kibens, V., Parekh, D. E. and Glezer, A. (1998). "Modification of Lifting Body Aerodynamics using Synthetic Jet Actuators", AIAA Paper 98-0209.

[5]Amitay, M., Kibens, V., Parekh, D. E. and Glezer, A. (1999). "Flow Reattachment Dynamics over a Thick Airfoil Controlled by Synthetic Jet Actuators". AIAA Paper 99-1001.

[6]Amitay, M., Smith, D. R, Kibens, V., Parekh, D. E. and Glezer, A. (2001). "Aerodynamic Flow Control over an Unconventional Airfoil Using Synthetic Jet Actuators". *AIAA J.* 39(3), 361-370.

[7]Erk, P. P. (1997) "Separation Control on a Post-Stall Airfoil Using Acoustically Generated Perturbations". Ph.D. Dissertation, Technische Universitat Berlin, Germany.

[8]Chatlynne, E., Rumigny, N., Amitay, M., and Glezer, A. (2001). "Virtual Aero-Shaping of a Clark-Y Airfoil using Synthetic Jet Actuators", AIAA Paper 2001-0732.

[9]Amitay, M., Horvath, M. Michaux, M. and Glezer, A. (2001). "Virtual Aerodynamic Shape Modification at Low Angles of Attack using Synthetic Jet Actuators". AIAA Paper 2001-2975.

[10]Liebeck, R.H. (1978). "Design of Subsonic Airfoils for High Lift. *Journal of Aircraft 15*(9), pp. 547-561.

[11]Jang, C., Ross, J., and Cummings, R. (1992). "Computational Evaluation of an Airfoil with a Gurney Flap". AIAA Paper 92-2708.

[12]Jeffrey, D., Zhang, X., and Hurst, D. (2000). "Aerodynamics of Gurney Flaps on a Single-Element High-Lift Wing". *Journal of Aircraft 37*(2), pp. 295-301.

[13]Giguère, P., Lemay, J., and Dumas, G. (1995). "Gurney Flap Effects and Scaling for Low-Speed Airfoils". AIAA Paper 95-1881.

[14]Myose, R., Papadakis, M., and Heron, I. (1998). "Gurney Flap Experiments on Airfoils, Wings, and Reflection Plane Model". *Journal of Aircraft 35*(2), pp. 206-211.

[15]Perkins, C.D. and Hazen, D. (1953). "Some recent advances in Boundary Layer and Circulation Control". Forth Anglo-American Aeronautical Conference.

[16]Mandl, P. (1959). "Effect of Standing Vortex on Flow about suction aerofoils with Split Flaps". *Nat. Res. Council of Canada, Aero. Rep. No.* 234.

[17]Smith, B. L. and Glezer, A. (1998). "The Formation and Evolution of Synthetic Jets". *Physics of Fluids*, Vol. 10, No. 9.

43

IV. INTERACTION OF A SYNTHETIC JET WITH A TURBULENT BOUNDARY LAYER

IV.1 OVERVIEW

The interaction of a synthetic jet with a cross-flow fully developed turbulent boundary layer over a flat plate is investigated. Unlike the interaction of the jet with the cross flow over an aerodynamic body, in the present configuration, the coupling between local interaction and global aerodynamic effects is removed. The focus of this work is the documentation of the most salient flow features of two distinct flow regimes where the jet scales either with the inner (viscous) sub-layer or with the entire boundary layer. The streamwise pressure gradient, which is nominally zero, is invariant throughout the experiment.

IV.1. FLAT PLATE BOUNDARY LAYER MODEL

The flat plate model forms one of the short walls of a 25.4 × 45.7 cm test section of a closed-return wind tunnel. In order to provide complete optical access, the working surface is displaced into the test section by 5.1 cm from the original plane of the tunnel wall thus reducing the cross-sectional area to 25.4 × 40.6 cm. A fairing section transitions the flow from outlet of the contraction, and occupies the first 26.7 cm of the test section. The flat plate model includes a 10.2 cm long spanwise suction module immediately downstream of the leading edge fairing where the flow rate (5.2 × 10^{-3} m^3/sec maximum) is controlled by a needle valve and monitored by a Meriam Laminar Flow Element. The plate allows for modular installation of the actuator in order to vary its streamwise position and is instrumented with static pressure ports. The two synthetic jet actuator modules were used. One module is driven by eight piezoelectric disks and has an orifice width of 0.51 mm, while the second module is driven by two loudspeakers and has an orifice width of 1.91 mm. Both jet orifices span the center 15.2 cm of the test section.

In all experiments, the boundary layer was tripped by a 3 cm long strip of 60-grit sandpaper that was fastened to surface at the contraction outlet. The thickness of the boundary layer could be increased by a 3.2 mm tall fence that was placed at the downstream edge of the suction section. This design enables variations of the boundary layer thickness δ (at the orifice of the jet actuator) between 10 and 40 mm.

IV.2 CHARACTERIZATION OF THE BASELINE BOUNDARY LAYER

In order to ensure that the boundary layer at the measurement station is fully turbulent, a strip of 60-grit sandpaper is installed at the outlet of the contraction. Normalized boundary layer profiles for the baseline flow are shown in Figure IV.1a at two different streamwise locations ($X = 406$ mm & 762 mm, measured from the outlet of the contraction). There is little variation in the normalized profile for $5 \leq U_\infty \leq 12.5$ m/s. The boundary layer profiles at the conditions at which synthetic jet interaction is studied are plotted in wall units (y^+, U^+) in Figure IV.1b in order to compare to the universal distribution proposed by Coles (1956) for the velocity profile outside of the viscous sub-layer: $U^+ = 1/\kappa \ln y^+ + C + (\Pi/\kappa)\varpi(y/\delta)$. Where $U^+ \equiv \bar{u}/U_T$ and $y^+ \equiv yU_T/v$, and the friction velocity (U_T) is defined by the wall shear stress, $U_T \equiv (\tau_w/\rho)^{0.5}$. The constants $\kappa = 0.41$ and $C = 5.0$, are generally considered to be invariant with respect to Reynolds number (Erm & Joubert, 1991). The third term in the above equation is known as "the law of the wake" and applies primarily to the outer region of the boundary layer. For the experimental conditions used in §§IV.3, IV.4 and IV.5 ($Re_\theta = 520, 2,100, \& 710$,
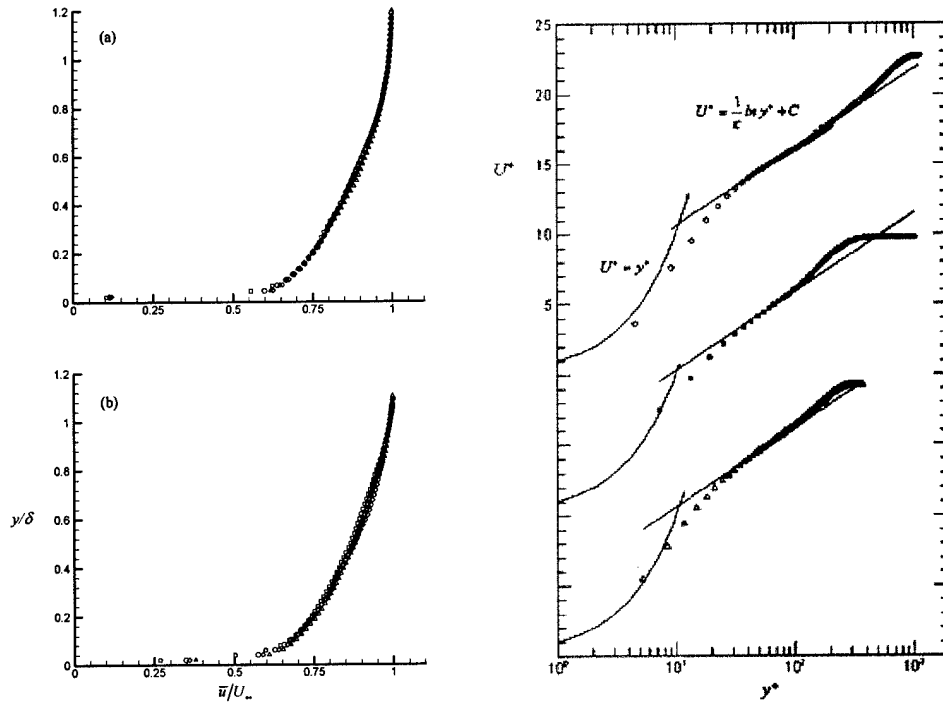
Figure IV.1. a) Normalized velocity profiles, (a) x = 406 mm (b) x = 762 mm: U∞ = 5.0 (□), 7.5 (O), 10.0
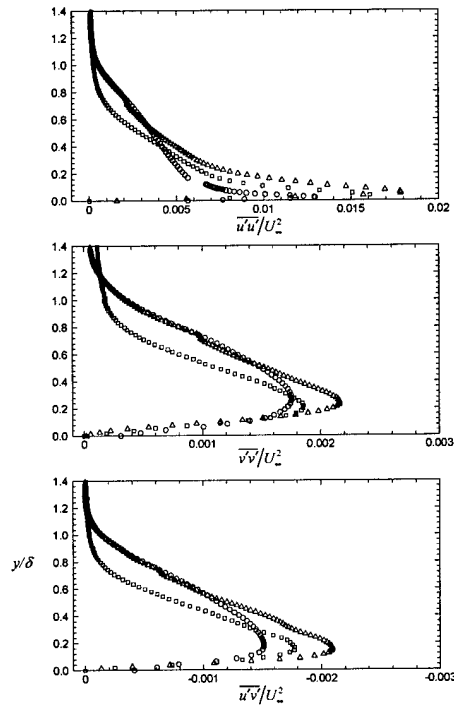
Figure IV.2. Reynolds Stresses: Reθ = 520 (△), 710 (□), and 2,100 (O).

45

respectively), it is apparent that the present velocity distributions include a logarithmic region. At $Re_\theta = 520$ and 2,100 reasonable agreement with the universal distribution is found for $\kappa = 0.41$ and $C = 5.0$ with $U_T = 0.106$, and 0.445 m/s, respectively. At $Re_\theta = 710$, the data was found to fit the universal distribution with $U_T = 0.405$ m/s with $\kappa = 0.41$ and $C = 4.7$. Within the viscous sub-layer $U^+ = y^+$, where the edge of this part of the boundary layer occurs near $y^+ \sim 15$. Cross-stream distributions of Reynolds stresses within the baseline boundary layers are shown in Figure IV.2. The distributions at the three Reynolds numbers are qualitatively similar and magnitude of the peak stresses, which occur near the inner edge of the logarithmic region, are in agreement with the levels within fully turbulent boundary layers at similar Reynolds numbers reported by Erm & Joubert (1991). Based on these comparisons of the mean streamwise velocity and turbulent stresses, the baseline boundary layers in the present investigation are judged to be fully turbulent. A detailed discussion of the characteristics of low Reynolds number ($Re_\theta <$ 6,000) turbulent boundary layers downstream from various tripping devices can be found in a paper by Erm & Joubert (1991), that also includes an extensive review of earlier work.

IV.3 CLOSED RECIRCULATION REGIONS

As shown in earlier work, the interaction between a synthetic jet and cross-flow leads to the formation of a closed recirculation region if the dimensionless formation frequency, $\hat{f}$, is above some critical value. This dimensionless frequency is defined as the product of Strouhal number (based on jet orifice width) and dynamic pressure ratio (jet to cross-flow). The characteristic features of closed recirculation regions are investigated in turbulent boundary layer where $Re_\theta = 500$, $\delta/b = 73$, $St_\delta = 21$, for $\overline{U}_j/U_\infty = 3.0$, 4.0, 5.0 and 6.0. (The dimensional parameters are $U_\infty = 2.0$ m/s, $\delta = 37.0$ mm, $\theta = 4.0$ mm, $b = 0.51$ mm, $f = 1130$ Hz, and $\overline{U}_j = 6.0$, 8.0, 10.0 & 12.0 m/s). The local dimensionless frequencies are $\hat{f} = 0.6$, 1.2, 1.8, and 2.6, all well above the critical value (0.1) at which a closed recirculation region forms.

The time-averaged flow field in the vicinity of the synthetic jet actuator orifice is measured within twelve partially overlapping sets of PIV images acquired at 33.1 μm/pixel (see table A.2). Concentration maps of normalized time-averaged spanwise vorticity, $\zeta_z \equiv (\delta/U_\infty)\zeta_z$, are shown in Figure IV.3 (Left) (positive vorticity is CCW). The closed recirculation regions are outlined using the streamline $\psi = 0$, where the streamfunction is computed by cross-stream integration of the streamwise velocity component, with $\psi = 0$ at the surface of the plate. It is apparent that the penetration of the synthetic jet increases with dynamic pressure ratio in a similar manner to a conventional jet in cross flow. The synthetic jet's counter rotating vortex pairs appear as bands of positive and negative vorticity that are deflected downstream by the cross flow and dissipate rapidly. A closed recirculation region forms as the cross flow separates just upstream of the actuator orifice and reattaches farther downstream ($x/\delta = L_{bubble}$) forming a new dividing streamline ($\psi = 0$) between upstream and downstream stagnation points. The characteristic scale of the closed recirculation increases with dynamic pressure ratio ($L_{bubble}/\delta = 0.60$, 0.95, 1.1 and 1.2 for $VR = 3.0$, 4.0, 5.0 and 6.0, respectively), and a similar dependence of has also been observed by Mittal & Rampunggoon (2002). During each suction cycle the synthetic jet actuator draws in fluid originating both upstream and downstream from the orifice, removing some fluid from the recirculation bubble, and subsequently replacing it during the blowing cycle. A simple

46

analysis shows that the total volume of fluid moved through the actuator orifice during each half-cycle is less than 2 % of the volume of the recirculation region at every velocity ratio. Thus, the size of the recirculation region does not vary significantly over the actuation cycle. As the velocity ratio is increased, the aspect ratio of the recirculation region (length-to-height) changes from approximately 4 ($\overline{U}_j/U_\infty$ = 3.0 & 4.0) to 2 ($\overline{U}_j/U_\infty$ = 5.0 and 6.0).

The presence of the recirculation region clearly distorts the velocity field and alters the downstream evolution of the boundary layer. Distributions of the mean streamwise velocity are shown in Figure IV.3-Right at three streamwise locations for each velocity ratio. Upstream from the actuator orifice (x/δ = −0.5) the boundary layer is thicker than in the baseline, due to the blockage that is introduced by the synthetic jet. At x/δ = 0.5, there is a local velocity maximum near the outer edge of the recirculation region (defined by ψ = 0), which increases with velocity ratio. At higher cross-stream elevations the streamwise velocity is higher than the baseline at all velocity ratios, indicating that the cross flow is accelerated due to the displacement of the recirculation region. At this streamwise location the strong reverse flow with the recirculation region toward the actuator orifice is also evident. While downstream from the interaction domain the CW vorticity is quickly reorganized into a new inner layer immediately adjacent to the surface [cf. Figure IV.3 (Left)], the return to the velocity distribution of the baseline flow requires a much greater streamwise distance. At x/δ = 3, an inner region of the boundary layer is re-established for all velocity ratios, however the velocity distributions are still substantially distorted relative to the baseline flow. This is particularly evident as the velocity ratio is increased, due to the wake effect (or velocity deficit) that is associated with the blockage caused by the recirculation region. The velocity distribution for VR = 6.0 has a local maximum at the edge of the new inner layer, followed by a velocity deficit at higher elevations before reaching the free-stream velocity. It is noteworthy to mention that CCW vorticity is generated in the region between the outer jet flow and the newly formed inner layer downstream from the reattachment point of the recirculation region [Figure IV.3 (Left)]. The rapid development of the inner layer is also evident in the normalized wall shear stress, $\hat{\tau}_w = \tau_w/\left(\frac{1}{2}\rho U_\infty^2\right)$, shown in Figure IV.4-Left. At every velocity ratio, the blockage caused by the recirculation region causes lower shear stress upstream from the actuator orifice, compared to the baseline value. The shear stress is negative within the recirculation region, and then rapidly rises as the boundary layer redevelops downstream. At every velocity ratio, the shear stress reaches a maximum value within 1.5 δ from the reattachment point, confirming the rapid formation of the inner wall region within the boundary layer. Farther downstream, the streamwise variation of the shear stress is reduced as the velocity distribution relaxes to that of the baseline boundary layer.

The effect of the presence of the closed recirculation regions on the boundary layer's displacement thickness δ^*, momentum thickness θ, and shape factor $h_{12} = \delta^*/\theta$ are shown in Figure IV.4-Right. As the velocity ratio is increased, the displacement thickness within the interaction domain increases due to the increased height of the recirculation region [cf. Figure IV.3 (Left)]. Concomitantly, the convective acceleration of cross-flow fluid and the additional momentum injected by the synthetic jet result in substantial reduction of the momentum thickness within the interaction domain. The momentum thickness becomes negative for $\overline{U}_j/U_\infty$ = 4.0, 5.0 & 6.0, indicating that the flow contains more momentum than a uniform profile at U_∞. Downstream from the recirculation region, the increased momentum thickness

47

compared to the baseline flow is attributed to the wake effect that is evident in the velocity distribution (Figure IV.3-Right). The shape factor is reduced since a significant amount of momentum is transported into the newly formed inner layer (Figure IV.3-Right).

IV.4 JET PENETRATION SCALING WITH THE INNER LAYER

In this section, the interaction of a synthetic jet with the flat plate boundary layer is studied under conditions leading to the formation of discrete vortices that scale with the inner segment of a turbulent boundary layer. This investigation is carried out at $Re_\theta = 2,100$, $\delta/b = 61$, $\overline{U}_j/U_\infty = 1.25$, and $St_\delta = 3.5$ ($U_\infty = 10$ m/s, $\delta = 31.0$ mm, $\theta = 3.2$ mm, $f = 1130$ Hz, $\overline{U}_j = 12.5$ m/s, and $b = 0.051$ mm). The *local* dimensionless frequency at these parameters is $\hat{f} = 0.02$ (assuming the mean jet centerline velocity in the absence of cross-flow $10b$ from the exit plane is $\sim 0.5\ \overline{U}_j$). Phase-locked measurements are obtained at eighteen instances during the actuation cycle (in 20° increments) using ten overlapping sets of PIV images. Six sets of 400 images per phase were acquired at 10.4 μm/pixel to resolve the flow immediately adjacent to the wall, and four sets of 100 images per phase were acquired at a resolution of 46.9 μm/pixel to resolve the outer region of the boundary layer.

IV.4.1 The Velocity Field

The interaction between the synthetic jet and cross flow leads to the formation of discrete vortices having a characteristic cross section that is smaller than the boundary layer thickness (0.08δ), as shown in the phase-averaged maps of spanwise vorticity concentrations in Figure IV.5. The origin of the coordinate system is at the centerline of the actuator exit plane and $\phi = 0°$ corresponds with the beginning of the blowing phase of the cycle. Selected cross-stream velocity distributions are also included. The formation of the vortex pair during the blowing phase of the cycle is visible during $0° < \phi < 180°$ (Figure IV.5a-c). A fraction in the fluid expelled from the actuator rolls up into the vortex pair, resulting in a stem of jet fluid behind the vortex. The upstream (CCW) vortex, which is advected by faster moving flow, overtakes the CW vortex. During the suction phase ($180° < \phi < 360°$, Figure IV.5d-f) the boundary layer upstream from the actuator orifice becomes thinner as fluid is drawn into the actuator. The vortices quickly diminish in strength and completely disappear within three actuation wavelengths, indicating that there is a finite domain where the vortices directly influence the flow. In the time-averaged flow, the finite interaction domain appears as a stationary vortex adjacent to the surface and immediately downstream from the actuator orifice, as shown in Figure IV.6b (the baseline flow shown in Figure IV.6a). The time-averaged flow bears a remarkable resemblance to the quasi-steady closed recirculation regions discussed in the previous section. The height and width of the interaction domain (as characterized by the vorticity concentration) are approximately 0.08δ and 0.3δ, respectively. Downstream from the interaction domain, beginning at $x/\delta = 0.4$, the vorticity is reorganized into a thin layer adjacent to the surface.

Cross-stream distributions of the time-averaged streamwise velocity at four streamwise locations ($x/\delta = 0.13, 0.25, 0.5\ \&\ 1.0$) are shown in wall units in Figure IV.7 using the friction velocity of the baseline flow ($U_T = 0.445$ m/s). Immediately downstream from the actuator orifice ($x/\delta = 0.13$), the passage of discrete vortices results in a local maximum at $y^+ = 70$, and negative

48
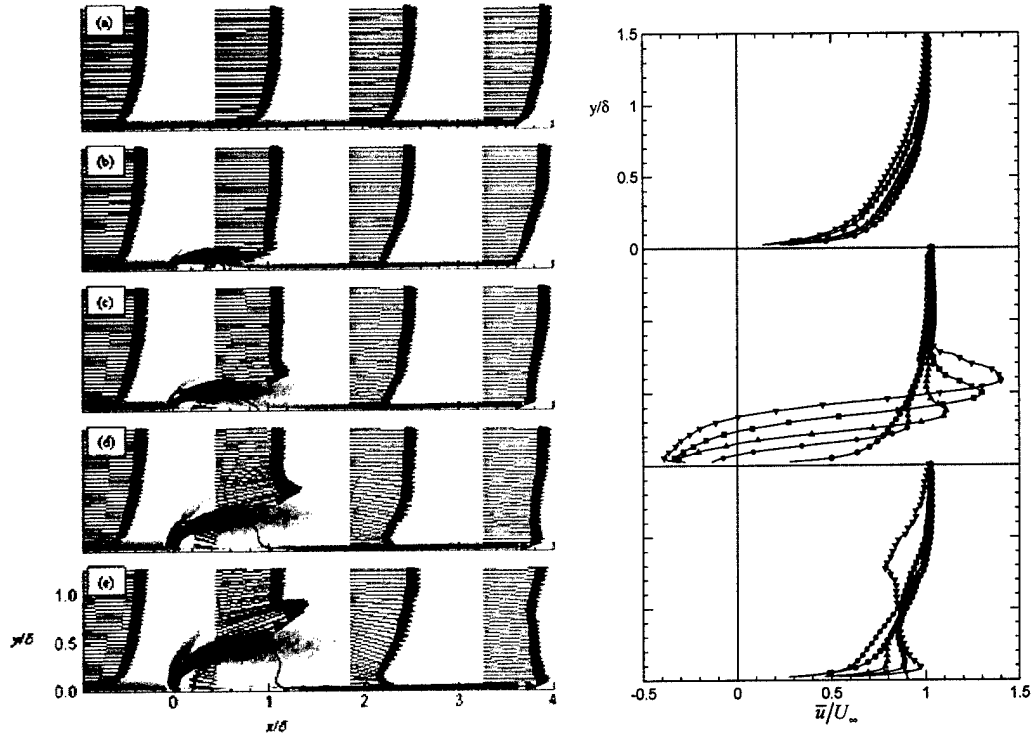
Figure IV.3. *Left: Normalized spanwise vorticity, and velocity, Re*θ *= 520, St*δ *= 21, δ/b = 73: (a) baseline, (b)* $\overline{U}_j/U_\infty$ *= 3.0, (c) 4.0, (d) 5.0, and (e) 6.0.* ψ *= 0 is superimposed, and Right: Mean velocity: baseline (O),* $\overline{U}_j/U_\infty$ *= 3.0 (●), 4.0 (▲), 5.0 (■), and 6.0 (▼). x/*δ *= -0.5, 0.5, and 3.0 (from top to bottom).*
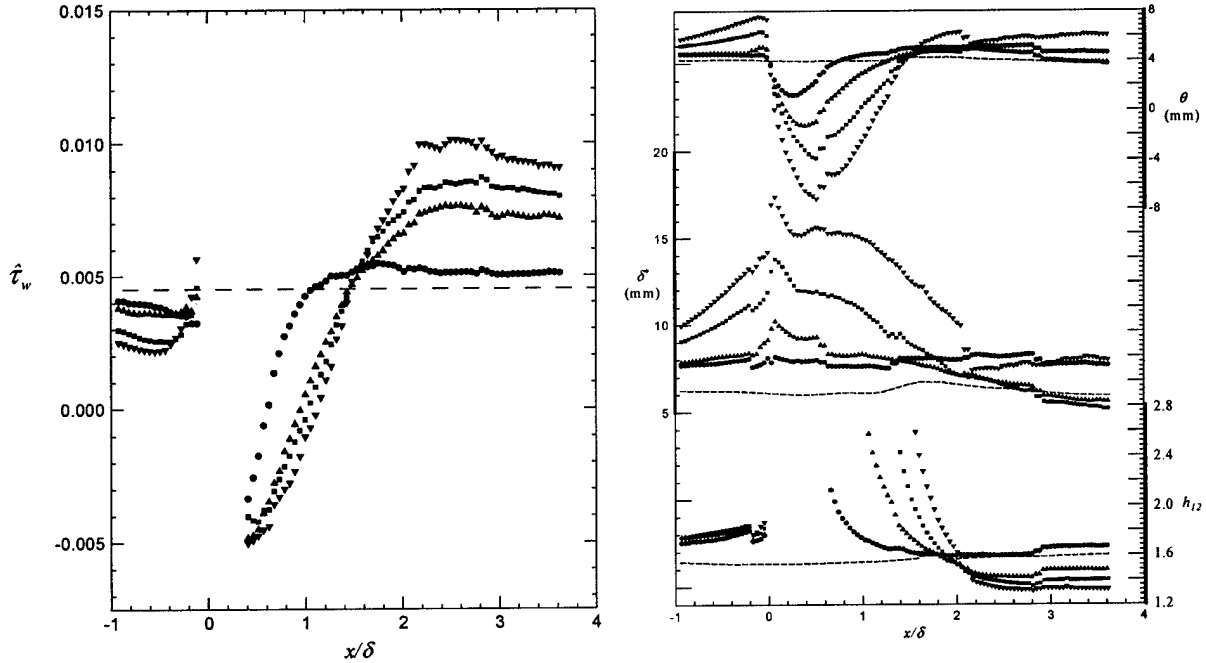
Figure IV.4. *Left: Normalized wall shear stress,* $\overline{U}_j/U_\infty$ *= 3.0 (●), 4.0 (▲), 5.0 (■), and 6.0 (▼). The baseline stress is indicated using a dashed line. Right: Boundary layer displacement thickness, momentum thickness and shape factor:* $\overline{U}_j/U_\infty$ *= 3.0 (●), 4.0 (▲), 5.0 (■), and 6.0 (▼). The baseline quantities are shown by the dashed lines.*

49
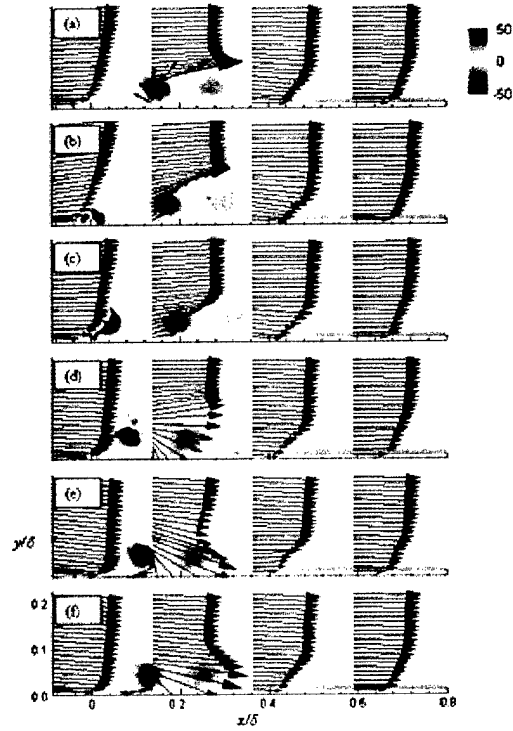
Figure IV.5. Phase-averaged normalized vorticity, $Re\theta = 2,100$, $\delta/b = 61$, $St\delta = 3.47$, and $\overline{U}_j/U_\infty = 1.25$: (a) $\phi = 0°$, (b) 60°, (c) 120°, (d) 180°, (e) 240°, and (f) 300°.
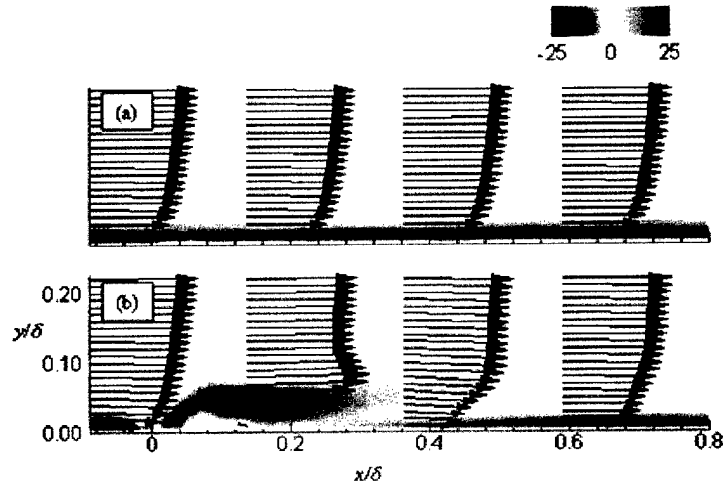
Figure IV.6. Time-averaged vorticity with superimposed velocity vectors: (a) baseline, (b) actuated.

50

velocity adjacent to the wall. Beyond $y^+ = 200$ there is little influence on the mean velocity profile. At $x/\delta = 0.25$ the mean velocity adjacent to the wall is significantly lower than in the baseline, but not reversed. The displacement of the velocity maximum induced by the vortices to a slightly higher elevation ($y^+ = 80$) indicates the cross stream spreading of their cores as they travel downstream. This trend continues at $x/\delta = 0.5$, with a slight perturbation associated with velocity induced by the CW vortices located at $y^+ = 100$. In the region downstream from the interaction domain, the velocity distributions are multi-tiered, with an inner region adjacent to the wall ($y^+ < 20$, at $x/\delta = 0.5$), a middle region that contains the remnants of vorticity from the coherent structures ($20 < y^+ < 200$), and finally an outer region of the boundary layer ($y^+ > 200$), which appears to be unaffected by the interaction.

Since the vortices formed by the interaction rapidly diminish in strength as they are advected downstream, the largest velocity fluctuations are confined to the interaction domain, as illustrated in the three normalized components of Reynolds stress ($\overline{u'u'}/U_\infty^2$, $\overline{v'v'}/U_\infty^2$, and $\overline{u'v'}/U_\infty^2$) shown in Figure IV.8. Within this domain, all three components of Reynolds stress are much higher (at least one order of magnitude) than the corresponding levels within the baseline turbulent boundary layer. Cross-stream distributions of the normal and shear components of Reynolds stress are shown at five streamwise locations ($x/\delta = 0.13, 0.25, 0.5, 1.0, \& 1.5$) in Figures IV.9-Left and IV.9-Right, respectively. From this data it is immediately apparent that the Reynolds stresses are rapidly attenuated with downstream distance from the actuator orifice, returning to values that are close to those in the baseline boundary layer by $x/\delta = 1.5$. Additionally, the velocity fluctuations induced by the interaction are confined to the inner part of the boundary layer ($y/\delta < 0.4$). The distribution of $\overline{u'v'}/U_\infty^2$ at $x/\delta = 0.13$ (Figure IV.9-Righta) changes sign close to wall, ostensibly the result of mean reverse flow immediately downstream from the actuator orifice (cf. Figure IV.7).

IV.4.2 The Pressure Field

The phase-averaged pressure gradients within the interaction domain are computed using the Navier-Stokes equations along with triple decomposition of the velocity field data. The normalized, phase-averaged cross-stream $\left[< \partial \hat{p} / \partial \hat{y} >= \delta / \tfrac{1}{2} \rho U_\infty^2 < \partial p / \partial y >\right]$ and streamwise $\left[< \partial \hat{p} / \partial \hat{x} >= \delta / \tfrac{1}{2} \rho U_\infty^2 < \partial p / \partial x >\right]$ gradients are shown for six phases of actuation in Figure IV.10. Each discrete vortex produces large gradients in both coordinate directions, which diminish rapidly with distance from the actuator orifice, further indicating the finite nature of the interaction domain. The time-averaged modification of the pressure gradients within this region are shown in Figure IV.11, computed from the Reynolds-averaged Navier-Stokes equations. Notice that the time-averaged gradients within the interaction domain ($0 \leq x/\delta \leq 0.3$) have a qualitatively similar structure compared to the phase-averaged gradients associated with a single vortex. Thus, although the time-averaged flow does not exist in reality, the interaction between the synthetic jet and cross flow leads to the formation of a time-averaged stationary vortex. The time-averaged normalized pressure, plotted in Figure IV.12, is computed using a combined-path Runge-Kutta integration scheme, with the boundary condition $\overline{p}(x,\infty) = 0$. (The pressure is computed as gage pressure using the local static pressure as the reference.) The lowest pressure, $\overline{p} = -0.55\left(\tfrac{1}{2} \rho U_\infty^2\right)$, in the flow is near the center of the time-averaged stationary vortex ($x/\delta =$

51
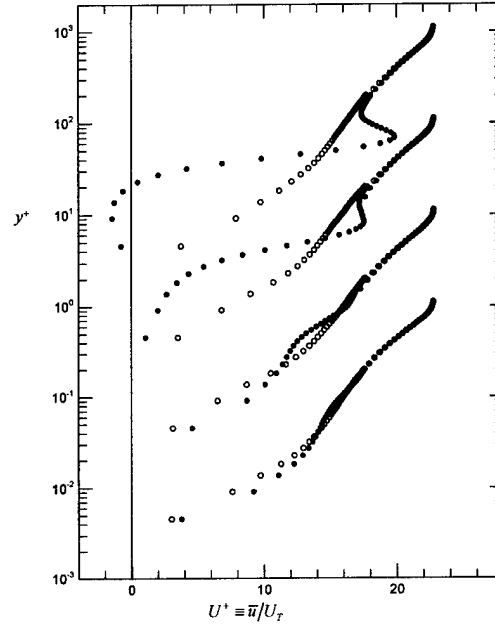
Figure IV.7. *Time-averaged velocity profiles in wall units. From top to bottom, $x/\delta = 0.13$, 0.25, 0.5, & 1.0, with successive locations separated by one decade.*
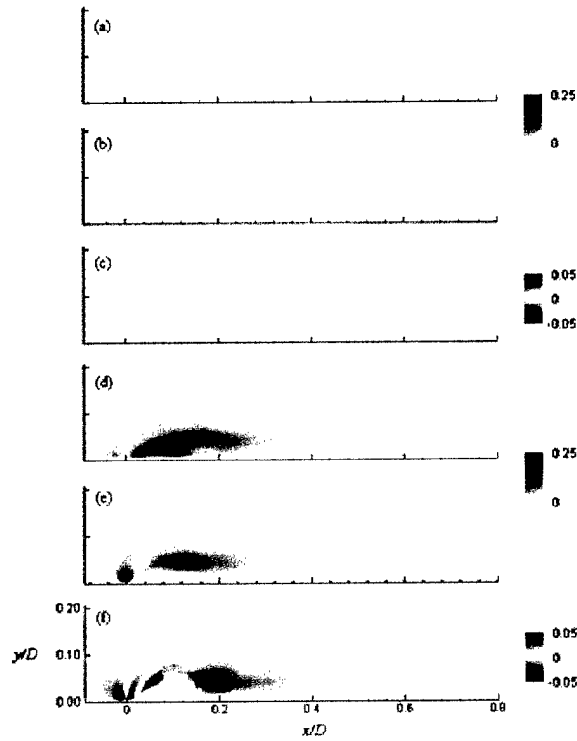
Figure IV.8. $\overline{u'u'}/U_\infty^2$, $\overline{v'v'}/U_\infty^2$ and $\overline{u'v'}/U_\infty^2$ baseline (a), (b), and (c), and actuated (d), (e) and (f).
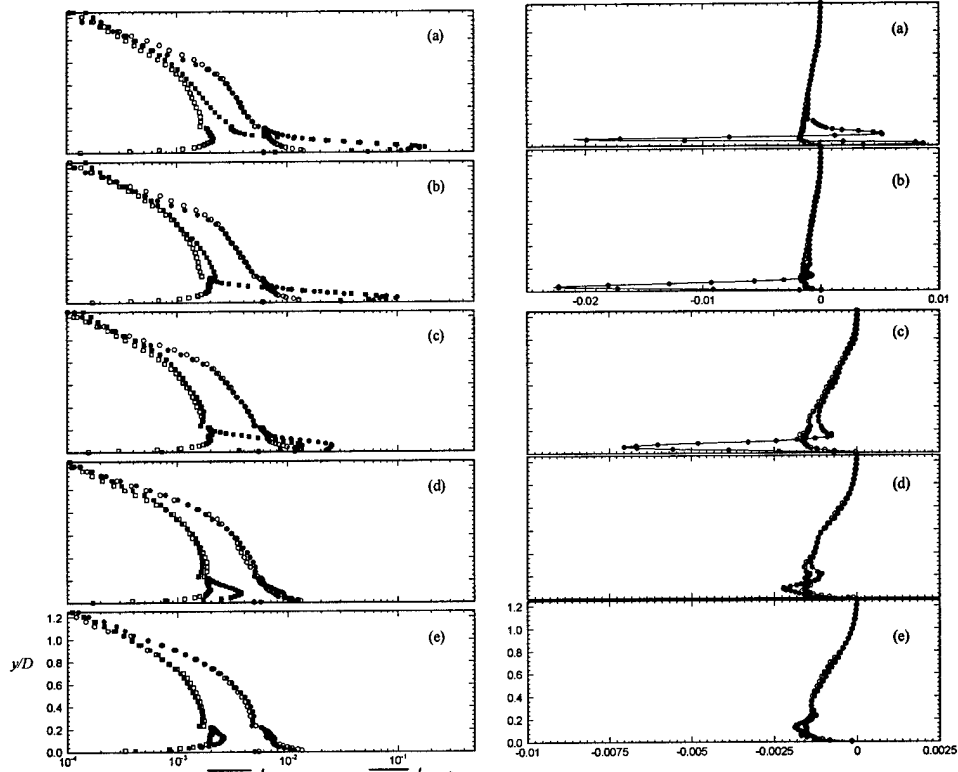
52

Figure IV.9. Distribution of Left $\overline{u'u'}/U_\infty^2$, and $\overline{v'v'}/U_\infty^2$: baseline: (○),(□); and actuated:(●), (■) and Right: $\overline{u'v'}/U_\infty^2$: baseline (○), actuated (●). $x/\delta = 0.13$ (a), 0.25 (b), 0.5 (c), 1.0 (d), and 1.5 (e). Note the change in ordinate.
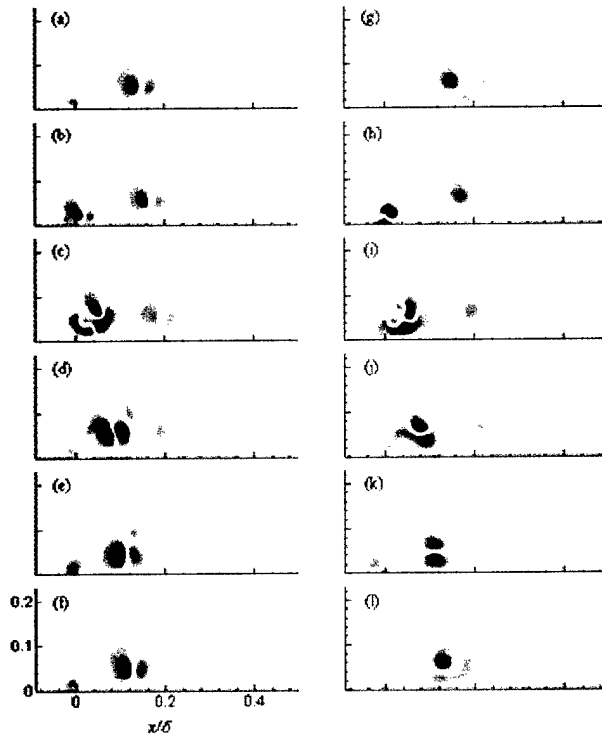
Figure IV.10. Phase-averaged normalized pressure gradients, $<\partial\hat{p}/\partial\hat{x}>$ (a)-(f); $<\partial\hat{p}/\partial\hat{y}>$ (g)-(l): (a, g) $\phi = 0°$, (b, h) 60°, (c, i) 120°, (d, j) 180°, (e, k) 240°,and (f, l) 300°.

53
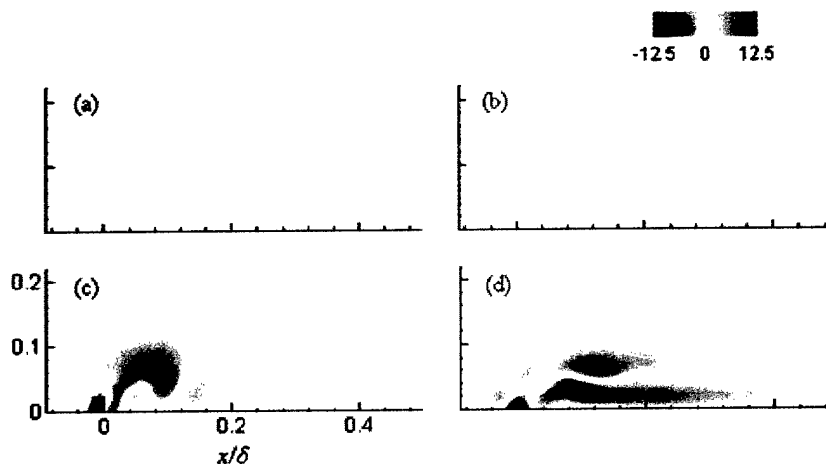
Figure IV.11. Normalized Reynolds-averaged pressure gradient $\partial\overline{p}/\partial\hat{x}$ and $\partial\overline{p}/\partial\hat{y}$ baseline (a) & (b); actuated (c) & (d).
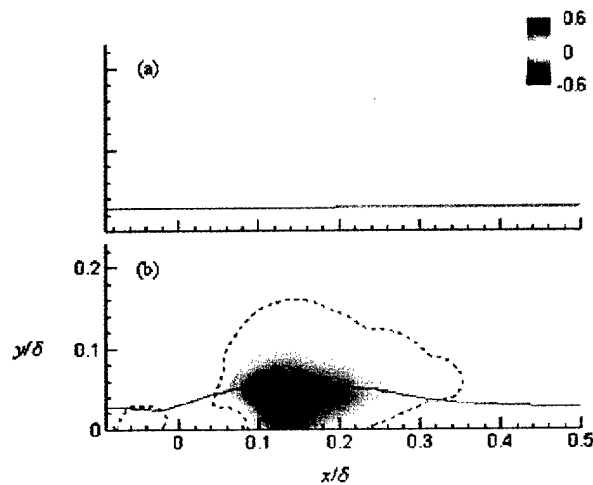
Figure IV.12. Normalized pressure field with $\hat{\psi} = 0.01$ superimposed: (a) baseline, (b) actuated. Dashed line indicates least significant contour of negative pressure, $\overline{p} = -0.025\left(\frac{1}{2}\rho U_\infty^2\right)$

$0.12, y/\delta = 0.04$). The displacement of the cross flow around the interaction domain is evidenced by the streamline $\hat{\psi} = \psi / U_\infty \delta = 0.01$.

IV.4.3 Boundary Layer Evolution

The normalized surface shear stress $\left[\hat{\tau}_w = \left(\mu / \tfrac{1}{2}\rho U_\infty^2\right)\left(\partial \bar{u} / \partial y\right)\right]$, plotted in Figure IV.13, further demonstrates the fact that the direct influence of the discrete vortices is confined to a finite domain. Within the interaction domain, there are large fluctuations in $\hat{\tau}_w$ associated with the passage of coherent vortices. The actuation wavelength (distance between successive vortices) is approximately $\lambda_{act} \approx 0.12\delta$, easily determined from successive local minima in shear, indicates that the vortex celerity ($U_c = f\lambda_{act}$) is approximately 0.4 U_∞. Since the CW vortices ($\zeta_z < 0$) are stronger and closer to the surface (cf. Figure IV.5), there is a reduction in the time-averaged shear stress within the interaction domain ($0 < x/\delta < 0.3$). Further downstream, the time-averaged shear is higher than that present in the baseline due to the formation of an inner layer in flow (cf. Figure IV.7). Interestingly, downstream from the interaction domain there are small phase-averaged oscillations in the shear stress about the time-averaged value, that may be the result of pressure waves. Notice that for $\phi = 0°$, $60°$, and $120°$ the phase-averaged wall shear stress is uniformly higher than the time-average (by about 5 %) within the domain ($0 < x/\delta < 0.3$). Within this domain, the time- and phase-averaged shear stress are approximately equal at $\phi = 180°$, while the phase-averaged stress is uniformly lower for $\phi = 240°$, and 300.

The alteration of the boundary layer characteristics due to jet actuation is shown in Figure IV.14. In the baseline flow, the boundary layer displacement and momentum thickness monotonically increase with downstream distance. At the location of the actuator orifice the thickness based on 0.99 U_∞ is 31.0 mm. The shape factor remains constant over the measurement domain at $h_{12} = 1.38$, a typical value for a fully turbulent boundary layer (Schlichting, p. 454, 1979). As seen in the velocity profiles (cf. Figure IV.7), the synthetic jet produces large changes in the boundary layer within the interaction domain ($0 < x/\delta < 0.5$). In this region, the cross-flow is displaced (increased δ^*) and accelerated (reduced θ), which brings about large changes in the shape factor. Downstream from the interaction domain δ^*, θ, and h_{12} return to their baseline values within one boundary layer thickness.

IV.4.4 Turbulent Kinetic Energy

High frequency actuation has previously been shown to enhance dissipation in free shear flows (Wiltse & Glezer, 1998). In the bluff body aerodynamics experiments, some of the reduction in turbulent kinetic energy within the separated shear layer may be due to this effect. The present data allows direct computation of the turbulent kinetic energy, as well as the rates of turbulent production and turbulent viscous dissipation within the interaction domain. The governing equation for turbulent kinetic energy equation in Cartesian coordinates is:

$$\tfrac{1}{2}\rho \frac{D}{Dt}\left(\overline{q^2}\right) = -\frac{\partial}{\partial x_i}\left[\overline{u_i'\left(p' + \frac{\rho\overline{q^2}}{2}\right)}\right] - \rho\overline{u_i'u_j'}\frac{\partial \bar{u}_j}{\partial x_i} + \frac{\partial}{\partial x_i}\left[\mu\,\overline{u_j'\left(\frac{\partial u_i'}{\partial x_j} + \frac{\partial u_j'}{\partial x_i}\right)}\right] - \mu\overline{\left(\frac{\partial u_i'}{\partial x_j} + \frac{\partial u_j'}{\partial x_i}\right)\frac{\partial u_i'}{\partial x_j}}$$

55
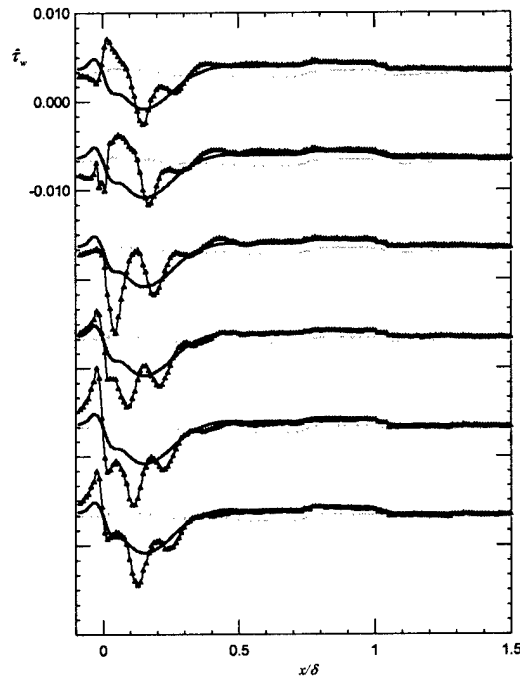
Figure IV.13. Normalized wall shear stress: (△) phase-averaged, from top to bottom, φ = 0°, 60°, 120°, 180°, 240°, and 300°; ━━ baseline; ─ ─ ─ actuated. Successive phases separated by 0.01
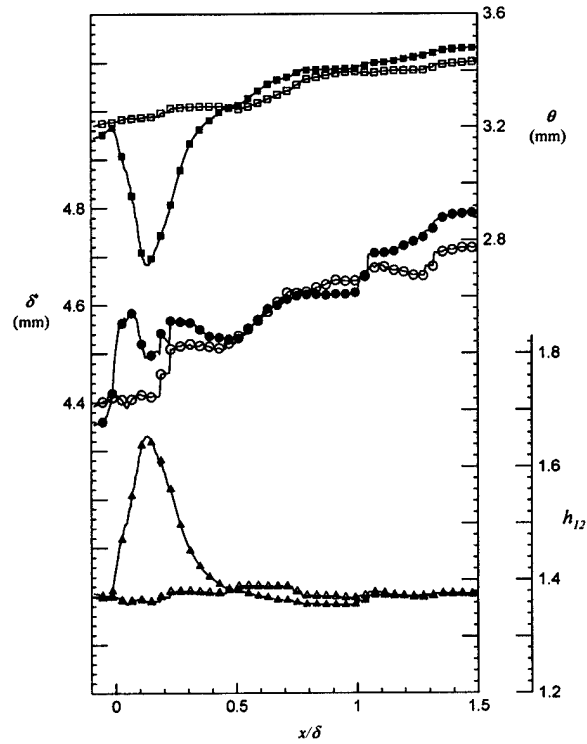
Figure IV.14. Boundary layer evolution, baseline: δ* (○), θ (□), h12 (△); actuated: δ* (●), θ (■), h12 (▲).

56

where $q^2 = (u')^2 + (v')^2 + (w')^2$, repeated indices indicate summation, and over-bars indicate time-averages. A derivation of this equation can be found in <u>Viscous Fluid Flow</u> by White (1974). The left hand side of the equation is the total rate of change of the turbulent kinetic energy, while the terms on the right hand side are the rates of convective diffusion, production, viscous work, and viscous dissipation, respectively. The time averaged turbulent kinetic energy $\hat{q}$, rate of turbulence production $\hat{P}$, and rate of viscous dissipation $\hat{\varepsilon}$ are shown in Figure IV.15 for the baseline and actuated flows. These quantities are computed from the PIV data assuming the flow to be two-dimensional (i.e. $w \equiv 0$, and $\partial(\ )/\partial z = 0$), and are normalized such that

$$\hat{q}^2 = \overline{q}^2 / U_\infty^2, \quad \hat{P} = -\rho \overline{u_i' u_j'}(\partial \overline{u}_j / \partial x_i)/(\tfrac{1}{2}\rho U_\infty^2 (U_\infty/\delta)), \text{ and}$$

$\hat{\varepsilon} = \mu \overline{(\partial u_i'/\partial x_j + \partial u_j'/\partial x_i)(\partial u_j'/\partial x_i)}/(\tfrac{1}{2}\rho U_\infty^2 (U_\infty/\delta))$. It is likely that the turbulence production can be computed to reasonable accuracy using the above assumptions, since the neglected terms contain either the mean spanwise velocity component ($\overline{w}$), or spanwise derivatives of the mean streamwise and cross-stream velocities all of which are likely to be very nearly zero. Although w' is definitely non zero, and its omission will likely lead to errors in the turbulent kinetic energy and dissipation, its contribution was not included.

In the baseline flow, turbulent kinetic energy is distributed throughout the boundary layer (profiles of $\overline{u'u'}$ and $\overline{v'v'}$ are shown in Figure IV.2) while the highest levels of production and viscous dissipation are adjacent to the wall. In the actuated flow, the levels of $\hat{q}^2$, $\hat{P}$, and $\hat{\varepsilon}$ within the interaction domain are an order of magnitude greater than those present in the baseline flow. Negative turbulence production, occurring near the actuator orifice, is interpreted as a transfer of energy from the periodic jet motion, into the mean flow. The total amount of turbulent kinetic energy within the boundary layer $\hat{q}^2$, as well as the total rates of $\hat{P}$, and $\hat{\varepsilon}$ as a function of x are determined by integrating these quantities in the cross-stream direction. Namely,

$$\hat{Q}^2(x) = \frac{1}{\delta}\int_{y=0}^{0.21\delta}\hat{q}^2(x,y)\,dy, \quad \underline{\hat{P}}(x) = \frac{1}{\delta}\int_{y=0}^{0.21\delta}\hat{P}(x,y)\,dy, \text{ and } \hat{E}(x) = \frac{1}{\delta}\int_{y=0}^{0.21\delta}\hat{\varepsilon}(x,y)\,dy.$$

These quantities are integrated across the full extent of the high-resolution data ($0 \leq y/\delta \leq 0.21$) and their streamwise variation is shown in Figure IV.16 for the baseline and actuated flows. In the baseline flow, $\hat{Q}^2$ is invariant with streamwise distance, since the rates of turbulence production and viscous dissipation are balanced. The large increase in turbulent kinetic energy within the interaction domain is immediately apparent, and its peak value occurs at $x/\delta = 0.11$. The turbulence production and viscous dissipation are also greatly elevated within the interaction domain. Downstream from the interaction domain, all three quantities rapidly decay, and by $x/\delta = 1$ have almost recovered their baseline values. However, in contrast to high-frequency excitation in free shear flows, the total amount of turbulent kinetic energy within the flow does not fall below the baseline value.
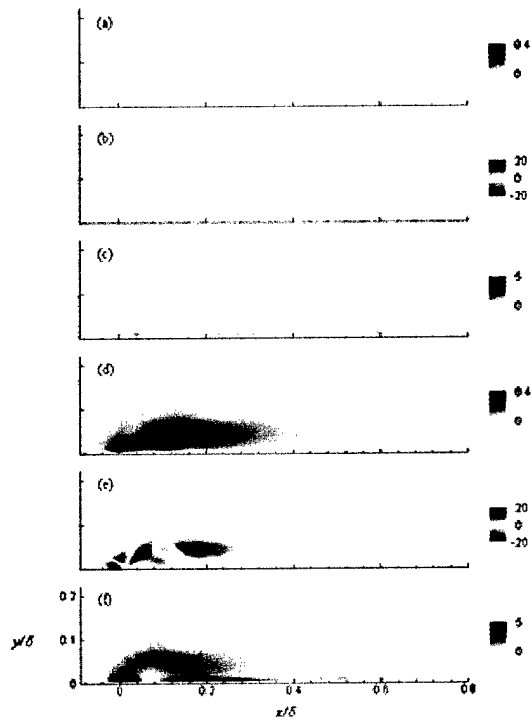
Figure IV.15. Normalized turbulent kinetic energy: $\hat{q}^2$, $\hat{P}$, $\hat{\mathcal{E}}$ baseline (a), (b), & (c), and actuated (d),(e), &
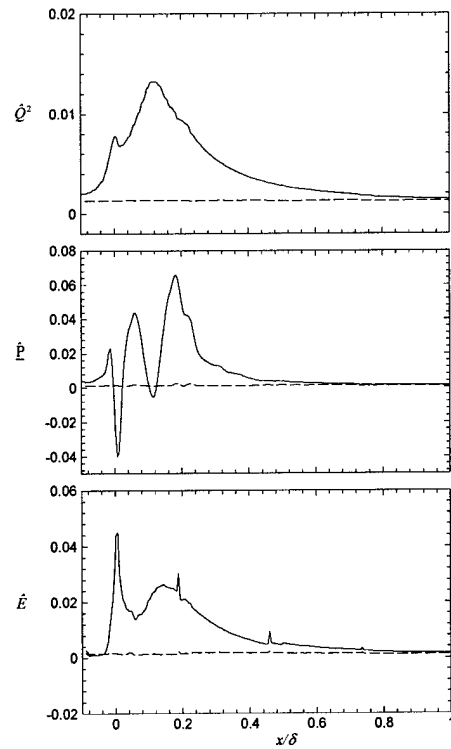

Figure IV.16. Integrated turbulent kinetic energy budget: $\hat{Q}^2$ (a), $\underline{\hat{P}}$ (b), and $\hat{E}$ (c); The baseline is dashed.

58

The rapid attenuation of turbulent kinetic energy downstream from the interaction domain is also apparent in power spectra of the streamwise velocity component, acquired using LDV. The power spectral density is plotted against normalized wavenumber $(k = 2\pi f / U_\infty)$ at constant elevation within the boundary layer $(y/\delta = 0.065)$ for several streamwise locations in Figure IV.17-Left, for the baseline and actuated flows. The slight upturn in the power spectra at the upper end of the frequency range is due to aliasing of energy contained above the Nyquist frequency. Immediately downstream from the orifice $(x/\delta = 0.16)$, the spectral peaks at the actuation frequency (1130 Hz, $k\delta = 22.0$) and its higher harmonics are present, and there is substantially more energy at all frequencies compared to the baseline. The inertial subrange is shifted to higher frequencies, starting at the actuation frequency, as energy is transferred to scales above and below the actuation frequency. The rapid reduction in turbulent kinetic energy is evident in the spectra downstream from the interaction domain $(x/\delta = 0.65, 1.3, 1.9, 2.6$ and $3.5)$. The spectral peak at the actuation frequency decays with downstream distance from the actuator orifice, and the normal energy cascade is re-established as the spectra relax toward its baseline shape. It should be noted that at $x/\delta = 1.3, 1.9$ & 2.6, there is a range of frequencies centered on $k\delta \sim 2$, where the actuated spectra falls below the baseline, ostensibly the result of the enhanced dissipation. Further downstream there is little difference between the baseline and actuated spectra, except for a small peak at the actuation frequency. The variation in power spectra of u across the boundary layer is shown at $x/\delta = 0.65, 1.3,$ and 1.9 in Figures IV.17-Right, IV.18-Left, and IV.18-Right, respectively. Similar to the observed changes in the velocity distributions, the effect of synthetic jet actuation on the power spectra is confined to the inner portion of the boundary layer $(y/\delta < 0.2)$.

IV.5 JET PENETRATION SCALING WITH THE ENTIRE BOUNDARY LAYER

The interaction of a synthetic jet with a flat plate boundary layer is also investigated under circumstances that lead to the formation of discrete vortices that scale with the entire width of the boundary layer. This is not a trivial undertaking, since even with maximum suction applied at the leading edge of the flat plate model, the boundary layer thickness within the test section is greater than 10 mm. In order to create the largest possible discrete vortices, the loudspeaker synthetic jet actuator was employed since the volume of fluid expelled per cycle is inversely proportional to formation frequency. Several combinations of actuation frequency, amplitude, and free stream velocity were tried before settling on the conditions: $U_\infty = 8.0$ m/s, $\delta = 12.5$ mm, $\theta = 1.4$ mm, $f = 300$ Hz, $\overline{U}_j = 12.5$ m/s, and $b = 1.91$ mm. The corresponding dimensionless parameters are: $Re_\theta = 700$, $\delta/b = 6.5$, $\overline{U}_j/U_\infty = 1.25$, and $St_\delta = 0.47$. In the context of the flow regime transition map (cf. Figure 22) the local dimensionless frequency for this set of parameters is $\hat{f} = 0.03$ (assuming the mean centerline velocity at $y = 10b$ is $\sim 0.5\ \overline{U}_j$). Eighteen phases of the flow, locked to the actuation in 20° increments, are measured in fifteen overlapping sets of PIV images. Ten sets of 400-800 images per phase are acquired at 15.1 μm/pixel to resolve the flow immediately adjacent to the wall, and five sets of 400 images per phase are acquired at 30.7 μm/pixel resolve the outer region of the boundary layer.
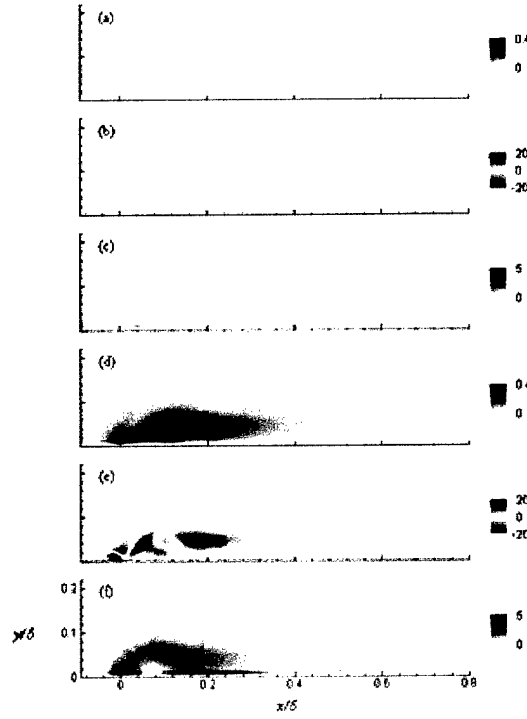
59

Figure IV.15. *Normalized turbulent kinetic energy:* $\hat{q}^2$, $\hat{P}$, $\hat{\mathcal{E}}$ *baseline (a), (b), & (c), and actuated (d),(e), &*
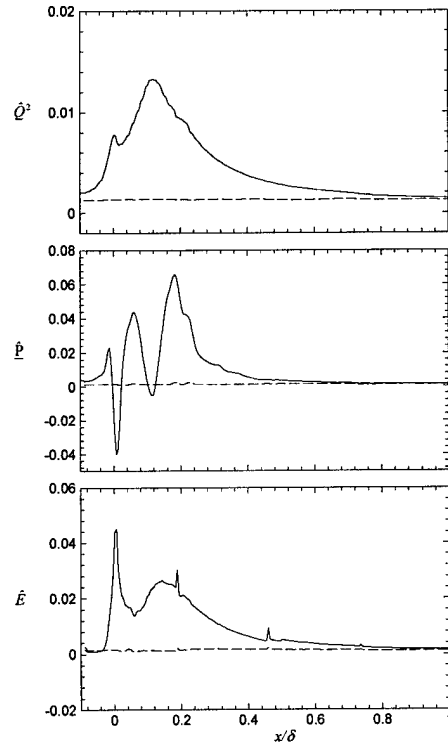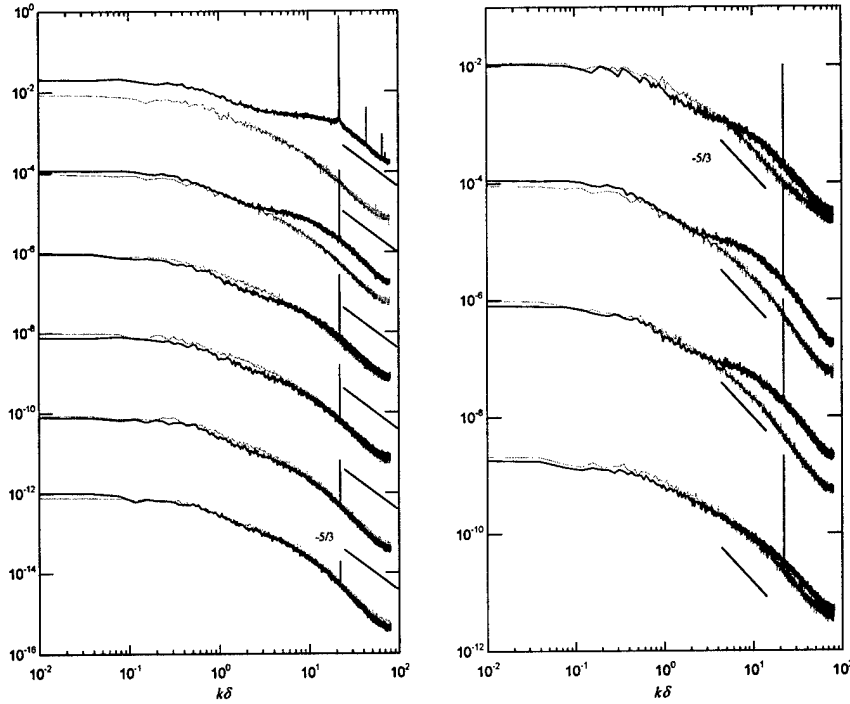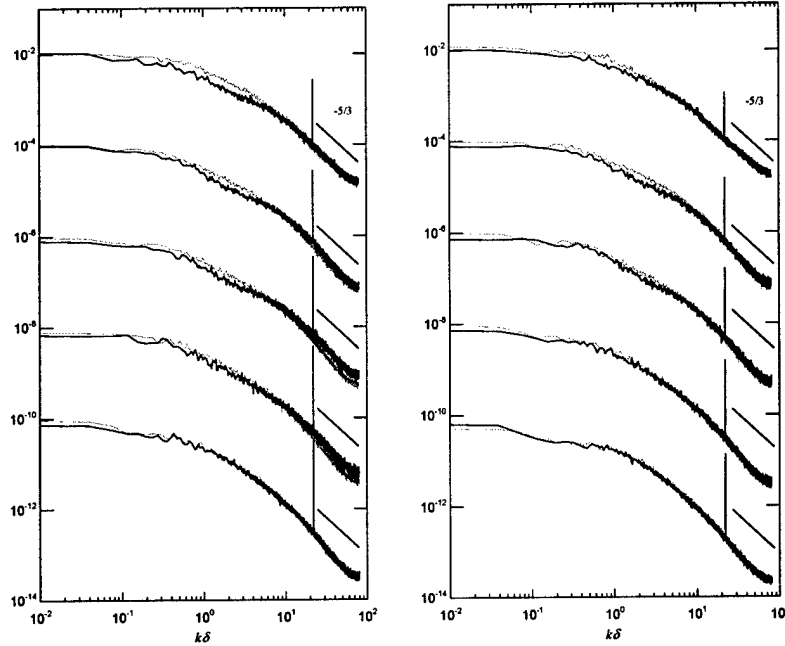

Figure IV.16. *Integrated turbulent kinetic energy budget:* $\hat{Q}^2$ *(a),* $\underline{\hat{P}}$ *(b), and* $\hat{E}$ *(c); The baseline is dashed.*

60

Figure IV.17 *u power spectra (baseline is in gray). Left: y/δ = 0.065 (y+ = 60), x/δ = 0.16, 0.65, 1.3, 1.9, 2.6, and 3.5 (top to bottom). Right: x/δ = 0.65, y/δ = 0.032, 0.065, 0.097, and 0.16 (top to bottom) (y+ = 30, 60, 90, and 145). Successive locations displaced by two decades.*

Figure IV.18. *u power spectra (baseline in gray) Left: x/δ = 1.3, y/δ = 0.032, 0.065, 0.097, 0.16, and 0.26 (top to bottom). (y+ = 30, 60, 90, 145, and 240) Right: x/δ = 1.9, y/δ = 0.032, 0.065, 0.13, 0.26, and 0.52 (top to bottom). (y+ = 30, 60, 120, 240, and 470. Successive locations displaced by two decades.*

61

IV.5.1 The Velocity Field

The phase-averaged spanwise vorticity field is shown for every third phase of actuation in Figure IV.19-Left. At the onset of the blowing portion of the cycle ($\phi = 0°$, Figure IV.19-Left a), the previously formed vortices from the interaction have been advected downstream from the actuator orifice by the free stream. During the blowing cycle a vortex pair forms at the actuator orifice. By $\phi = 60°$ (Figure IV.19-Left b) the formation of the vortex pair is almost complete, and as the blowing cycle continues a stem of fluid is expelled behind the pair (Figure IV.19-Left c). The vortex pairs penetrate to approximately $y/\delta = 0.9$ at $\phi = 240°$, much farther than the previous case (§IV.4, $Re_\theta = 2,100$, $\delta/b = 61$, $\overline{U}_j/U_\infty = 1.25$, & $St_\delta = 3.5$). As the jet fluid is deflected by the cross-flow, the upstream (CCW) half of the vortex pair is subjected to a higher advection velocity and overtakes the CW vortex (Figure IV.19-Left d and e). During the suction phase ($180° \leq \phi \leq 360°$, Figure IV.19-Left d-f), upstream fluid is drawn into the actuator, resulting in a "fuller" boundary layer profile immediately upstream from the actuator orifice. Once the discrete vortices are fully formed, they remain at approximately the same elevation within the boundary layer and rapidly diminish in strength and coherence as they travel downstream. The vortices completely disappear within three wavelengths, and a new inner boundary layer is re-established.

In the time-averaged interaction domain is comprised of a stationary vortex adjacent to the surface and immediately downstream from the actuator orifice as shown in the time-averaged vorticity field in Figure 132. The vortex extends approximately 0.8δ outward from the surface and 2δ downstream. The discrete vortices are of sufficient strength to induce time-averaged reverse flow within the interaction domain, and therefore a time-averaged separation bubble is created as shown in the streamlines plotted in Figure 133. The dividing streamline $\bar{\psi} = 0$ extends approximately 0.5δ above the surface, and reattaches at $x/\delta = 1.9$. The modification of the time-averaged velocity profiles is shown in Figure IV.20 in wall coordinates. (The friction velocity of the baseline flow at the actuator orifice, $U_T = 0.405$ m/s, is used in the normalization). The time-averaged velocity field shares many features with the quasi-steady recirculation region formed at a much higher dimensionless frequency (§IV.3). Within the interaction domain ($x/\delta = 1.0$) the passage of the discrete vortices induces time-averaged reversed flow adjacent to the wall. The presence of the interaction domain displaces the cross-flow fluid, and the associated convective acceleration as well as the additional momentum injected by the synthetic jet results in a maximum in the profile at the outer edge of the time averaged vortex. Downstream from the mean reattachment point, there is a significant wake effect in the velocity profile. The associated velocity deficit reduces as a new inner layer within the boundary layer is formed ($x/\delta = 4.0$, 8.0). In fact, the velocity distribution at $x/\delta = 8.7$ definitively exhibits a multi-tiered character, with the formation of an inner boundary layer ($y^+ < 100$, $y/\delta < 0.3$) followed by a region of constant streamwise velocity ($100 < y^+ < 200$, $0.3 < y/\delta < 0.6$) and then an outer layer. Under these conditions, a greater distance is required ($>10\delta$) for the velocity field to recover a normal turbulent boundary layer profile compared to the previous case (§IV.4).

Within the interaction domain, all three components of Reynolds stress are substantially higher than the baseline values as illustrated in Figure IV.21. Cross-stream distributions of the normal ($\overline{u'u'}$ and $\overline{v'v'}$) and shear ($\overline{u'v'}$) components of Reynolds stress downstream from the interaction
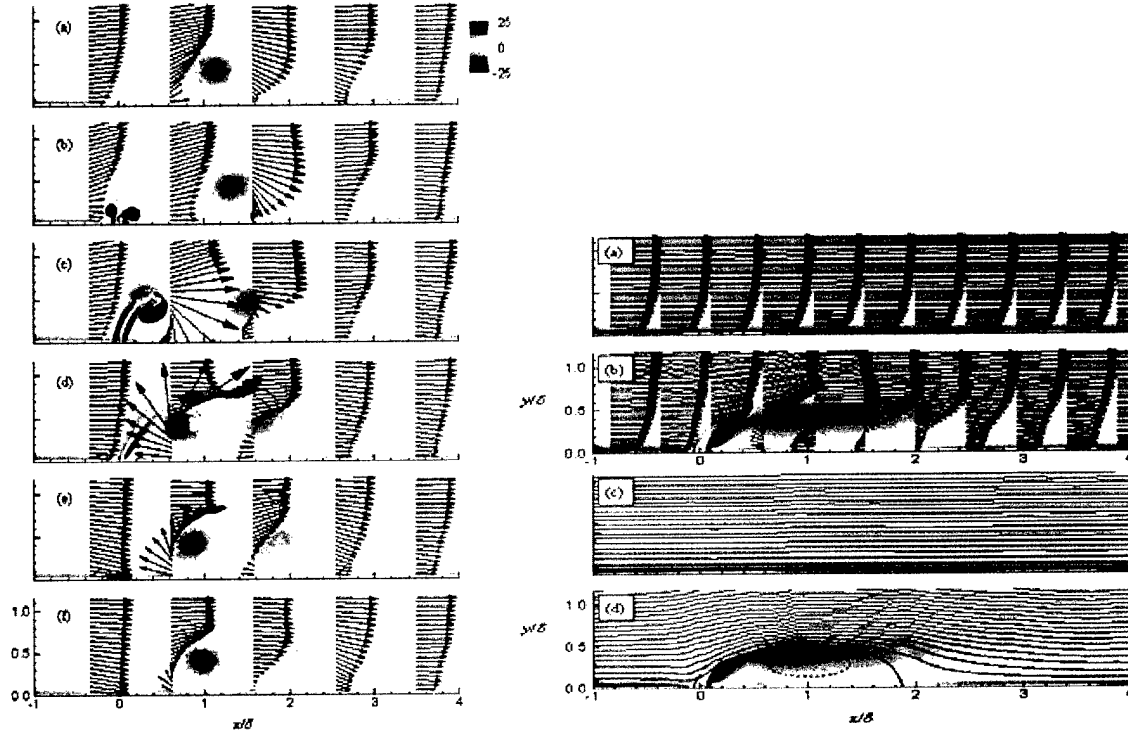
Figure IV.19. Left: Phase-averaged normalized vorticity with superimposed velocity vectors, $Re\theta = 700$, $St\delta = 0.47$, $\overline{U}_j/U_\infty$ = 1.25, $\delta/b = 6.5$: (a) $\phi = 0°$, (b) $60°$, (c) $120°$, (d) $180°$, (e) $240°$, and (f) $300°$. Right: Time-averaged normalized vorticity with velocity vectors (a & b) and streamlines (c & d) for baseline (a, c) and actuatd (b,d).
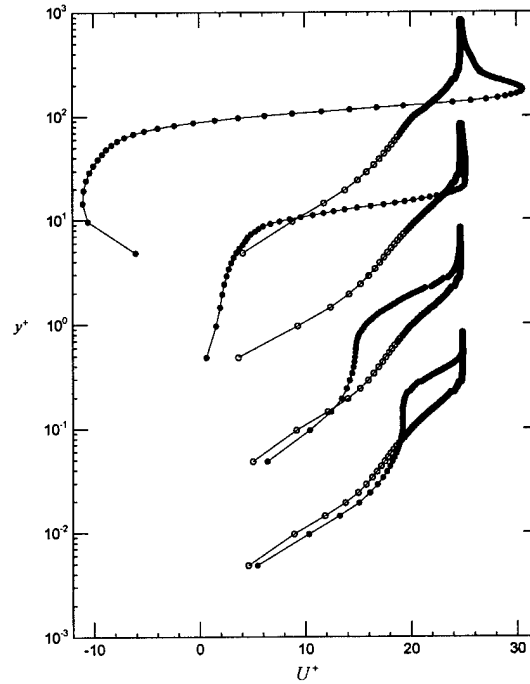

Figure IV.20. Time-averaged velocity profiles in wall units, $x/\delta = 1.0$, 2.0, 4.0, and 8.7 (top to bottom): baseline (O), actuated (●), successive locations separated by one decade.

63

domain are shown in Figures IV.22-Left and IV.22-Right, respectively. At the downstream end of the interaction domain ($x/\delta = 2.0$, Figure IV.22-Left a and IV.22-Right a) all three stress components are still an order of magnitude above the baseline values. The stresses are rapidly attenuated with downstream distance in this region of the flow, decreasing by a factor of three by $x/\delta = 4.0$ (Figure IV.22-Left b and IV.22-Right b). As a new inner region develops within the boundary layer the distributions of Reynolds stresses also change, as local peaks develop close to the wall in $\overline{u'u'}$ and $\overline{u'v'}$ at $x/\delta = 8.7$ (Figures IV.22-Left c and IV.22-Right c). The present data set is not of sufficient extent to determine the streamwise length required for the return to a normal turbulent boundary layer.

IV.5.2 The Pressure Field

The discrete vortices formed by the interaction between a synthetic jet and cross flow induce large pressure gradients locally. The normalized phase-averaged streamwise $< \partial \hat{p}/\partial \hat{x} >$ and cross-stream $< \partial \hat{p}/\partial \hat{y} >$ pressure gradients are shown for six instances during the actuation cycle for the current experimental conditions in Figure IV.23. As observed in earlier measurements, each CW vortex produces alternating sign gradients (favorable, then adverse), which diminish rapidly and completely disappear within two wavelengths. As a result, there is a finite domain immediately downstream from the actuator orifice where the time-averaged pressure gradients are modified as shown in Figure IV.24 (computed via the Reynolds-Averaged Navier Stokes equations). The time-averaged pressure gradients bear a remarkable resemblance with the phase-averaged gradients associated with a single vortex, suggesting that the time-averaged interaction may be modeled as a stationary vortex. The normalized time-averaged pressure field, shown in Figure IV.24, is determined by integrating the pressure gradients using the combined-path Runge-Kutta routine outlined in Appendix B. A low-pressure region is produced immediately downstream from the actuator orifice, with a minimum pressure of $\hat{p} = -2.1$.

IV.5.3 Boundary Layer Evolution

As discussed in §IV.5.1, under the present conditions the combined action of the passage of the discrete vortices results in the formation of a time-averaged stationary vortex, which is sufficiently strong to produce a large time-averaged recirculation region. One indication of the re-establishment of a new inner region of the boundary layer is seen in the wall shear stress, computed from least-square error polynomial curve fits to cross-stream profiles of the streamwise velocity component. The normalized wall shear stress is shown at six phases of actuation in Figure IV.25 along with the time-averaged actuated and baseline values. In the baseline flow, the wall shear at the actuator location is $\hat{\tau}_w = 0.0033$. At the onset of blowing ($\phi = 0°$), there is a local minimum in $\hat{\tau}_w$ at $x/\delta = 1.1$ associated with the previously formed CW vortex. During the blowing portion of the cycle ($\phi = 60°$, $120°$) the wall shear stress upstream from the actuator orifice becomes smaller, and large negative shear is produced as the vortex pair rolls-up (at $\phi = 60°$, $\hat{\tau}_w = -0.012$ at $x/\delta = 0.16$, compared with the baseline value of 0.0033). As expected, the deviation in shear stress from the time-averaged value associated with each vortex rapidly diminishes downstream. During the suction portion of the cycle ($\phi = 240°$, $300°$) the shear stress is upstream of the orifice increased, and decreased immediately downstream as fluid is drawn into the actuator. The net effect is a region of reduced wall shear stress immediately downstream from the orifice, in fact, negative shear persists for $0 \leq x/\delta \leq 1.9$ as a mean
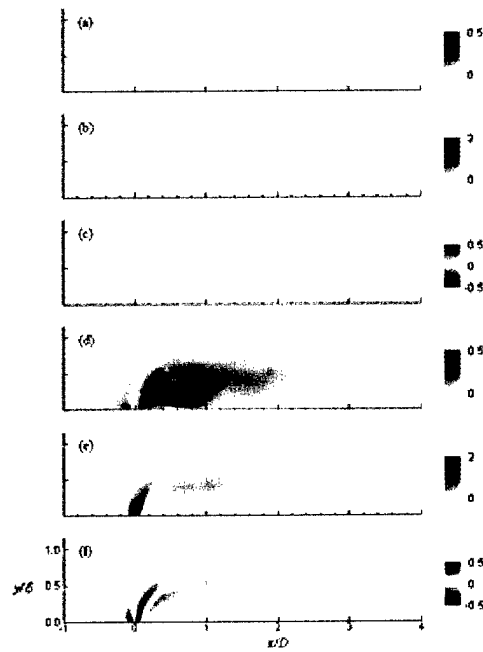
Figure IV.21. *Reynolds Stress, baseline:* $\overline{u'u'}/U_\infty^2$, $\overline{v'v'}/U_\infty^2$ & $\overline{u'v'}/U_\infty^2$ *baseline (a, b & c) and actuated (d, e, & f).*
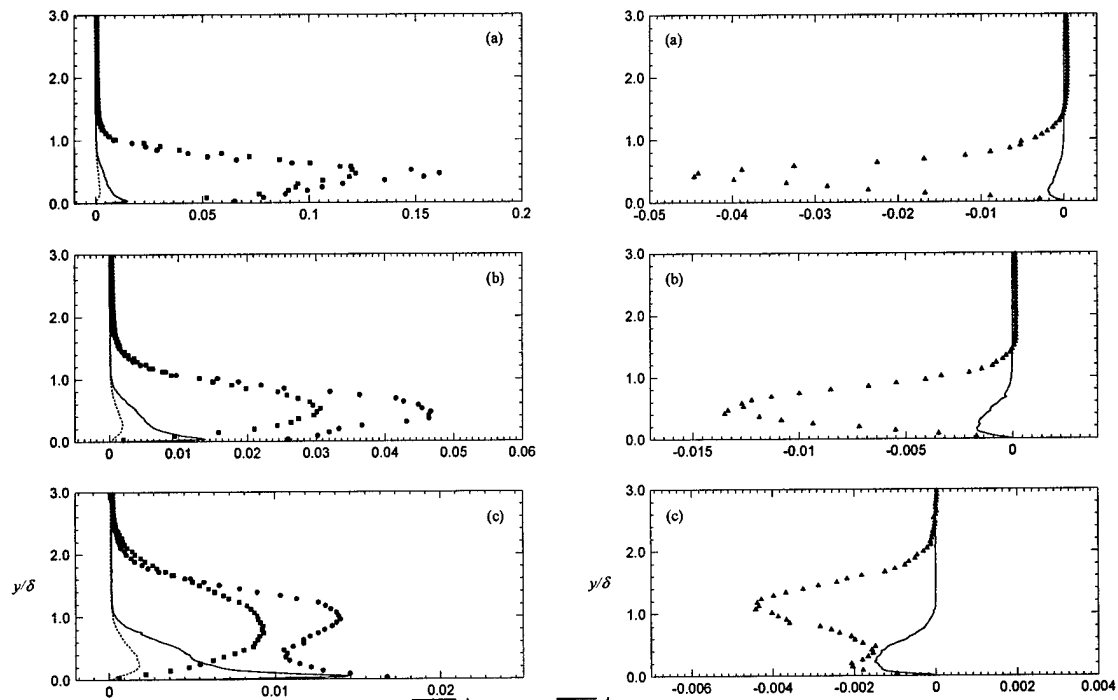

Figure IV.22. *Cross-stream distribution of Left:* $\overline{u'u'}/U_\infty^2$ & $\overline{v'v'}/U_\infty^2$: *(a)* $x/\delta = 2.0$, *(b)* 4.0, and *(c)* 8.67: *(baseline in solid and dashed lines, and actuated ● & ■), Right:* $\overline{u'v'}/U_\infty^2$, $x/\delta = 2.0$ *(a),* 4.0 *(b), and* 8.67 *(c).* *baseline in solid line and actuated in ▲).*

65
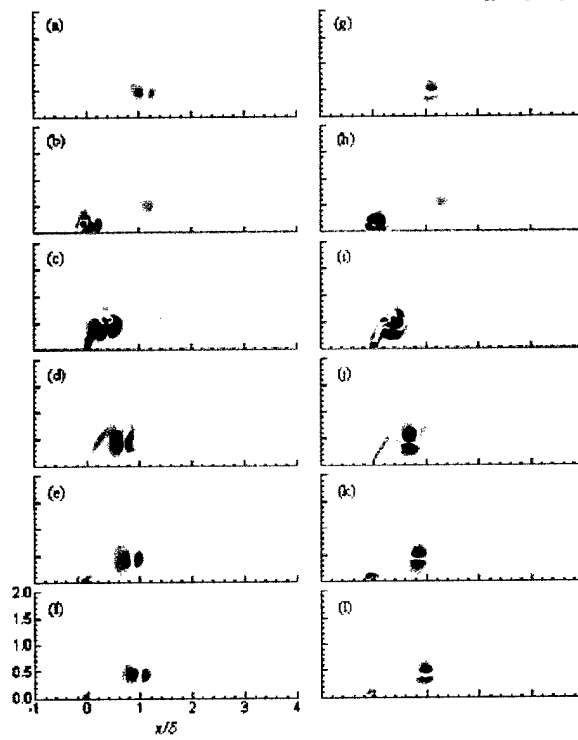
Figure IV.23. *Phase-averaged normalized pressure gradients, C (a-f); $<\partial \hat{p}/\partial \hat{y}>$ (g-l): (a, g) $\phi = 0°$, (b, h) 60°, (c, i) 120°, (d, j) 180°, (e, k) 240°, and (f, l) 300°.*
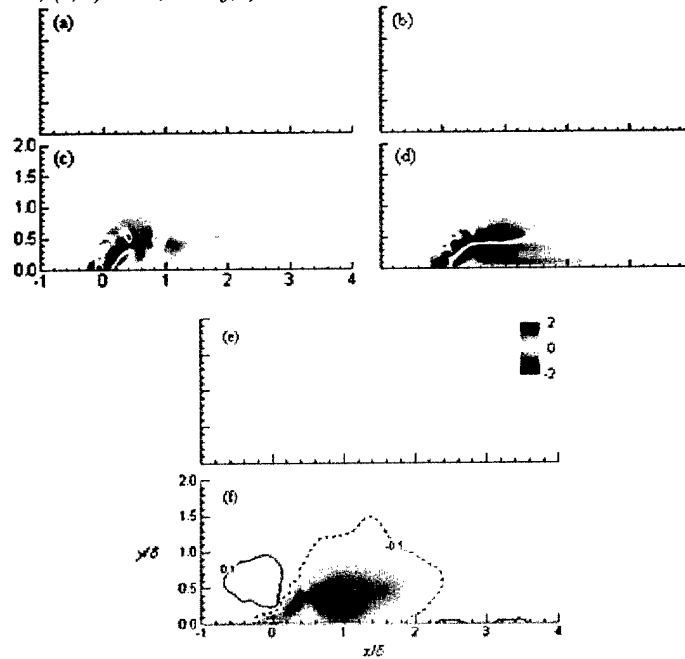

Figure IV.24. *Normalized Reynolds-averaged pressure gradients, $\partial \hat{p}/\partial \hat{x}$ $\partial \hat{p}/\partial \hat{y}$ baseline (a, b) and actuated:(c, d). Normalized time-average pressure, baseline (d) and actuated (e) (Dashed and solid lines indicate least significant contours.)*

66

recirculation region is created (cf. Figure 133). Downstream from this region, the shear stress in the presence of actuation rapidly recovers its baseline value as a new inner region in the boundary layer is formed.

Both the displacement thickness (δ^*) and momentum thickness (θ) are substantially modified across the entire measurement domain by the interaction, as shown in Figure IV.26. The discrete vortices displace the cross flow fluid within the interaction domain, causing a local maximum in δ^* at $x/\delta = 1$. Within the same region, the additional momentum input of the jet, as well as the convective acceleration of the cross-flow due to the displacement effect results in negative momentum thickness (indicating that the flow contains more momentum than a uniform profile at U_∞). The shape factor h_{12}, which is has little physical meaning within the interaction domain, is reduced downstream from the interaction domain compared to the baseline ($h_{12} = 1.40$ vs. 1.55), indicating that the boundary layer has more momentum immediately adjacent to the wall as a new inner layer is formed (cf. Figure IV.20). It is apparent that compared to the case with discrete vortices scaling with the inner portion of the boundary layer (§IV.4) the boundary layer characteristics downstream from the interaction domain require a much greater streamwise distance to fully evolve.

IV.5.4 Turbulent Kinetic Energy

The normalized time averaged turbulent kinetic energy ($\hat{q}^2$) is plotted alongside the normalized rates of turbulence production ($\hat{P}$) and viscous dissipation ($\hat{\varepsilon}$) in Figure IV.27 for the baseline and actuated flows. In the baseline flow, turbulent kinetic energy is distributed throughout the boundary layer (profiles of $\overline{u'u'}$ and $\overline{v'v'}$ are shown in Figure IV.2) while the highest levels of production and viscous dissipation are adjacent to the wall. In the actuated flow, the largest magnitudes of $\hat{q}^2$, $\hat{P}$, and $\hat{\varepsilon}$ are confined to the interaction domain and are an order of magnitude larger than those present in the baseline flow. Particularly large values for all three quantities occur immediately above the actuator orifice, where the velocity fluctuations introduced by the synthetic jet are largest. Negative turbulence production, occurring above the actuator orifice, indicates a transfer of energy from the periodic jet motion, into the mean flow. The largest [positive] turbulence production occurs in the domain where the discrete vortices break down ($0.2 < x/\delta < 2$). Downstream from the interaction domain, the largest rates of production and dissipation occur adjacent to the surface within the newly formed inner layer ($y/\delta < 0.2$, cf. Figure IV.20).

Power spectra of the u velocity component are obtained from LDV data. The streamwise variation of power spectra at constant elevation within the boundary layer ($y/\delta = 0.32$) is shown in Figure IV.28a, for the baseline and actuated flows. Within the interaction domain ($x/\delta = 0.8$, 1.5) the entire spectra is shifted since there is substantially more turbulent kinetic energy in the flow. In addition to the spectral peak at the actuation frequency ($k\delta = 2.9, f = 300$ Hz), higher harmonics are also present within this region. At $x/\delta = 1.5$ the interaction leads to an expanded inertial subrange, with a -5/3 slope starting at the actuation frequency and extending at least a decade. In the region downstream from the interaction domain, where a normal turbulent boundary layer begins to redevelop, the spectra contain multiple changes in slope as it redevelops a normal energy distribution. While the spectral peak at the actuation frequency decreases with downstream distance from the actuator, it is still present at $x/\delta = 18$.
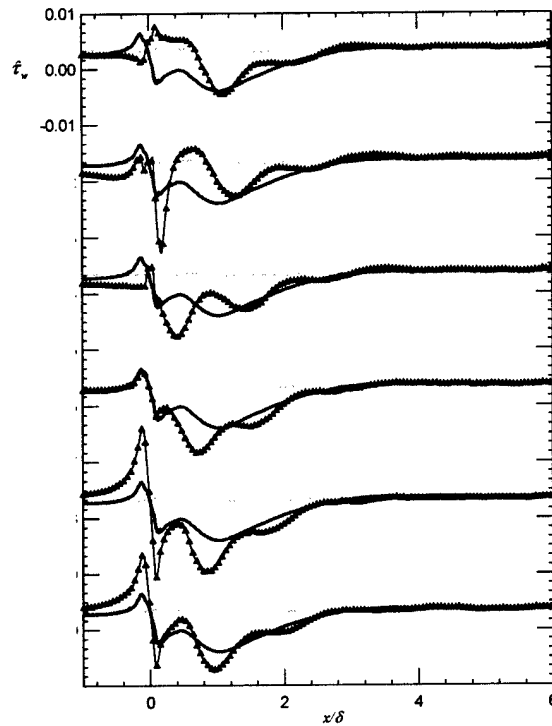
Figure IV.25. Normalized wall shear stress, $\phi = 0°$, $60°$, $120°$, $180°$, $240°$, and $300°$ (from top to bottom, successive phases separated by 0.02): (baseline-gray line; time-averaged actuated-black solid line, phase-averaged $\triangle$).
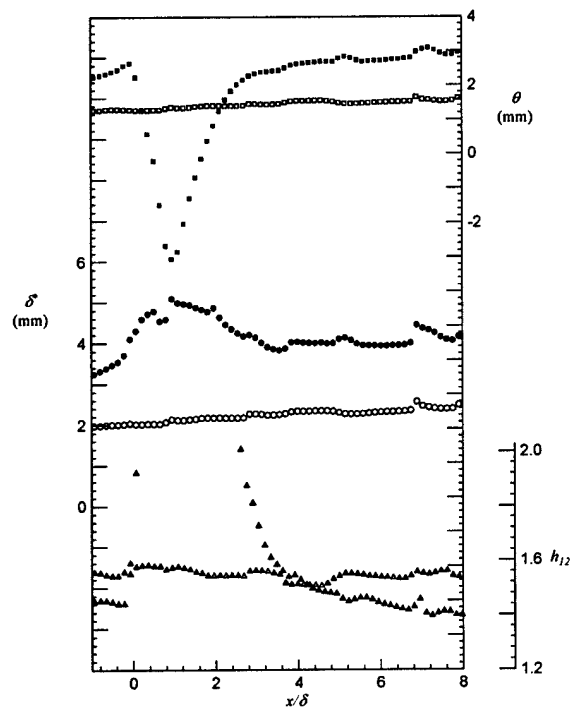

Figure IV.26. Boundary layer evolution, baseline: δ^* (O), θ ($\square$), $h12$ ($\triangle$); actuated: δ^* (●), θ (■), $h12$ (▲).
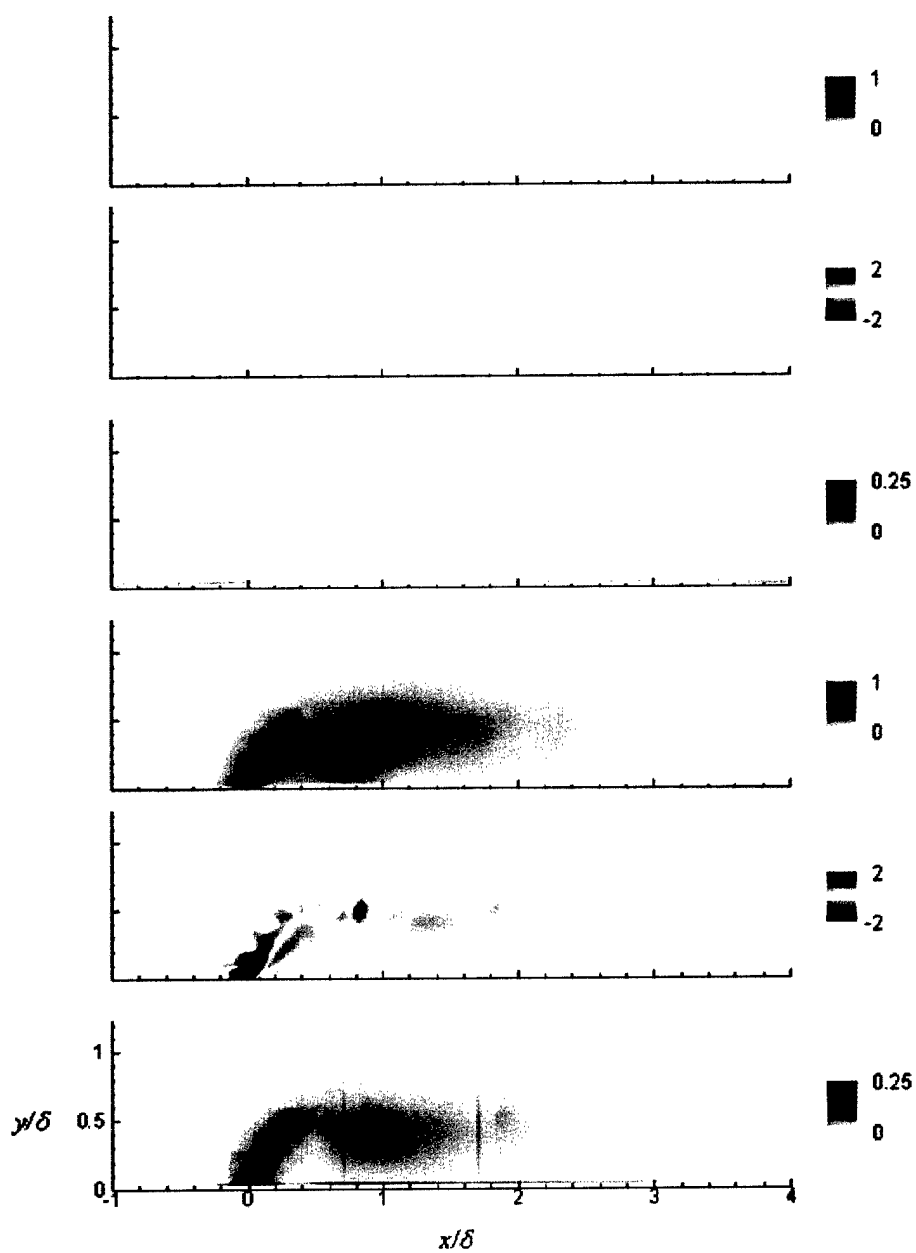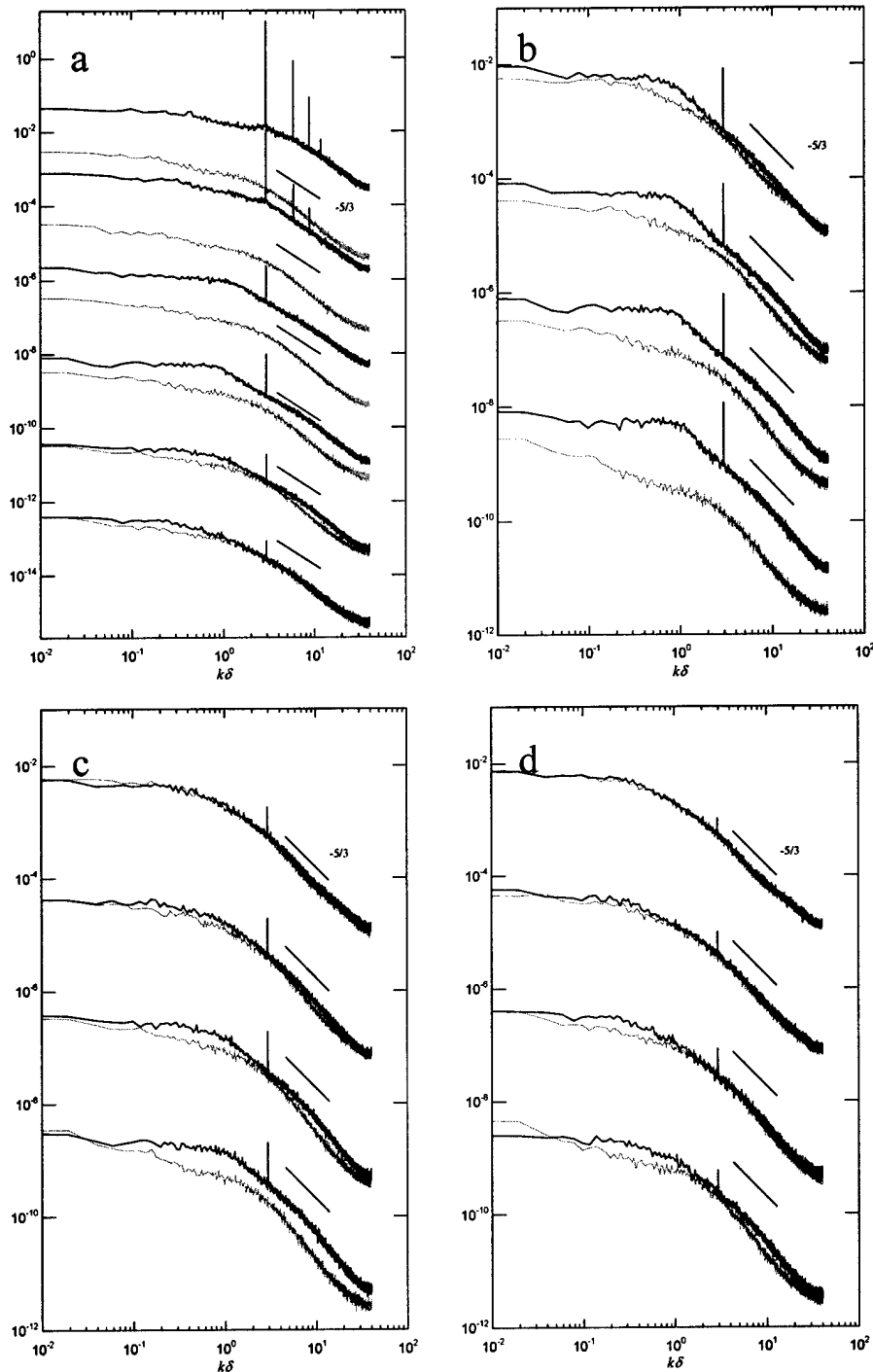
68

Figure IV.27. *Normalized turbulent kinetic energy:* $\hat{q}^2$, $\hat{P}$, *&* $\hat{\varepsilon}$: *baseline (a, b, & c) and actuated (d, e, &*
f).

Figure IV.28. *u power spectra: a) y/δ = 0.32 (y+ = 85), x/δ = 0.8, 1.5, 3.0, 6.1, 12, and 18 (top to bottom), b) x/δ = 6.1, y/δ = 0.08, 0.16, 0.32, and 0.64 (top to bottom) (y+ = 21, 43, 85, and 170), c) x/δ = 12, y/δ = 0.08, 0.16, 0.32, and 0.64 (top to bottom) (y+ = 21, 43, 85, and 170), and d) x/δ = 18, y/δ = 0.08, 0.16, 0.32, and 0.64 (top to bottom) (y+ = 21, 43, 85, and 170. Baseline in gray, actuated solid line. Successive spectra displaced by two decades.*

70

The variation in u power spectra across the boundary layer is shown at x/δ = 6.1, 12, and 18 in Figures IV.28b, IV.28c, and IV.28d, respectively. At x/δ = 6.1, the actuated flow still contains more turbulent kinetic energy than the baseline, particularly so at higher cross-stream elevations above the surface. Curiously, in contrast to the baseline flow the power spectral density of the actuated flow is roughly constant for $k\delta$ < 1, and has approximately a $-\frac{5}{3}$ slope at higher frequencies. Further downstream (x/δ = 12, 18), except for a small peak at the actuation frequency, the baseline actuated spectra are almost indistinguishable for $y/\delta \leq 0.16$ ($y^{+} \leq 43$), which is within the inner tier of the redeveloping boundary layer. The outer part of the boundary layer requires greater streamwise distance to recover a normal turbulence structure due to the wake effect caused by the presence of the interaction domain.

IV.6 CONCLUSION: DEMONSTRATION OF SEPARATION CONTROL

As demonstrated in earlier work at Georgia Tech, synthetic jet actuation can significantly alter the aerodynamic characteristics of a circular cylinder. In particular, the modification of the streamwise pressure gradient within the interaction domain leads to a thinner boundary layer downstream, which is more capable of withstanding adverse pressure gradients. The resultant delay in boundary layer separation leads to the generation of lift, and the reduction in pressure drag. In this section, the effects of synthetic jet actuation on a separated flow are studied within the flat plate boundary layer.

A separated flow region on the flat plate was created by mounting a 75 mm tall obstruction with a downstream fairing to the flat plate model. The free stream velocity and actuation conditions are identical to those in §IV.4 (U_∞ = 10 m/s, f = 1130 Hz, $\overline{U}_j$ = 12.5 m/s, and b = 0.051 mm). The streamwise location (125 mm downstream from the orifice) was selected such that boundary layer separation occurs downstream of the interaction domain. In the absence of actuation, the wall-mounted obstruction induces the formation of a large separated flow region and a trapped vortex, as seen in Figures IV.29a (time-averaged velocity distributions) and 149a (corresponding streamlines). Jet actuation leads to the formation of a time-averaged separation bubble that is characterized by the dividing streamline ψ = 0 (Figure 149b). The presence of the interaction domain displaces and accelerates the cross flow fluid (Figure IV.29b). Remarkably, even in the presence of such a large adverse pressure gradient (imposed by the obstruction) a new inner layer is formed within the boundary layer, as seen in the velocity distribution at x/b = 140. The creation of this inner layer, ostensibly the result of a modification of the streamwise pressure gradient within the interaction domain, results in a downstream movement of the separation streamline from x/b = 110 to x/b = 140.
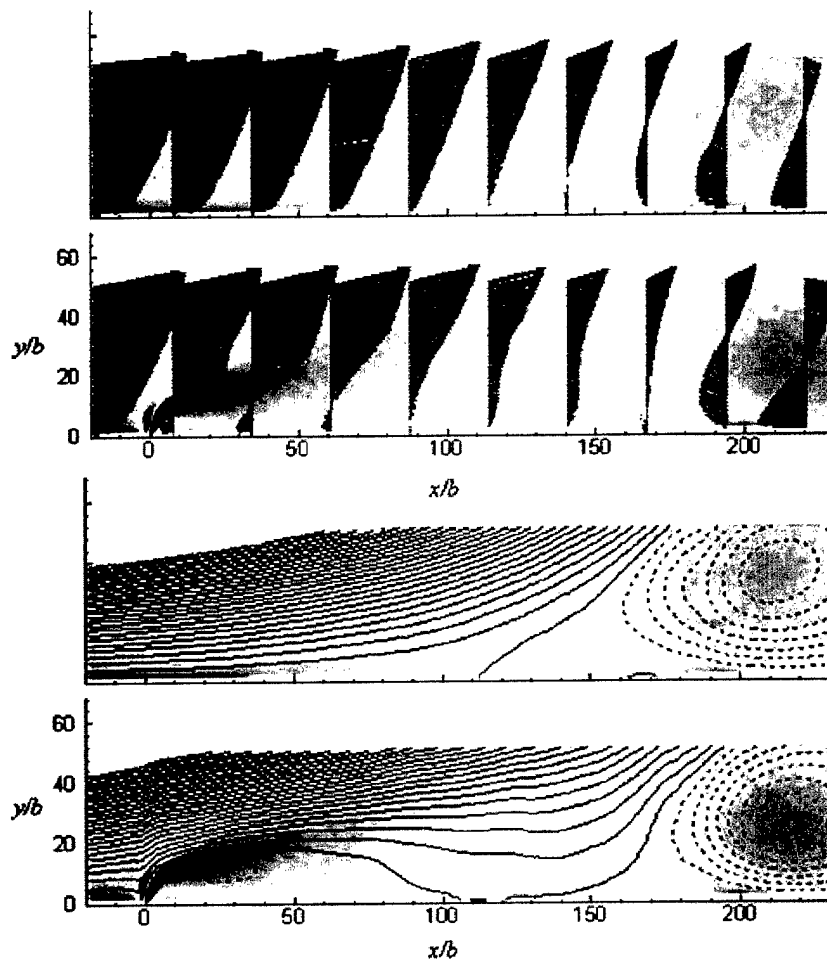
Figure IV.29. Separation control using synthetic jet actuation, time-averaged normalized vorticity for unforced and forced with superimposed velocity distributions (top) and strea,lines (bottom). Streamlines shown in increments of 0.8 U∞ with negative values shown as dashed lines. =

72